AD-A058 698 LOCKHEED MISSILES AND SPACE CO INC PALO ALTO CALIF PA--ETC F/G 6/18
RADIATION EFFECTS OF IR DETECTORS.(U)
MAR 78 F A JUNGA, W W ANDERSON, R B EMMONS F19628-75-C-0127

UNCLASSIFIED LMSC/D566051 RADC-TR-78-66 NL

1 OF 2
AD
A058 698

AD A058698

LEVEL II

13

DDC FILE COPY

RADC-TR-78-66
Final Technical Report
March 1978

RADIATION EFFECTS ON IR DETECTORS

Lockheed Palo Alto Research Laboratory

Approved for public release; distribution unlimited.

This research was sponsored by the Defense Nuclear Agency under Subtask TA026, Work Unit 03, entitled: "Radiation Effects on New Devices."

ROME AIR DEVELOPMENT CENTER
AIR FORCE SYSTEMS COMMAND
GRIFFISS AIR FORCE BASE, NEW YORK 13441

78 09 14 031

This report has been reviewed by the RADC Information Office (OI) and is releasable to the National Technical Information Service (NTIS). At NTIS it will be releasable to the general public, including foreign nations.

RADC-TR-78-66 has been reviewed and is approved for publication.

APPROVED: Jerry Silverman

JERRY SILVERMAN
Contract Monitor

If your address has changed or if you wish to be removed from the RADC mailing list, or if the addressee is no longer employed by your organization, please notify ESD (ESE), Hanscom AFB MA 01731. This will assist us in maintaining a current mailing list.

Do not return this copy. Retain or destroy.

SECURITY CLASSIFICATION OF THIS PAGE (When Data Entered)

(19) REPORT DOCUMENTATION PAGE	READ INSTRUCTIONS BEFORE COMPLETING FORM
(18) 1. REPORT NUMBER: RADC-TR-78-66	2. GOVT ACCESSION NO. / 3. RECIPIENT'S CATALOG NUMBER
(6) 4. TITLE (and Subtitle): RADIATION EFFECTS ON IR DETECTORS,	(9) 5. TYPE OF REPORT & PERIOD COVERED: Final Report, 30 Jun 75-30 Jan 78,
	(14) 6. PERFORMING ORG. REPORT NUMBER: LMSC D566051
(10) 7. AUTHOR(s): Frank A. Junga, W. W. Anderson, R. B. Emmons	(15) 8. CONTRACT OR GRANT NUMBER(s): F19628-75-C-0127
9. PERFORMING ORGANIZATION NAME AND ADDRESS: Lockheed Palo Alto Research Laboratory, 3251 Hanover Street, Palo Alto, California 94304	(16) 10. PROGRAM ELEMENT, PROJECT, TASK AREA & WORK UNIT NUMBERS: PE62702F, 2306J224, CDNA (17) J2
11. CONTROLLING OFFICE NAME AND ADDRESS: Defense Nuclear Agency, Washington, D.C. 20305 (12) 120 p.	(11) 12. REPORT DATE: March 1978 / 13. NUMBER OF PAGES: 120
14. MONITORING AGENCY NAME & ADDRESS (if different from Controlling Office): Deputy for Electronic Technology (RADC), Hanscom AFB, Massachusetts 01731, Monitor/J. Silverman/ESE	15. SECURITY CLASS. (of this report): Unclassified / 15a. DECLASSIFICATION/DOWNGRADING SCHEDULE

16. DISTRIBUTION STATEMENT (of this Report)

Approved for public release; distribution unlimited.

17. DISTRIBUTION STATEMENT (of the abstract entered in Block 20, if different from Report)

18. SUPPLEMENTARY NOTES

This research was sponsored by the Defense Nuclear Agency under Subtask TA 026; Work Unit 03, entitled: "Radiation Effects on New Devices."

19. KEY WORDS (Continue on reverse side if necessary and identify by block number)

INFRARED DETECTORS, MERCURY-CADMIUM TELLURIDE, IONIZING RADIATION EFFECTS, SURFACE STATE STUDIES

20. ABSTRACT (Continue on reverse side if necessary and identify by block number)

The effects of surface potential and surface states on the properties of, and radiation sensitivity of trapping mode mercury cadmium telluride detectors with energy gaps of 0.3 eV and 0.1 eV were investigated. These studies were made with photo MIS structures. Low frequency C-V measurements were made and a program developed to extract the surface state density and surface potential from these data. The responsivity of these devices was dependent on surface potential. Gamma irradiation increased the number of surface states at the

(over)

DD FORM 1 JAN 73 1473 EDITION OF 1 NOV 65 IS OBSOLETE

SECURITY CLASSIFICATION OF THIS PAGE (When Data Entered)

210118

mt

valence band edge but did not affect surface potential. The 0.3 eV detectors appeared to be more radiation sensitive than the 0.1 eV detectors.

The results of this study are briefly discussed in light of current models for trapping behavior.

TABLE OF CONTENTS

	Page
INTRODUCTION	1
EXPERIMENTAL PROCEDURE	9
EXPERIMENTAL RESULTS	18
RADIATION EFFECTS ON DETECTOR PROPERTIES	75
DISCUSSION	84
APPENDIX	88

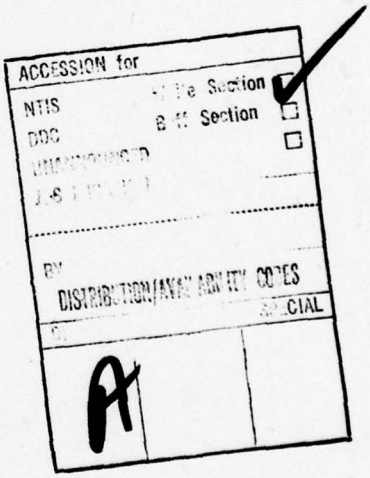

Final Report

RADIATION EFFECTS ON IR DETECTORS

INTRODUCTION

The minority carrier "trapping" which appears in some HgCdTe detectors at low backgrounds and low temperatures is of great practical importance. The trapping mechanism, although not completely understood, is known to interact in a significant way with the device surface potential. Low energy ionizing radiation also affects device surface potentials, and thus may have important effects on trapping mode detectors. The purpose of this work is to further investigate the minority carrier trapping mechanism in HgCdTe photoconductors, and in particular to determine the effects of ionizing radiation on these devices.

$Hg_{1-x}Cd_xTe$ is a ternary semiconductor (for $x > 0.14$). Its bandgap may be adjusted by changing the relative proportions of Hg and Cd. The detectors studied here are of two compositions, one providing a cutoff wavelength at about 4.5 μm, the other at about 12.0 μm. The material used in both cases is extrinsic, n-type, and has a nominal electron concentration of 10^{15} cm^{-3}. As photoconductors, the devices are "intrinsic" in the sense that the optical excitation is band-to-band.

At high temperatures or with large optical background fluxes incident, the photoconductivity observed in HgCdTe is similar to that expected from Ge or Si. Both carriers are mobile, and minority carrier sweepout is observed [References 1 through 3]. The excess majority and minority carrier lifetimes are about

[1] R. L. Williams, B. H. Breazeale, and C. G. Roberts, "Sweepout of Minority Carriers in $Hg_{1-x}Cd_xTe$," Proc. of the Third Int. Conf. on Photoconductivity, E. M. Pell, ed. (Oxford, Pergamon Press, Inc., 1971) 237-242

[2] S. P. Emmons and K. L. Ashley, "Minority Carrier Sweepout in 0.09 eV HgCdTe," App. Phys. Letters, Vol. 20, 162-164 (1972)

[3] M. R. Johnson, "Sweepout Effects in $Hg_{1-x}Cd_xTe$, Photoconductors," J. App. Phys., 43, 3090-3093 (July 1972)

78 09 14 031

10^{-6} sec, and a band-to-band or Shockley-Read recombination process is indicated. The factors which control background-limited detectivity in photoconductors of this type are well known [References 4 and 5] and have been specifically applied to HgCdTe [Reference 6]. However, HgCdTe, when functioning with two mobile carriers, is not a candidate for sensitive low-background applications. The argument leading to this conclusion can be summarized briefly as follows:

To obtain background-limited detectivity, the background-induced generation-recombination noise must exceed the detector Johnson-Nyquist noise. Both depend on the majority carrier concentration, but the one inversely and the other inversely as the square root. Thus, to improve the ratio, the majority carrier concentration must be decreased. Since the g-r noise is also proportional to the photoconductive gain, the ratio might also be increased by increasing the photoconductive gain. But the gain is limited by minority carrier sweepout, and saturates when the sweepout time becomes less than the majority carrier time constant. Nothing can be done about that as long as both carriers are mobile. Thus, with two mobile carriers, the detectivity can be improved only by reducing the majority carrier concentration. A comparison of the magnitudes of the generation-recombination noise and the Johnson-Nyquist noise shows very quickly, however, that to obtain background-limited operation with backgrounds below $\sim 10^{15}$ photons cm^{-2} sec^{-1} and two mobile carriers, the majority carrier density in HgCdTe would have to be reduced correspondingly. But a reduction of more than a factor of 10 in majority carrier density is unlikely.

However, at low detector temperatures and with low incident backgrounds, the

[4] E. R. Rittner, "Electron Processes in Photoconductors," Photoconductivity Conference, R. G. Breckenridge, ed., (John Wiley & Sons, Inc., New York, 1954) 215-268
[5] M. Nisenoff and H. Y. Fan, "Photoconductivity in Uniform Germanium" Purdue University Department of Physics (unpublished) (June 30, 1952)
[6] R. L. Williams, "Sensitivity Limits of 0.1 eV Intrinsic Photoconductors," Infrared Physics, Vol. 8, 337 (1969)

mode of operation of HgCdTe photoconductors shifts [References 7 through 13]. At these low backgrounds, minority carriers are immobilized.* Minority carrier sweepout no longer occurs and thus no longer limits the attainable photoconductive gain. The photoconductive gain is now controlled by the excess majority carrier lifetime, which may increase from about 10^{-6} sec to times as long as a few seconds. These changes produce dramatic increases in responsivity, g-r noise, and thus detectivity, which in turn permit background-limited operation with incident background intensities in the range of 10^{10} to 10^{15} ph/cm^2 sec.

Minority carrier trapping permits these large increases in detectivity by producing an increase in the detector time constant in lieu of the decrease in majority carrier concentration which would be required to produce an equal detectivity if both carriers were mobile. This "exchange" is essential to the successful practical application of HgCdTe detectors with realistically obtainable majority carrier densities in the presence of low background radiation intensities. The behaviour of the critically important photoconductive time constant is the most obvious measure of trapping mode behavior.

---

[7] C. G. Roberts, et al., "Cold Background Performance of 0.1 eV Bandgap HgCdTe Detectors," Minutes of ABMDA Detector Meeting, 28-47 (Apr 1970)

[8] T. Koehler and J. Schlickman, "Characteristics of HgCdTe Intrinsic Photoconductors Under Low Background Conditions," Minutes of ABMDA Detector Meeting, 86-105 (Apr 1970)

[9] S. R. Hawkins, et al., "Results of Recent Measurements on Extrinsic Ge and HgCdTe Detectors Under Low Background Conditions," Minutes of ABMDA Detector Meeting, 137-176 (Apr 1970)

[10] R. B. Horst, et al., "Characterization of Trapping Mechanisms in Mid and Far IR $Hg_{1-x}Cd_xTe$ Detectors," Proc. of the Detector Specialty Group Meet., IRIS, 217-248 (1971)

[11] A. F. Milton, "The Influence of Spatial Variations in the Minority Carrier Density on the Photoconductive Gain Enhancement Caused by Minority Carrier Trapping," Proc. of the Detector Specialty Group Meet., IRIS, 249-274 (1971)

[12] M. B. Reine, et al., "Intrinsic (Hg,Cd)Te Photodetectors," Proc. of the Detector Specialty Group Meet., IRIS, 399 (1971)

[13] M. R. Johnson, et al, "Short Wavelength HgCdTe Detectors," Proc. of the Detector Specialty Group Meet., IRIS (1972)

---

*Strictly speaking, the mechanism involves a long-lived recombination center and not a trap. Having noted the distinction, the center will be referred to as a trap, which is the more common generic term.

Time Constant Dependence on Intensity

In trapping mode operation, the HgCdTe photoconductive detector time constant (i.e., the excess majority carrier lifetime) not only becomes large, but also becomes dependent on the incident radiation intensity. Small signal responsivity measurements taken as a function of frequency with incident background as a parameter produce curves such as those shown in Figure 1.

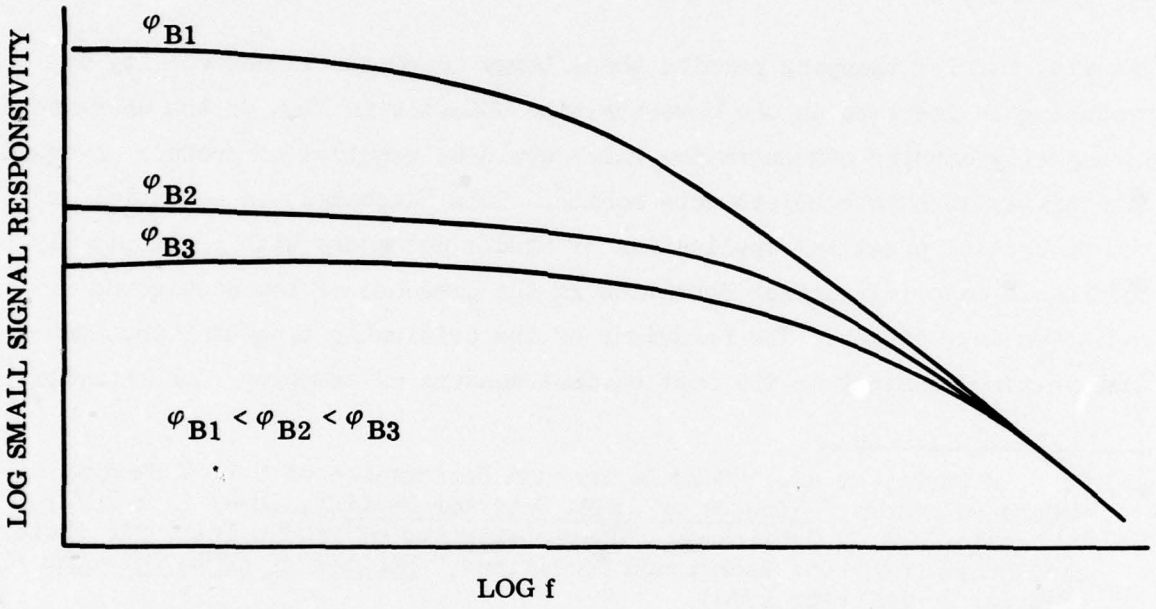

Figure 1. Form of small signal responsivity variation with frequency for different background intensities for HgCdTe detectors under low temperature, low background intensity conditions

In the high frequency rolloff region the responsivity is (almost completely) independent of the background intensity. However, as the background decreases, the 3 db rolloff frequency decreases, and the low frequency responsivity increases. These changes are selfconsistent, and predict a small signal lifetime dependence on background given by

$$\tau_n = \frac{k}{\phi_B^{\alpha}} \qquad (1)$$

where τ_n is the excess majority carrier (electron) lifetime, ϕ_B is the incident photon flux density, and k and α are constants.

The value of α in Eq. (1) is constant for a given detector, but varies somewhat from detector to detector. Values of approximately 0.5 are observed for 12 μm cutoff detectors, and 0.7 for 4.5 μm cutoff detectors. This power law background dependence has been observed in all detectors which show good low background performance, and for individual detectors the functional dependence has been shown to persist over a range of background fluxes extending more than four orders of magnitude [Reference 14].

In some cases the frequency response data rolls off more softly than would be expected if a single time constant were dominating the recombination process. The resulting ambiguity in the 3 db time-constant is not so severe as to prevent determination of background dependence, but does indicate that an adequate model of the trapping behaviour should include the possible operation of multiple time constants.

Mechanisms for an Intensity Dependent Time Constant

The central problem in modeling the trapping mechanism in HgCdTe photoconductors is the development of a physical description of the trapping process which predicts a dependence of the time constant on background raised to a power between $-\frac{1}{2}$ and -1, and which is consistent with the other experimental data. A brief description of the suggestions which have been made will help place the present work in context.

A variation of time constant with intensity given by $\tau = k/\phi^{\frac{1}{2}}$ can be expected if the recombination is bimolecular and if the majority carrier density is determined by the incident radiation. The present case is not of this type since the HgCdTe majority carrier density is too large to be influenced by the radiation intensities used (an observation born out by the constancy of

---

[14] Detector Test Program Final Report, Vol. I, Contract F04701-70-C-0227 (Space and Missile Systems Organization) Lockheed Missiles & Space Co., LMSC-B303910 (Aug. 1972)

the device resistance through very large changes in detector time constant). This mechanism is also inconsistent with the disappearance of minority carrier sweepout, which implies minority carrier trapping.

Minority carrier trapping resulting in increased excess majority carrier lifetime is frequently observed in II-VI and III-V compounds, is occasionally observed in silicon and germanium, and is usually attributed to the presence of a sensitizing center, e.g., a double acceptor in n-type material [Reference 15].

A doubly negative center can readily capture a hole. After doing so, an electron can in turn be captured, but since the center still has a negative charge, the probability of its doing so is small. The electron lifetime for such a capture will therefore be long (seconds). The center, when occupied by one hole, is thus a long-lived recombination center for electrons. If a second hole is captured by the center, it becomes neutral and can rapidly capture an electron, again quickly becoming a repulsive, long-lived recombination center for electrons.

A sensitizing center of this type produces a dependence of time constant on background given by $\tau_n = k/\phi$, and thus is not adequate, by itself, to explain a time constant dependence on background to a fractional power. This mechanism does however produce the very long lifetimes observed in HgCdTe, and most attempts to model the HgCdTe trapping mechanism have been attempts to perturb the simple sensitizing center to produce the required fractional power background dependence.

It has been suggested for example that non-uniform absorption of the incident light might provide the required perturbation [Reference 11].

The light used for most experiments on HgCdTe is highly absorbed, placing a greater density of hole-electron pairs near the front of the detector than at

---

[15] A. F. Sklensky and R. H. Bube, "Photoelectronic Properties of Zinc Impurity in Silicon," Phys. Rev. B., Vol. 6, No. 4, 1328-1366 (15 Aug 1972)

the back. If, in addition, the distribution of sensitizing centers is uniform and the hole mean free path prior to localization is short, it would be expected that the centers near the front of the detector would be saturated at a lower incident background intensity than those at the back, and a change in the exponent of the power law variation might result. However, experiments have shown [Reference 14] that penetrating radiation produces the same power law variation given in Eq. (1) with only a change in the value of the constant k. The minority carrier diffusion length is apparently sufficiently long to distribute the optically generated carriers from the front of the crystal to the back.

It has also been suggested that local variations in the density or capture cross sections of the sensitizing centers might change the exponent in the power law variation. Local variations in defect density and type, and variations in composition, are to be expected in a complex ternary semiconductor such as HgCdTe, and evidence indicating local variations in lifetime and quantum efficiency confirm the presence of material variations [Reference 14]. These do not, however, appear large enough or consistent enough to explain the lifetime dependence. The reported power law is obtained consistently from detector to detector and wafer to wafer. Further, the value of α remains constant in given detectors for intensity variations spanning nearly five orders of magnitude. That kind of regularity is particularly difficult to attribute to material irregularities.

Rose has shown [Reference 16] that the simple sensitizing center model can be modified to yield a power law dependence of the time constant on flux with an exponent between $-\frac{1}{2}$ and -1 if the density of the sensitizing centers is distributed exponentially in energy within the bandgap. Beck [Reference 17] and Broudy and Beck [Reference 18] have applied this idea to HgCdTe detectors in

---

[16]A. Rose, "An Outline of Photoconductive Processes," RCA Rev. 363 (1951)

[17]J. D. Beck, "Effects of Temperature and Background Photon Flux on the Photoconductive Response Time in (Hg,Cd)Te," S.M. Thesis, Dept. of Elect. Eng., MIT, Cambridge (May 1972)

[18]R. M. Broudy and J. D. Beck, "Trapping Photoconductivity in (Hg,Cd)Te," Proc. IRIS Detector Specialty Group Meet., Washington, DC (May 1973)

some detail. In their results, the fractional exponent to which the background flux is raised to obtain the time constant is a function of device temperature. Data reported in this work however indicate that the exponent observed is not temperature dependent.

Finally, it has been suggested that the interaction of the surface potential with a bulk sensitizing center may yield a model with the appropriate background dependence. A simple modification of the surface state density or distribution is not likely to be adequate because of poor communication between the surface and the bulk. If, however, the dominant time constant is set by the relative positions of the trap energy and fermi level in the surface potential region, then the background may be only fractionally effective. The surface potential has been shown to affect the device responsivity [References 19 and 20] and hence its time constant. It is the purpose of this work to obtain further information on the effects of surface potential on detector parameters, and on the consequences of irradiating these devices with ionizing radiation.

---

[19]A. F. Tasch, et al., "Field-Effect Measurements on the HgCdTe Surface," J App. Phys., 41, 4202-4204 (Sept. 1970)
[20]A. A. Pellegrino, "Surface Related Effects in (Hg,Cd)Te," S.M. Thesis, Dept. of Elec. Eng., MIT, Cambridge (May 1974)

EXPERIMENTAL PROCEDURE

Test Devices

The device configuration chosen to study the surface properties and detector performance of trapping mode detectors is shown in Figure 2. The entire configuration is fabricated on one die taken from a wafer which produced other trapping mode detectors. Each die, in effect, consists of three detectors: the field modulated detector AB (an MIS device with a semitransparent gate), a ZnS covered detector d-e, and an uncoated detector e-f. The surfaces of the three devices all received the same surface treatment. In fact the same surface treatment is given to all devices regardless of alloy composition. Since these detectors are not normally coated with ZnS, detector e-f is in effect the experiment control detector. Detector d-e will show whether or not a ZnS coating affects detector performance. Finally detector AB (or b-c) is used for surface state studies. This MIS device has a nominal capacitance of about 20 pF. The Au field plate is sufficiently thin so that about 10% of 3 μm radiation can reach the detector. The underlying HgCdTe is approximately 18 μm thick.

Four device arrays with the configuration shown in Figure 2 were purchased from Carson-Alexiou Detection Science Inc. (formerly A. D. Little Detection Sciences). Two arrays had an alloy composition resulting in an energy gap of 0.3 eV while the other two arrays had an alloy composition yielding devices with 0.1 eV energy gap. Data, however, could only be obtained on one array of each composition. The MIS devices on the other two arrays had such high leakages that data could not be obtained. All the detectors on the two usable arrays displayed trapping mode behavior at appropriate backgrounds and temperatures.

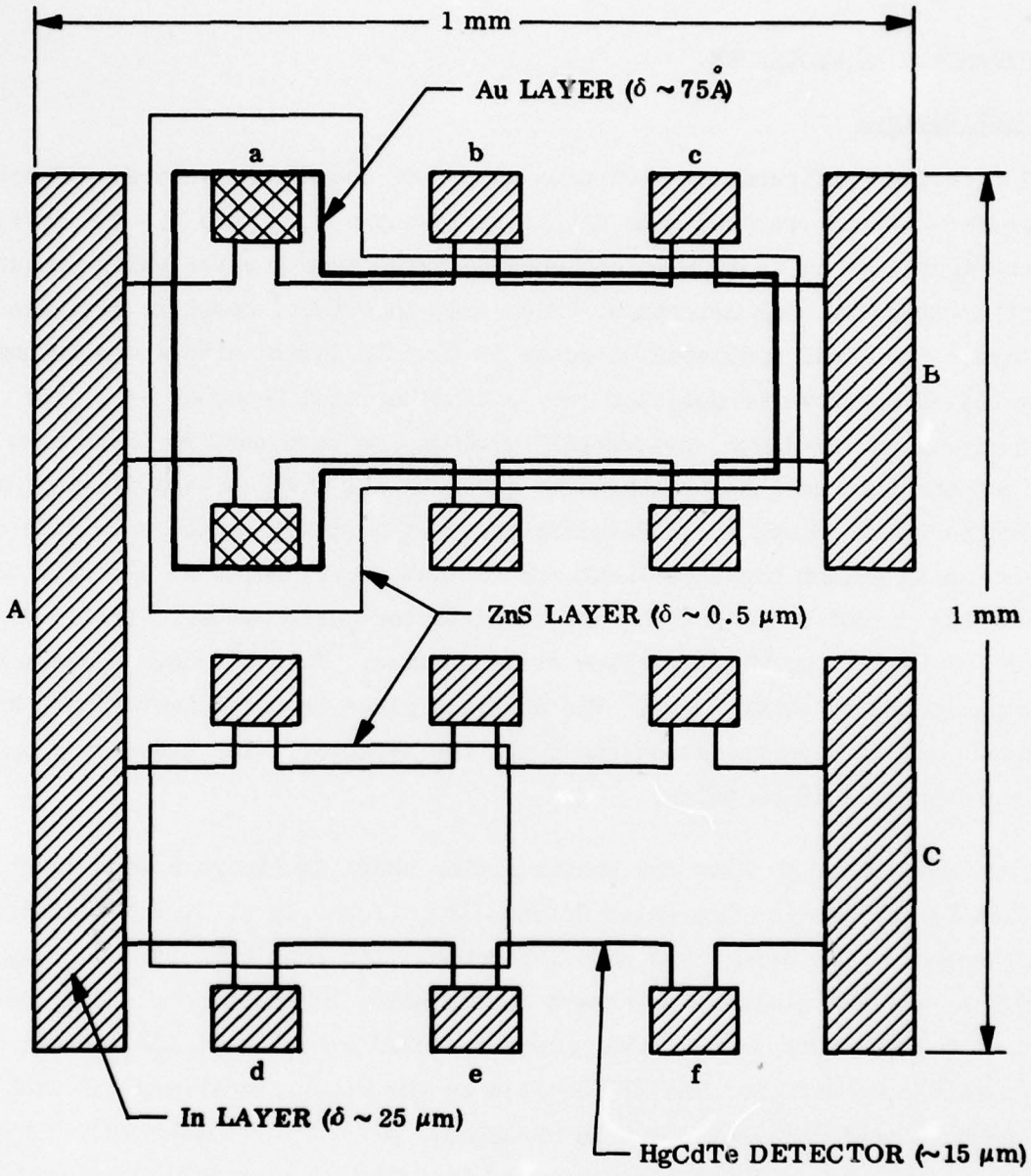

Figure 2. HgCdTe detector and MIS configuration

Detector Characterization

The detector parameters of most concern to this program are: voltage responsivity vs. frequency, and noise spectral density vs. frequency measured at low temperatures and low optical backgrounds. The temperature dependence of responsivity and optical background dependence of majority carrier lifetime are also of interest. The apparatus used to obtain these data is shown in Figures 3 and 4.

Figure 3 shows in detail the low optical background detector chamber used in this study. This dark chamber is fastened to the cold plate of a "Cryoflask" dewar. The optical background in the dark chamber (once cooled to low temperature) is determined by the transmission of the bandpass filter, a neutral density filter, the size of the cooled aperture, and the external temperature seen by the detector. The background could easily be varied from 10^{11} ph/cm^2 sec to 10^{13} ph/cm^2 sec with the ambient 300°K background as the radiation source. Backgrounds in excess of 10^{16} ph/cm^2 sec could be obtained using the blackbody as a radiation source. The bandpass filter used in this study transmitted from 3.1 to 4.0 μm.

Figure 4 schematically shows the detector test apparatus. In the measurement of responsivity the detector is exposed to a small (compared to the background flux density) modulated optical signal from the blackbody (T = 500°K). The magnitude of this signal is computed from the measured characteristics of the bandpass filter, the temperature of the blackbody, the blackbody aperture size, and the blackbody-to-detector spacing. The time varying voltage developed across the biased detector as a result of excitation by the modulated optical signal is amplified by a low-noise preamp (PAR Mod. 118) and the voltage synchronously detected by the lock-in amplifier (PAR Mod. 124A). The lock-in output is either read with a digital voltmeter or recorded on a strip chart recorder. This initial measurement is made at a convenient low frequency, generally 100 Hz. Subsequently the blackbody radiation source is removed, and radiation from an InAs diode emitter is used

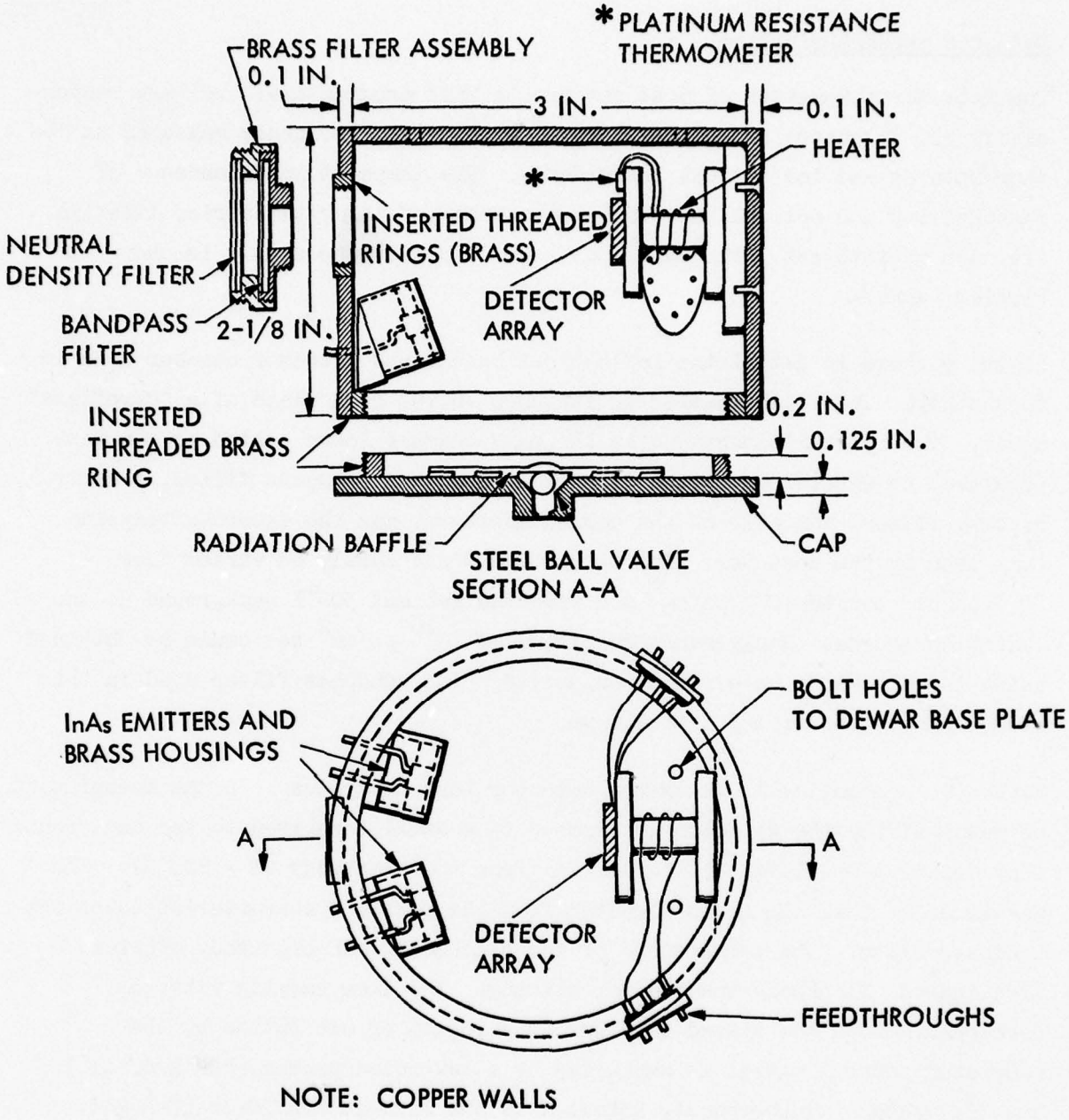

Figure 3. Low background test chamber

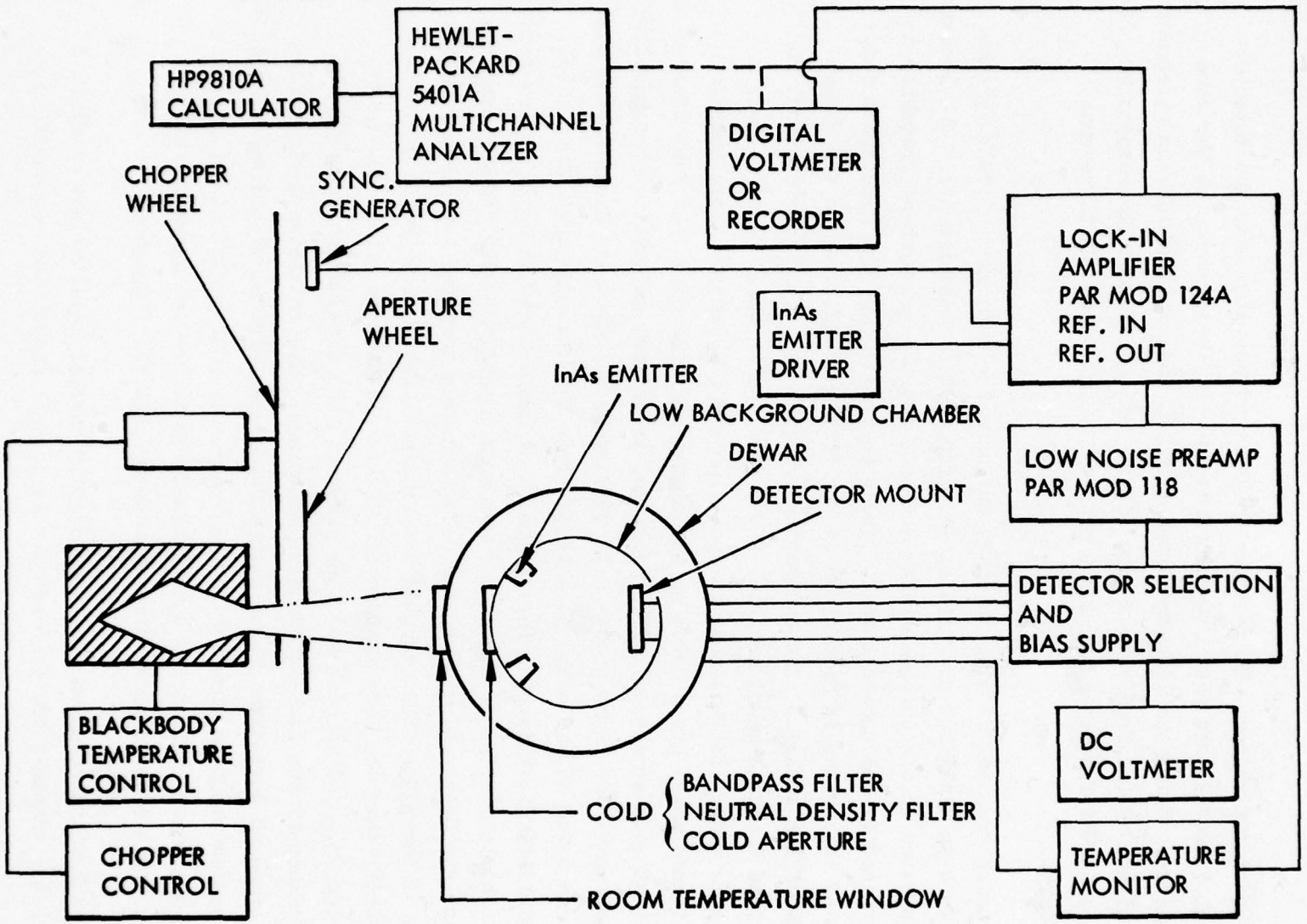

Figure 4. Experimental setup for detector measurements

as the signal source. The emitter drive is adjusted so that the detector output is lower than that obtained from the blackbody source at the same frequency. Using the lock-in in the internal mode, and the lock-in reference out signal as the frequency source for the emitter driver, the responsivity as a function of frequency is easily obtained from about 5 Hz to several kilohertz.

The noise spectral density is measured using the same bias circuit, preamp, and lock-in amplifier as was used for responsivity measurements. The lock-in is operated in the internal reference mode and the measurement frequency is determined by the chosen lock-in detection frequency. The electrical bandpass of the system is determined by the time constant used in the output stage of the lock-in. The bandpass was ≥ 1.25 Hz. The lock-in output is fed into a multichannel analyzer (MCA) operated in the sampled voltage analysis mode. In this mode of operation the MCA samples those voltage amplitudes which are present in the signal and determines how much time is spent at each amplitude. The result is, in effect, an amplitude probability histogram of the input signal. In this study the noise is Gaussian, and thus the rms value of the noise is obtained from the standard deviation of the probability distribution. (The system is ac coupled resulting in a zero mean distribution.) The HP calculator which is interfaced with the MCA computes a best fit Gaussian curve to the data, and then computes the standard deviation of the data. The computed Gaussian best fit is superposed on the data to verify that the data is, indeed, Gaussian and that no extraneous noise sources (e.g., 60 Hz pick-up) were present. The measurement frequency is determined by the lock-in frequency settings. The rms noise derived from the standard deviation of the distribution when divided by the square root of the system bandpass then yields the "noise per root hertz" at the frequency of measurement. The noise spectral density curves are generated by following the above procedure for each measurement frequency.

The background dependence of the majority carrier lifetime was determined using the responsivity test setup. As is well known, the responsivity at

sufficiently low frequencies is directly proportional to the majority lifetime. Thus, the dependence of lifetime on background can be obtained from a measurement of the small signal detector voltage output vs. background (as long as the detector resistance remains constant). Determination of the dominant lifetime in the detector will be discussed later.

Capacitance Measurements

The capacitance voltage characteristic of the MIS structure will be used to determine both the surface state density and surface potential vs. gate voltage on HgCdTe. In this section we describe only the apparatus, leaving the discussion of analysis to a later section.

The low frequency (5 Hz to 10 kHz) capacitance measurement apparatus is illustrated schematically in Figure 5 a. A small ac signal derived from the lock-in reference output is applied to the MIS device. The ac current through the device is then measured by using a current mode preamp in conjunction with the lock-in amplifier. The current in phase with the input signal is proportional to the conductance of the device, while the 90° out-of-phase component is proportional to ωC where C is the device capacitance and $\omega = 2\pi f$. Provision is made to simultaneously apply a dc voltage to the MIS device. Figure 5 b shows the biasing circuit used. The unity gain summing amplifier has a bandwidth of 1 MHz. The dc voltage is derived from a motor driven potentiometer. With the sample in the dewar, capacitance resolution of about 0.05 pF can be obtained at 5 Hz. This resolution limit is imposed by noise on the signal at low frequencies. Better resolution can be obtained at higher frequencies. The system was calibrated against a 10 pF standard air gap capacitor. Repeatability was better than 0.5% and was limited by how accurately the input signal could be set.

Early measurements showed that the test signal had to be less than 5 mV rms in order to avoid non-linear effects in the MIS structure. All low-frequency measurements reported here were made with 2 mV rms test signals. In general, the lock-in output is fed into the Y axis of an X-Y recorder while the ramp

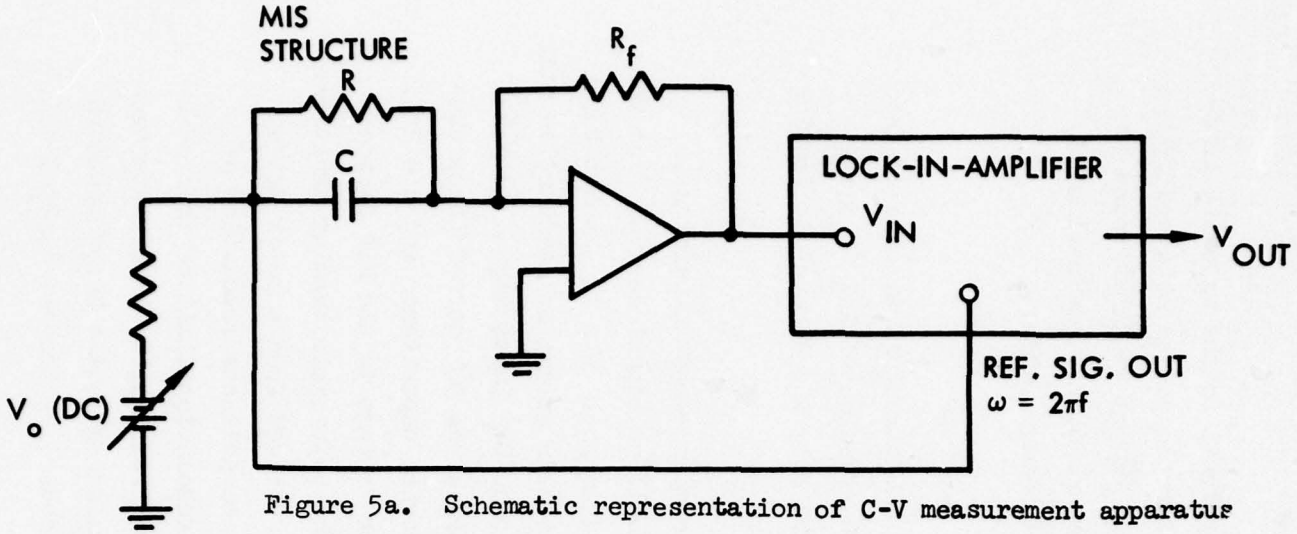

Figure 5a. Schematic representation of C-V measurement apparatus

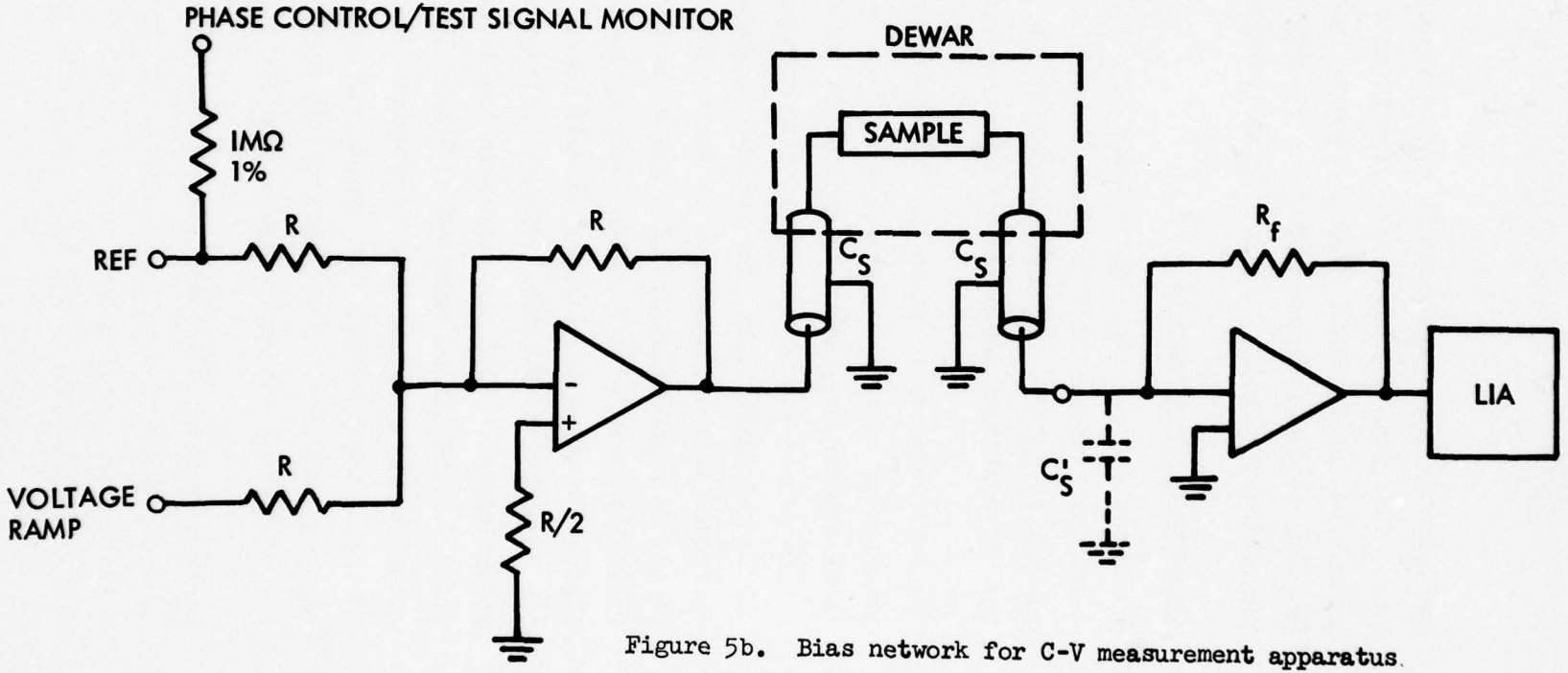

Figure 5b. Bias network for C-V measurement apparatus

voltage is fed into the X axis, giving a continuous measurement of capacitance vs. voltage. However, at low frequencies, because of the long integration times used ($\sim$ 4 min), point-by-point data were taken.

High-frequency (1 MHz) capacitance data were obtained with a Boonton Model 75A-S8 capacitance bridge. A 2.5 mV rms test signal was also used in these measurements.

EXPERIMENTAL RESULTS

Surface Potential Variation

Capacitance vs. Voltage

The simple MIS structure is an effective tool for measurement and variation of surface potential. The semiconductor surface potential is controlled by the gate electrode potential, V_g, through the relation:

$$V_g = \Psi_s + \frac{Q_\square(\Psi_s)}{C_i} + V_{off} \tag{2}$$

where $Q_\square(\Psi_s)$ is the total semiconductor bulk space charge and surface charge at a surface potential of Ψ_s and C_i is the insulator capacitance. The offset voltage, V_{off}, may be due to a combination of metal-semiconductor work function difference and fixed, trapped charge at the semiconductor-insulator interface. It is possible to obtain the relation between V_g and Ψ_s by a measurement of device capacitance, C, as a function of gate voltage through

$$\frac{C(V_g)}{C_i} = \frac{dQ_\square/d\Psi_s}{C_\perp + dQ_\square/d\Psi_s} \tag{3}$$

where the semiconductor charge may be explicitly separated into a bulk component and a surface component through:

$$Q_\square = Q_\square(\text{bulk}) + Q_\square(\text{surface}) \ . \tag{4}$$

$Q_\square(\text{bulk})$ may be calculated as an explicit function of Ψ_s given the HgCdTe band structure parameters [21]. Similarly, $Q_\square(\text{surface})$ may be calculated as an explicit function of Ψ_s given the surface state type (donor or acceptor) and density distribution. When the surface state density varies negligibly over a potential interval $\Delta\Psi_s = kT/q$, a significant simplification occurs through

$$\frac{dQ_\square(\text{surface})}{d\Psi_s} \approx qN_{ss}(\Psi_s + E_F) \quad , \tag{5}$$

---

[21] M. Michael and W. F. Leonard, Solid-State Electronics 17, 71 (1974)

an expression which is exact at $T = 0^{\circ}K$.

Full mathematical details are given in the appendix. A graphical presentation of the interrelations between $C(V_g)/C_i$, V_g, Ψ_s, and $N_{ss}(E_s)$ is given in Figure 6. The total surface state density distribution function, $N_{ss}(E_s)$, is composed of two components: a donor type surface state density distribution, $N_{ssD}(E_s)$, and an acceptor type surface state density distribution, $N_{ssA}(E_s)$.

The C/C_i vs. V_g curve of Figure 6 is a "low frequency" curve, i.e., the surface states are in thermal equilibrium with the semiconductor bulk and the surface state occupation follows the ac modulation or measuring signal. A first estimate of the midband value of $N_{ss}(E_{ss} \approx -E_g/2)$ may be obtained from the capacitance minimum since

$$\frac{dQ_{\square}(\text{surface})}{d\Psi_s} \gg \frac{dQ_{\square}(\text{bulk})}{d\Psi_s}$$

in depletion in all HgCdTe MIS devices we have examined. Also, when C/C_i is dominated by surface states, the width of the C/C_i curve is of the order

$$\Delta V_g \approx \frac{q}{C_i} \int_{-E_g}^{0} N_{ss}(E_s)\,dE_s$$

which gives an estimate of the total number of surface states. This data may be used to construct a first estimate of $N_{ss}(E_s)$ from which a C/C_i vs. V_g curve is then calculated for comparison with the experimental data. A large number of calculations have indicated that Ψ_s vs. V_g is not a sensitive function of the detailed shape of $N_{ss}(E_s)$ so that the correction to $N_{ss}(E_s)$ may be obtained from the difference between C/C_i (experimental) and C/C_i (first calculation) at each $\Psi_s(V_g)$ point. We have found a reasonable fit of calculated to experimental C/C_i curves for surface state density distributions of the form

$$N_{ssA} = S_A \Big/ \sqrt{\left(\frac{E_s - E_A}{\Delta_A}\right)^2 + 1} \qquad (6)$$

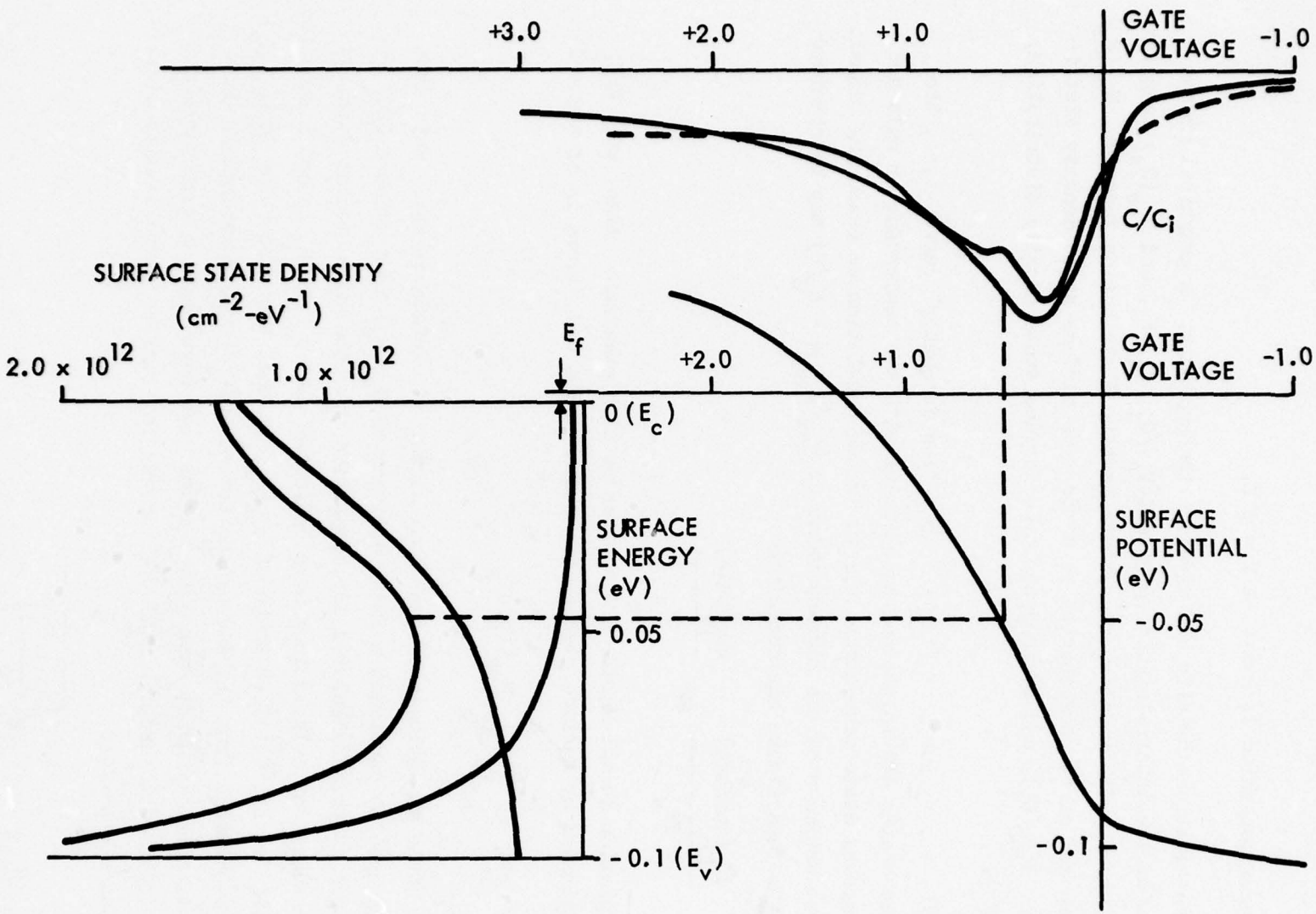

Figure 6. Graphical presentation of interrelations between capacitance, C/C_i, gate potential, V_g, surface potential, V_s, and surface state distribution $N_{ss}(E_s)$

for acceptor type states and

$$N_{ssD} = S_D \Big/ \sqrt{\left(\frac{E_s - E_D}{\Delta_D}\right)^2 + 1} \qquad (7)$$

for donor type states. The quantities S_A and S_D give the maximum surface state densities, E_A and E_D give the energy position of the density distribution maxima and Δ_A and Δ_D determine the width of the distributions.

In Figures 7 - 9 we show the measured and calculated C/C_i vs. V_g curves for a SWIR MIS device at three temperatures. In all three figures, a "typical" MIS device characteristic is obtained with well defined "high frequency" and "low frequency" regimes [22]. At T = 155°K and 80°K, the experimental "low frequency" regime is reached as indicated by the merging of several curves with the 5 Hz curve. However, at T = 8°K, "low frequency" behavior is not reached at 5 Hz, our lowest measurement frequency available. "Low frequency" behavior is obtained when the reciprocal of the measurement frequency is small compared to minority carrier generation times due to thermal or optical processes. Figures 7 - 9 were all taken with a background photon irradiance of $\varphi_B = 10^{13}$ cm^{-2} sec^{-1}.

For the SWIR device, bulk thermal equilibrium electron concentration, n_B, was determined by the high-frequency inversion regime capacitance at 80°K from Figure 8. This value, characteristic of the surface to depth of 0.25 μm, is in reasonable agreement with a van der Pauw type measurement as shown in Table 1. The insulator capacitance, C_i, was determined at low frequencies in strong inversion. The MIS device capacitance, C, does not saturate to C_i in accumulation as may be seen in Figures 7 - 9. This is due to the small conduction band density of states function in narrow band gap HgCdTe. Also apparent in Figures 7 - 9 is a significant temperature dependence of C_i. The temperature coefficient of capacitance,

---

[22] A. S. Grove, E. H. Snow, B. E. Deal, and C. T. Sah, J. Appl. Phys. 35, 2458 (1964)

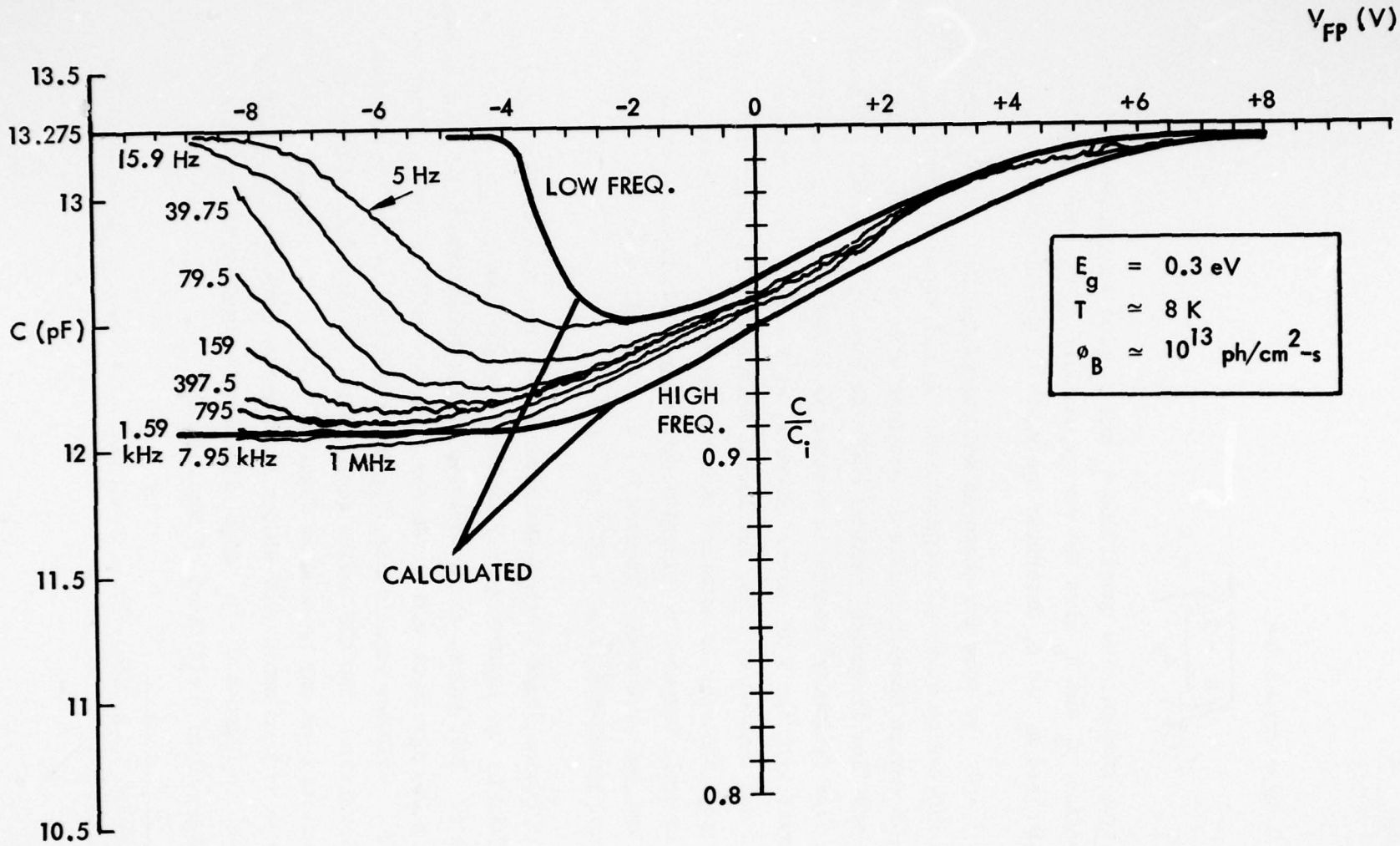

Figure 7. Capacitance-voltage characteristic of SWIR MIS device near liquid He temperature ($T \approx 8^{\circ}K$) with measurement frequency as a parameter

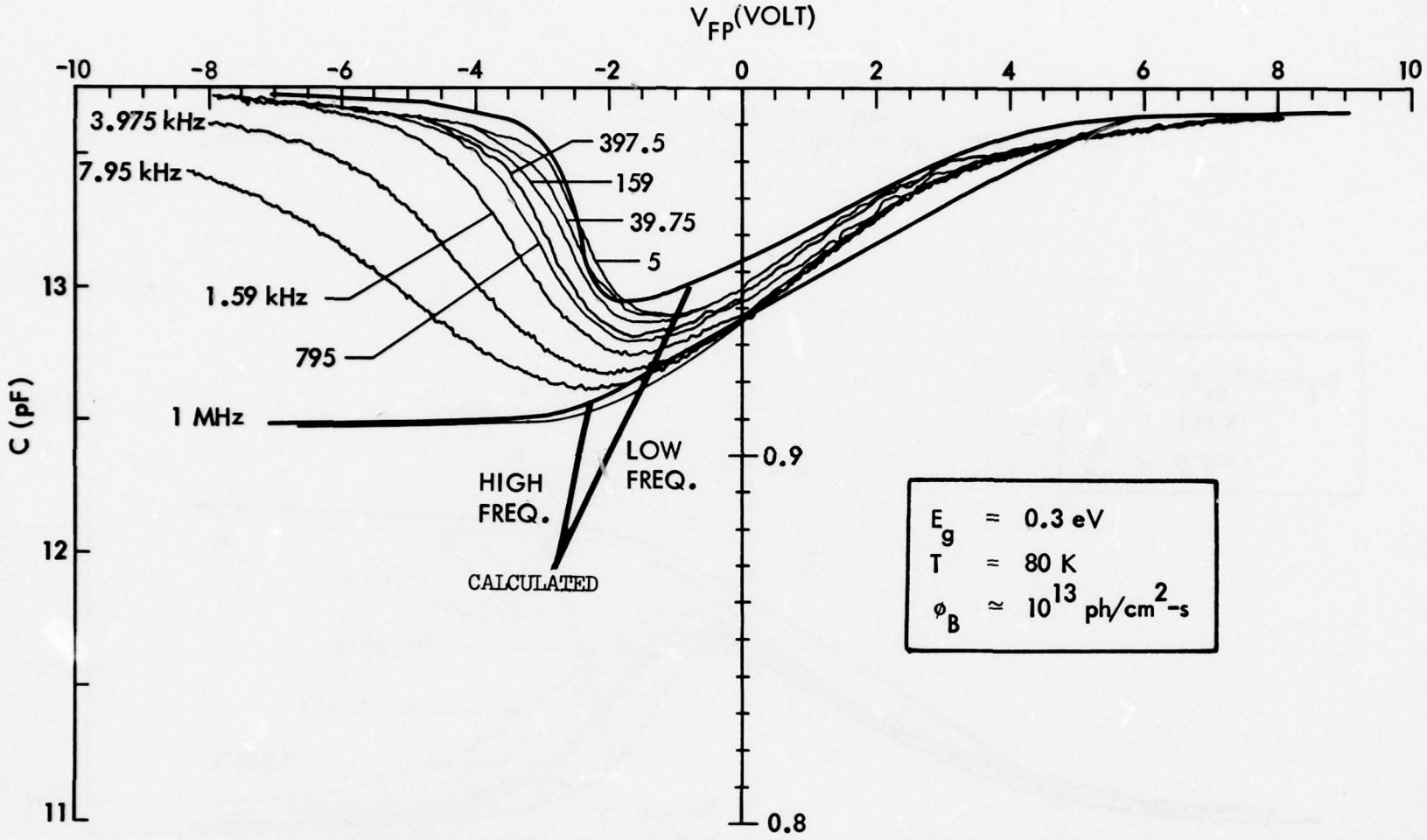

Figure 8. Capacitance-voltage characteristic of SWIR MIS device near liquid N_2 temperature (T ≈ 80° K) with measurement frequency as a parameter

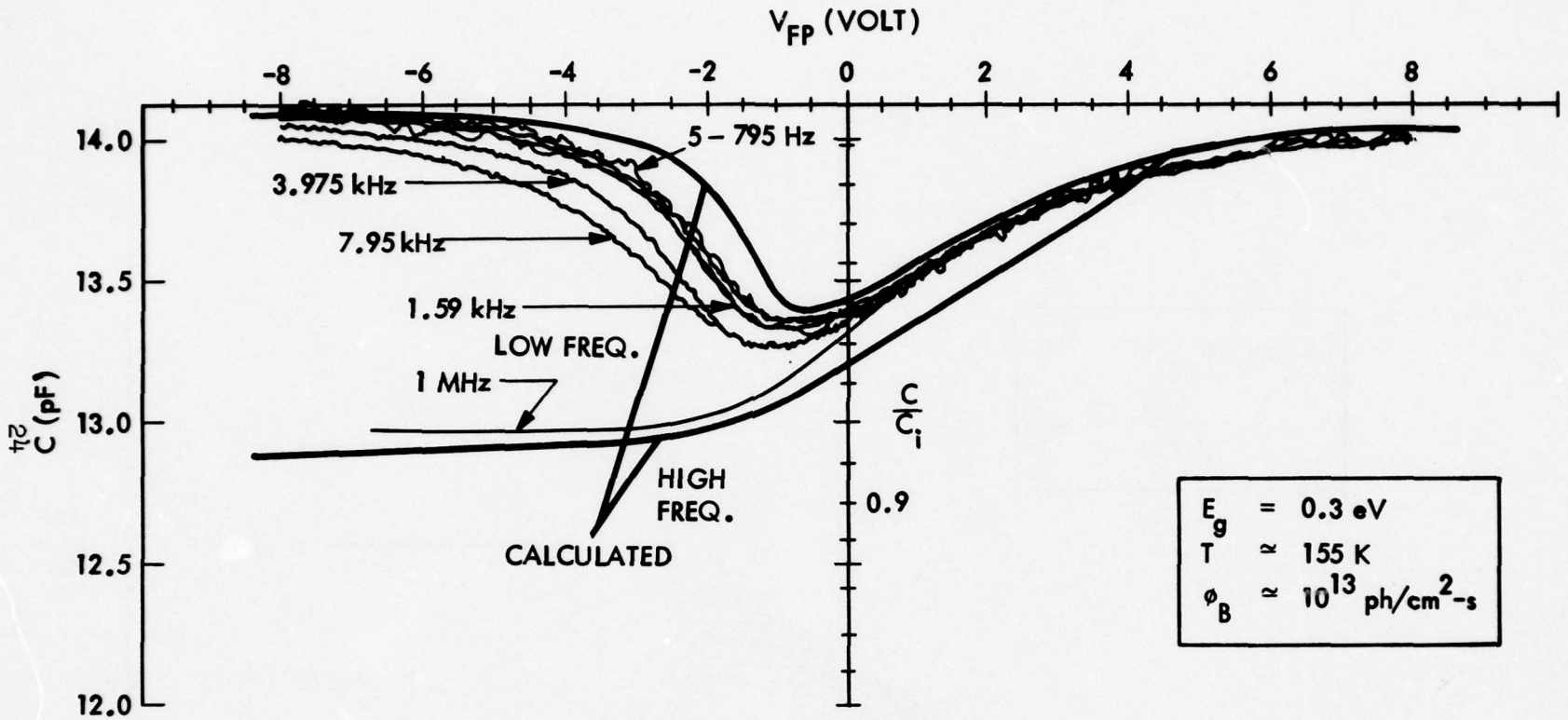

Figure 9. Capacitance-voltage characteristic of SWIR MIS device at "high" temperature ($T \approx 152^\circ K$) with measurement frequency as a parameter

TABLE 1.

COMPARISON OF BULK ELECTRON CONCENTRATIONS DETERMINED BY VAN DER PAUW TECHNIQUE AND BY HIGH FREQUENCY C vs. V_g ON MIS STRUCTURE

	SWIR	LWIR
MIS	9.3×10^{15} cm^{-3}	1.7×10^{14} cm^{-3}
van der Pauw	1.6×10^{16} cm^{-3}	2.7×10^{14} cm^{-3}

$$\frac{1}{C_i}\frac{dC_i}{dT} \approx 4 \times 10^{-4}\,{}^{\circ}K^{-1}$$

is due to the temperature dependence of the insulator (ZnS) dielectric constant [23,24].

Using the appropriate values of T and $C_i(T)$, the low frequency and high frequency C vs. V curves of Figures 7-9 were calculated from the single set of surface state parameters in the first column (pre irradiation) of Table 2. If the entire offset voltage, V_{off}, is due to trapped charge at the semiconductor-insulator interface, the offset corresponds to $\Delta N_s = 1.2 \times 10^{11}$ cm^{-2} negative charges in the insulator. The agreement between calculation and experiment over the temperature interval $10^{\circ}K \leq T \leq 155^{\circ}K$ and at the low and high frequency extremes is satisfactory. It should be noted that the abrupt drop of the high frequency calculated C below the experimental 1 MHz curve as the MIS gate voltage moves from accumulation to depletion is due to the assumption that the surface states are abruptly disconnected from the semiconductor bulk at $\Psi_s = 0$.

In Figures 10 and 11 we show the experimental and calculated C-V_g characteristics for the SWIR device before and after a 200 kR γ-irradiation. The experimental points in Figure 11 are the superposition of data following two separate irradiations with an intervening room temperature anneal. The pre irradiated C-V characteristic of Figure 10 is indistinguishable from the post irradiation C-V characteristics following a room temperature anneal. An increased surface state density in the irradiated sample is indicated by the shallower dip at C_{min} and wider gate potential variation, ΔVg, in Figure 11 vis á vis that in Figure 10. The surface state parameters required for the pre and post irradiated calculated C-V characteristics are listed in Table 2 and the surface state density distributions are plotted in Figure 12. The corresponding surface potential variation is shown in Figure 13. The principal effect of

---

[23]I. B. Kobyakov and G. S. Pado, Sov. Phys.-Solid State 9, 1707 (1968).
[24]A. Goswami and P. Goswami, Thin Solid Films 16, 175 (1973).

TABLE 2

BULK AND SURFACE STATE PARAMETERS OF HgCdTe MIS DEVICES

	SWIR		LWIR	
	PRE IRRADIATION	POST IRRADIATION	PRE IRRADIATION	POST IRRADIATION
E_g (eV)	0.3		0.1	
T (°K)	80		10	
n_B (cm^{-3})	9.3×10^{15}		1.7×10^{14}	
ϵ_s	18		18	
C_i (f/cm^2)	6.4×10^{-9}		1.45×10^{-8}	
S_A ($cm^{-2} \cdot eV^{-1}$)	2×10^{12}	2×10^{12}	1.45×10^{12}	1.5×10^{12}
E_A (eV)	0	-.025	0	0
Δ_A (eV)	.01	.01	.02	.02
S_D ($cm^{-2} \cdot eV^{-1}$)	1×10^{12}	4×10^{12}	1.6×10^{12}	8×10^{12}
E_D (eV)	-0.3	-0.3	-0.1	-0.1
Δ_D (eV)	.0075	.0075	.005	.005
V_{off} (volts)	3.6	4.0	0.56	1.8
ΔN_s (cm^{-2})	1.2×10^{11}	1.35×10^{11}	5.1×10^{10}	1.63×10^{11}

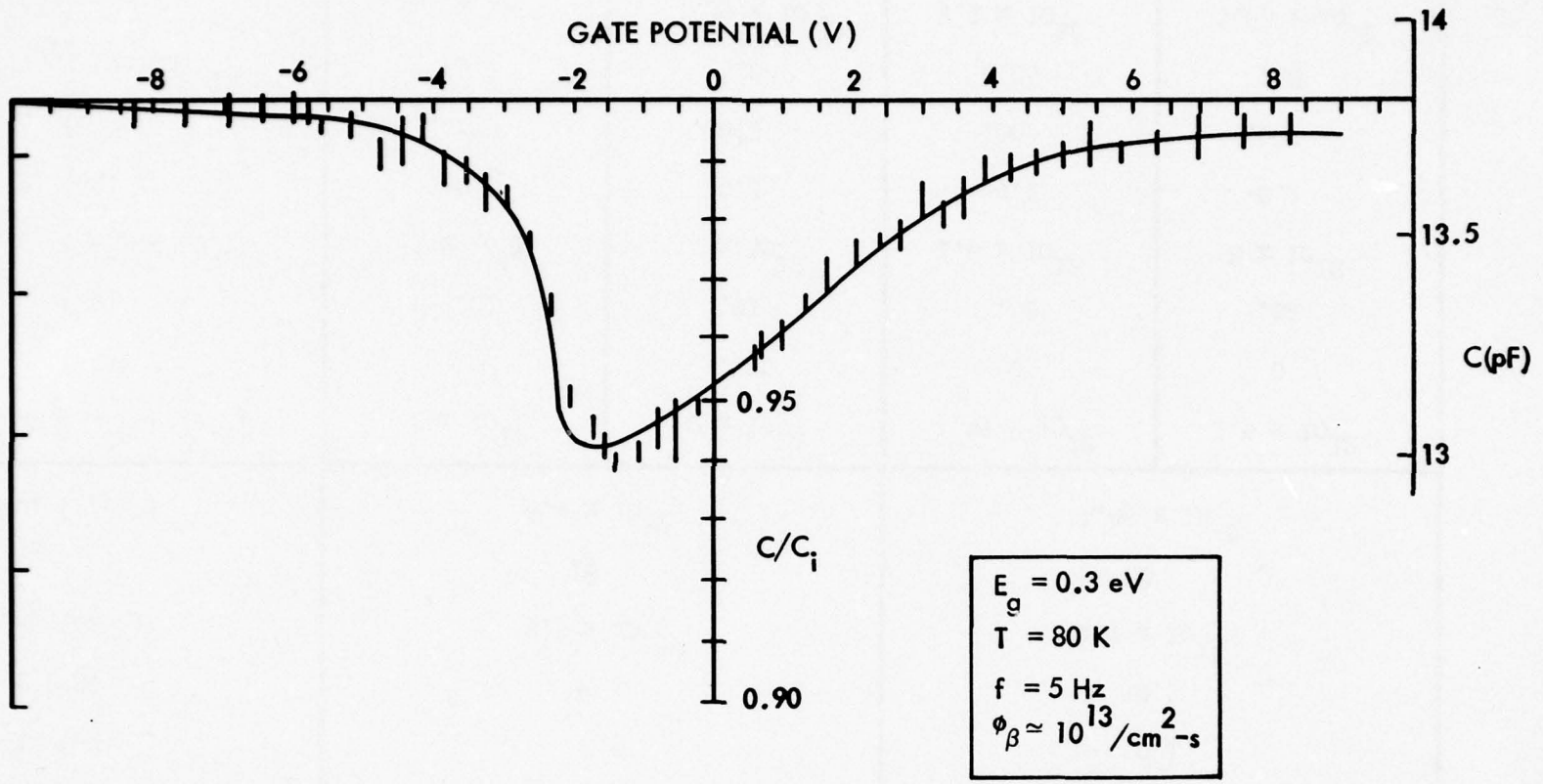

Figure 10. Low frequency capacitance-voltage characteristic of SWIR MIS device before γ-irradiation

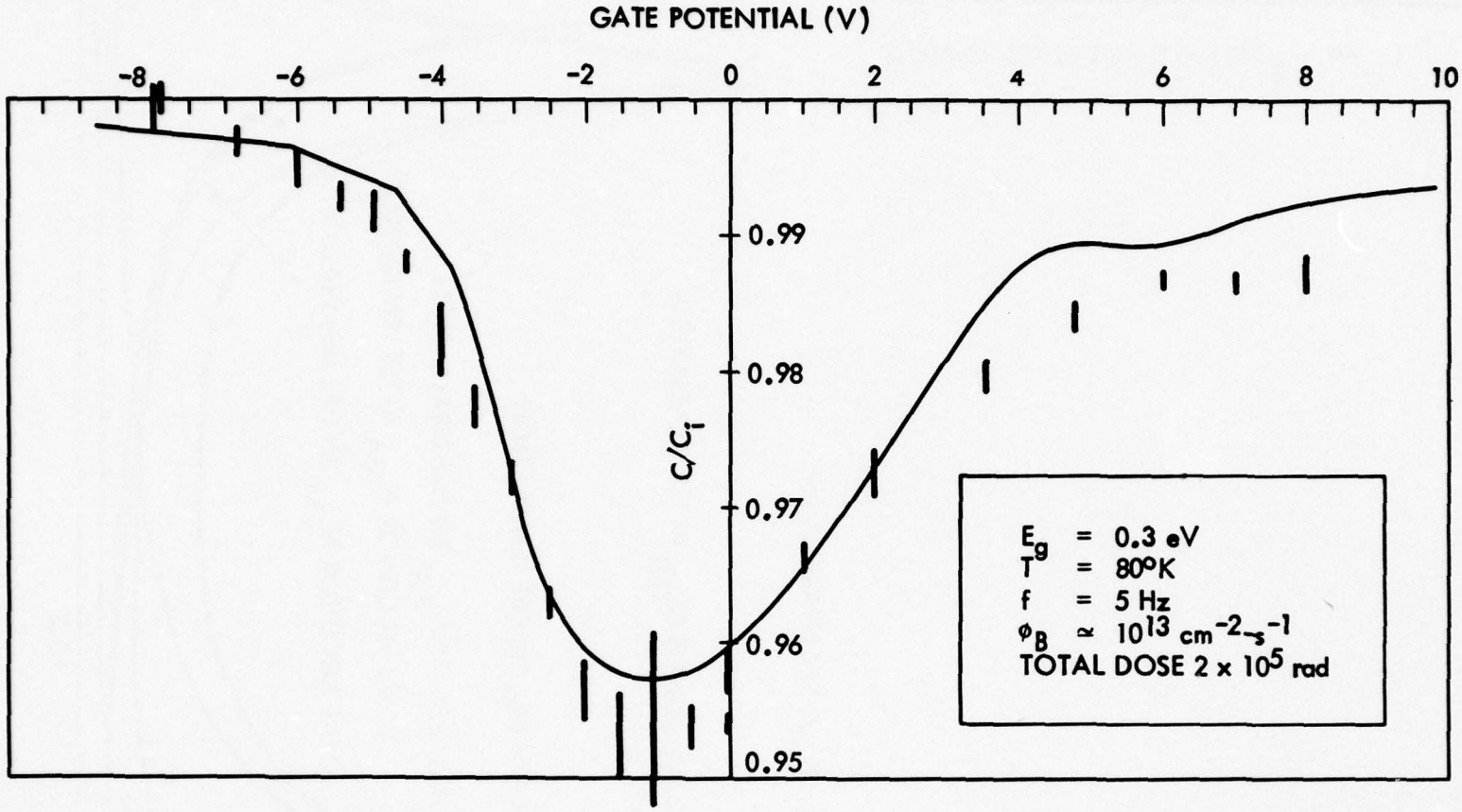

Figure 11. Low frequency capacitance-voltage characteristic of SWIR MIS device after 200 kR γ-irradiation

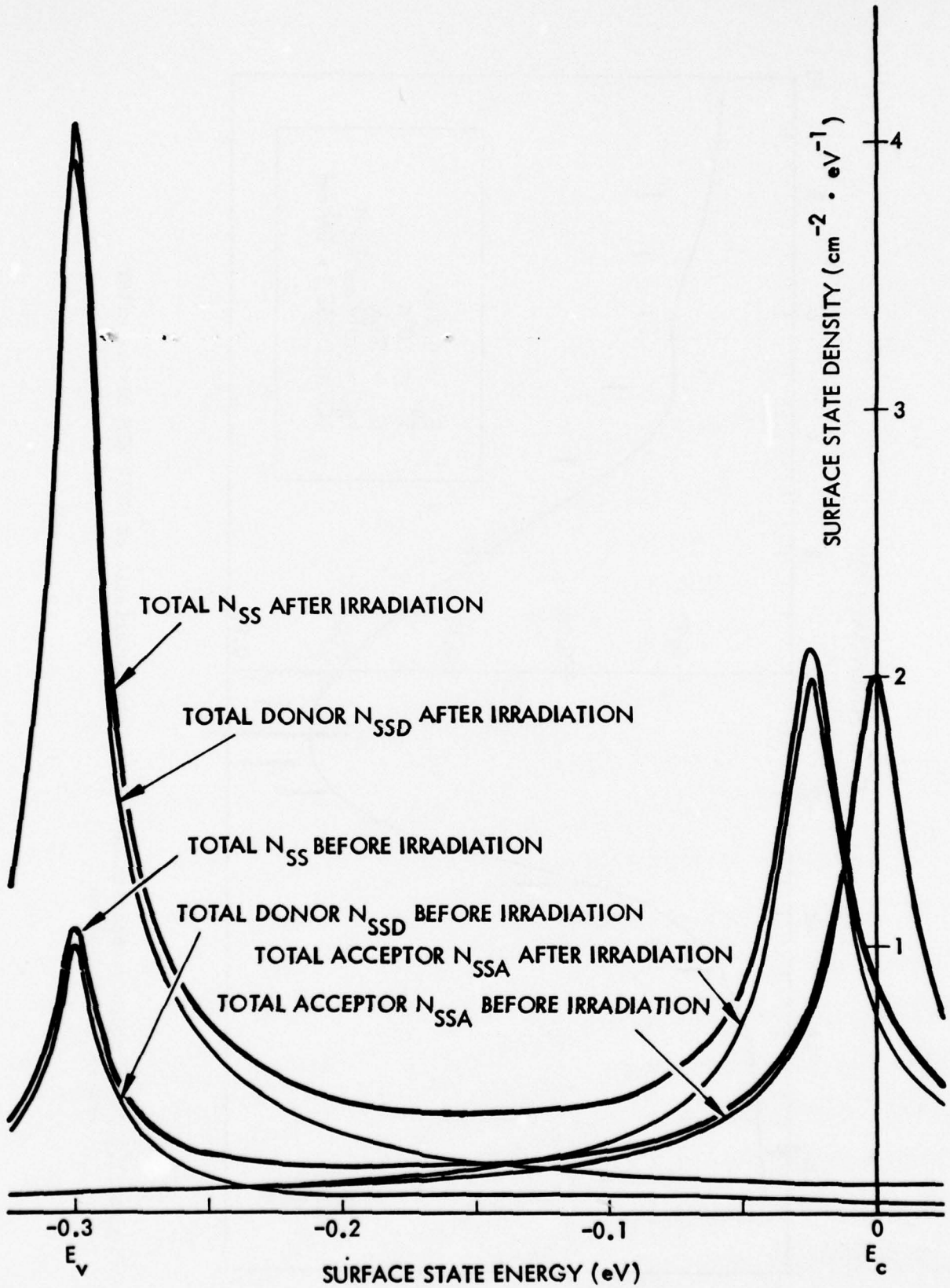

Figure 12. Surface state density distributions of SWIR MIS device before and after 200 kR γ-irradiation

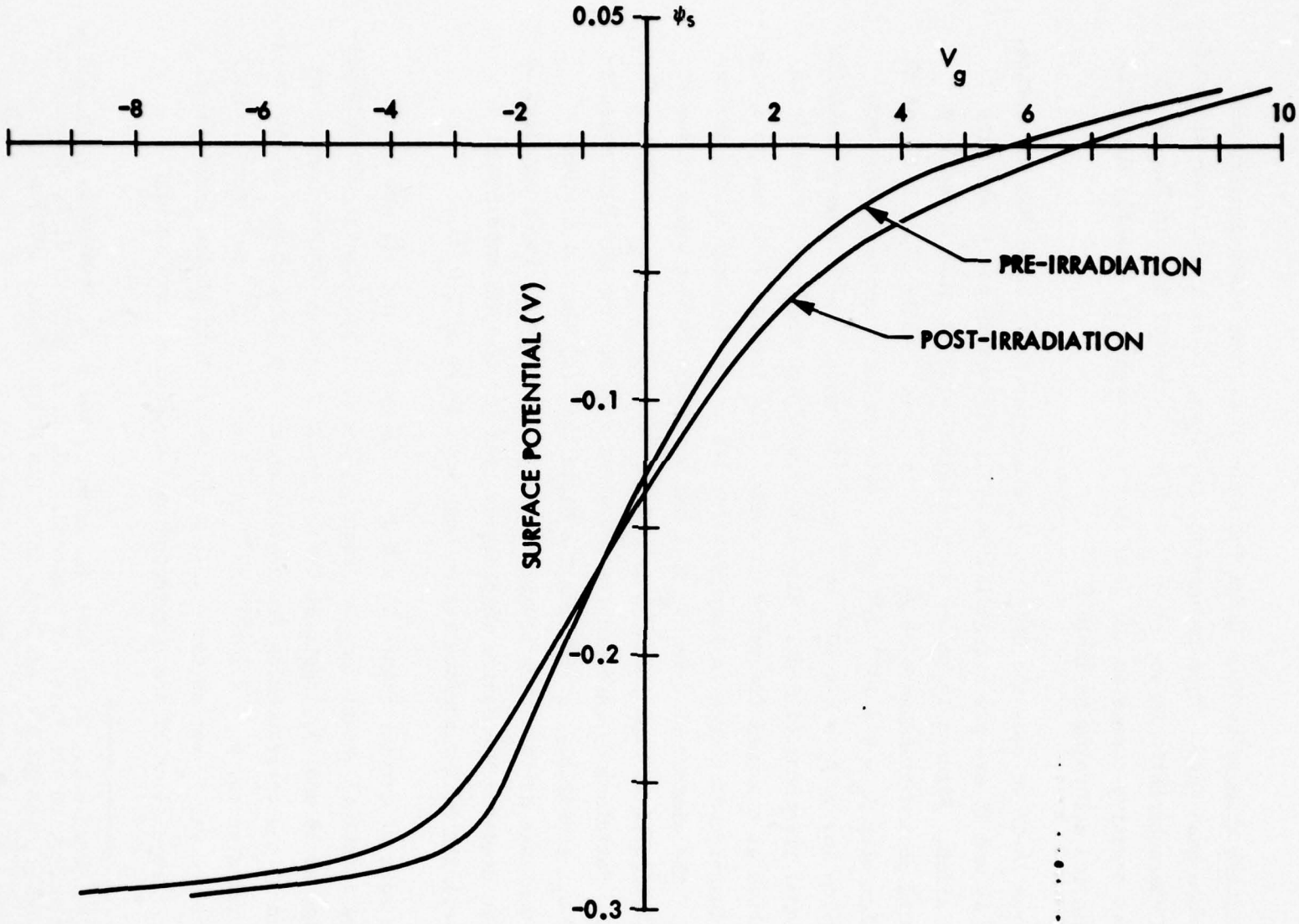

Figure 13. Surface potential as a function of gate voltage of SWIR MIS device before and after 200 kR γ-irradiation

γ-irradiation appears to be a large increase in surface state density near the valence band edge. This is apparent in Figure 11 as a shallower slope of the C-V characteristic in the $-4 < V_g < -2$ volt interval than in Figure 10. The fixed negative charge in the insulator increased only slightly following γ-irradiation according to Table 2.

In Figures 14-17 we show the C/C_i vs. V_g characteristics of a LWIR MIS device. Figures 14 and 15 are pre γ-irradiation while Figures 16 and 17 are post γ-irradiation. Figures 14 and 16 were obtained with the MIS device in a background photon irradiance of $\phi_B = 10^{13}$ cm^{-2} sec^{-1} while Figures 15 and 17 were taken with $\phi_B = 2 \times 10^{12}$ cm^{-2} s^{-1}. Note that the carrier generation rate is too low at $\phi_b = 2 \times 10^{12}$ cm^{-2} sec^{-1} to reach "low frequency" behavior at a signal frequency of 5 Hz. Also note that "high frequency" behavior is not reached at a signal frequency of 1 MHz. This is presumably due to a significant tunnel conductance in inversion for the narrow bandgap HgCdTe devices [25,26]. The minimum of C vs. V_g at 1 MHz in Figure 14 was taken as due to the depletion layer capacitance only and the corresponding n_B calculated for Table 1. Satisfactory agreement was obtained with the van der Pauw measurement of n_B, especially considering the facts that (1) the van der Pauw measurement was performed on a wafer slice from the HgCdTe ingot adjacent to the slice used for MIS device fabrication, and (2) the MIS measurement is characteristic of the surface region only to a depth of 1.0 μm.

The two sets of curves, Figure 14 and 15 and Figure 16 and 17, are nearly pairwise identical except for the frequency label on each curve. If we superpose Figures 14 and 15, identical C vs. V_g with f as a parameter curves are obtained at the corresponding frequencies shown in Figure 18 for the two background irradiances, $\phi_B = 2 \times 10^{12}$ cm^{-2} sec^{-1} and $\phi_B = 10^{13}$ cm^{-2} sec^{-1}. At 1 MHz, the C vs. V_g curves are nearly identical at both photon irradiances. Linear extrapolation of the corresponding frequencies curve to high

---

[25]A. F. Tasch, Jr., D. D. Buss, R. T. Bate, and B. H. Breazeale, Proc. Tenth Int. Conf. on the Phys. of Semicond., ed. S. P. Keller, J. C. Hensel, and F. Stern, (USAEC Div. of Tech. Inf., Oak Ridge, Tenn., 1970) p 458

[26]W. W. Anderson, Infrared Phys. 17, 147 (1977)

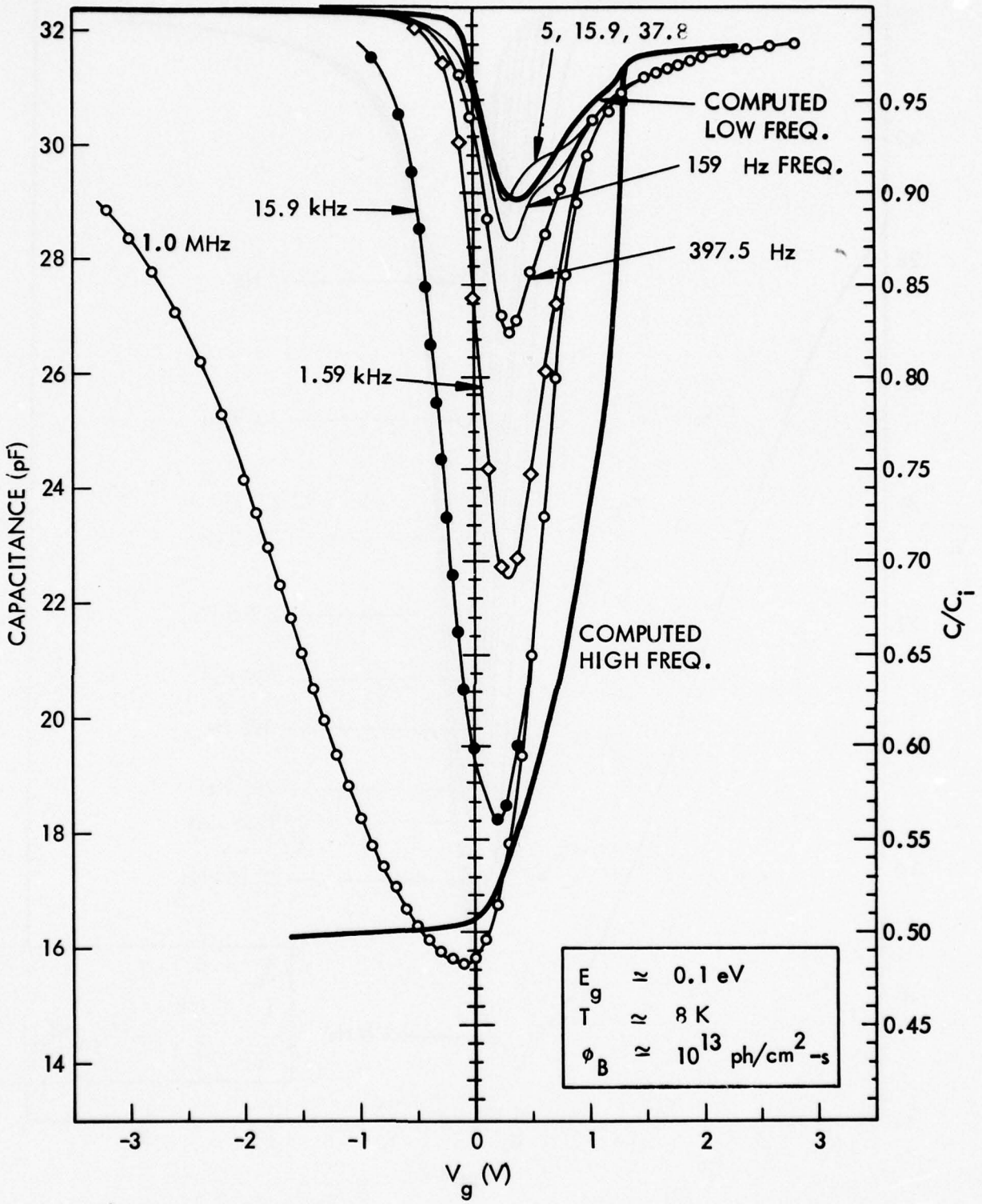

Figure 14. Capacitance-voltage characteristic of LWIR MIS device with signal frequency as a parameter. Sample before γ-irradiation in background photon irradiance of $\phi_B = 10^{13}$ cm^{-2} sec^{-1}

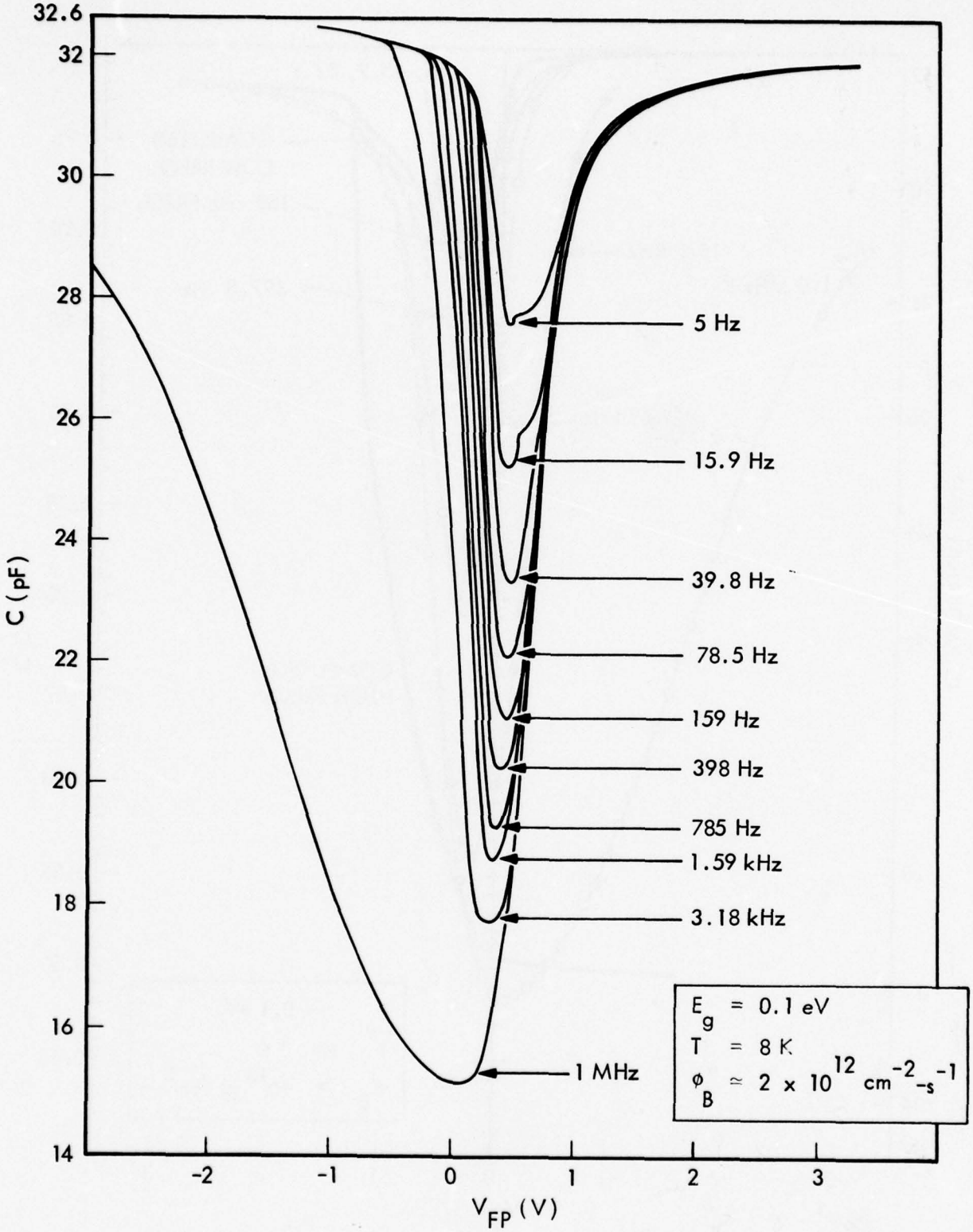

Figure 15. Capacitance-voltage characteristic of LWIR MIS device with signal frequency as a parameter. Sample before γ-irradiation in background photon irradiance of $\phi_B = 2 \times 10^{12}$ cm^{-2} sec^{-1}

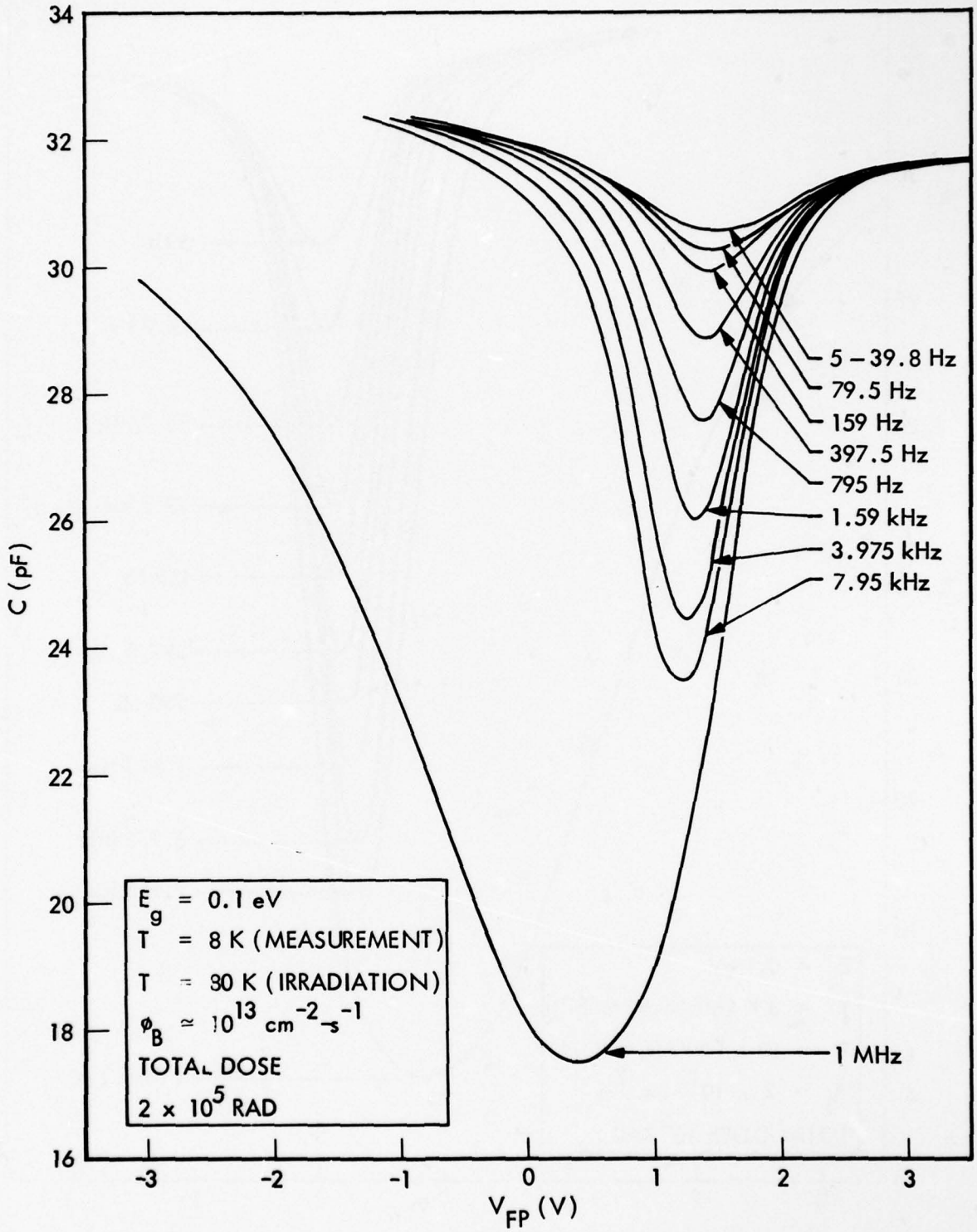

Figure 16. Capacitance-voltage characteristic of LWIR MIS device with signal frequency as a parameter. Sample following 200 kR γ-irradiation and in a background photon irradiance of $\phi_B = 10^{13}$ cm^{-2} sec^{-1}

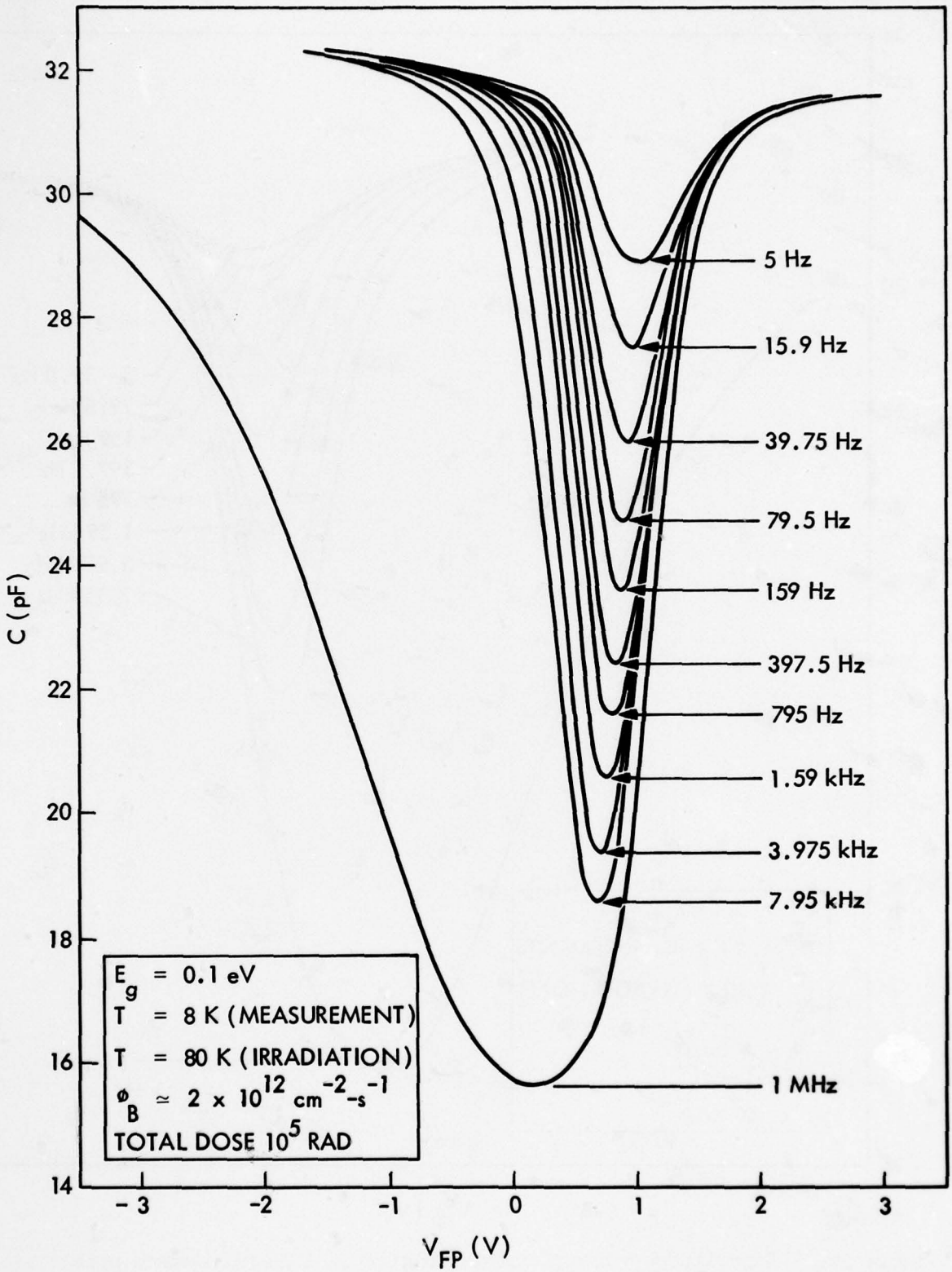

Figure 17. Capacitance-voltage characteristic of LWIR MIS device with signal frequency as a parameter. Sample following 100 kR γ-irradiation and in a background photon irradiance of $\phi_B = 2 \times 10^{12}$ cm^{-2} sec^{-1}

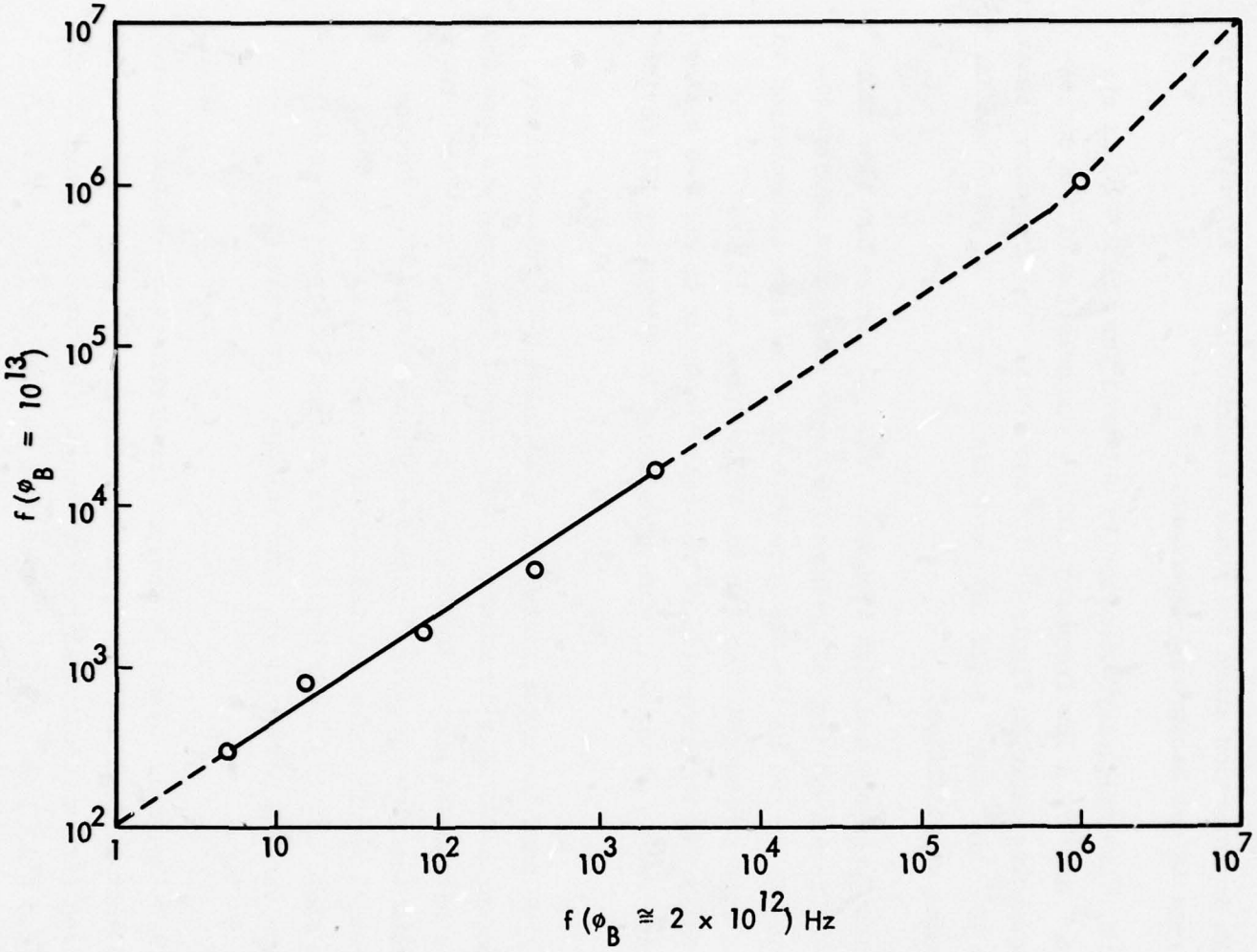

Figure 18. Frequencies at which C vs. V_g curves at $\phi_B = 10^{13}$ cm^{-2} sec^{-1} are identical to C vs. V_g curves at $\phi_B = 2 \times 10^{12}$ cm^{-2} sec^{-1}. Dotted lines are assumed interpolation and extrapolations beyond measured points

frequencies indicates that the two sets of C vs. V_g curves should merge at 700 kHz. We expect the C vs. V_g curves to be independent of background above 700 kHz in inversion since the tunnel contribution to minority carrier generation rate is not background dependent.

In Figure 14, "low frequency" behavior is observed for all $f \leq 80$ Hz at $\phi_B = 10^{13}$ cm^{-2} sec^{-1}. A low frequency linear extrapolation of the corresponding frequencies curve in Figure 18 indicates that "low frequency" behavior at $\phi_B = 2 \times 10^{12}$ cm^{-2} sec^{-1} would not occur until $f \approx 0.7$ Hz which was far below our measurement capabilities.

Calculated low frequency and high frequency C vs. V_g curves are also shown on Figure 14. The abrupt drop of the high frequency calculated C below the 1 MHz experimental curve as the MIS gate voltage moves from accumulation to depletion is more pronounced than for the SWIR device in Figures 7 - 9. This is probably due to connection of the bulk electrons to surface states via the tunnel mechanism which is more pronounced in narrow gap MIS devices [26].

In Figure 19 we show the experimental and calculated C-V_g characteristic before and after a 200 kR γ-irradiation. The signal frequency was less than 80 Hz with a background photon irradiance of $\phi_B = 10^{13}$ cm^{-2} sec^{-1} so that we were well into the "low frequency" regime of Figures 14 and 16. Surface state parameters required for the calculated curves are given in Table 2. The surface state density distributions are plotted in Figure 20 and the corresponding surface potential vs. gate voltage curves are given in Figure 21.

In Figure 19, the small "bump" in the pre irradiation C-V_g measured curve at $V_g = 0.5$ volt is real and also appears in Figures 14 and 15. This effect can be modeled with an additional peak in the $N_{ss}(E)$ curve of Figure 20 of $\Delta N_{ss}(E_s) = 2.3 \times 10^{11}$ cm^{-2} eV^{-1} centered at $E_s = -.05$ eV ($E_s = -E_g/2$). When the device was annealed at room temperature following the first

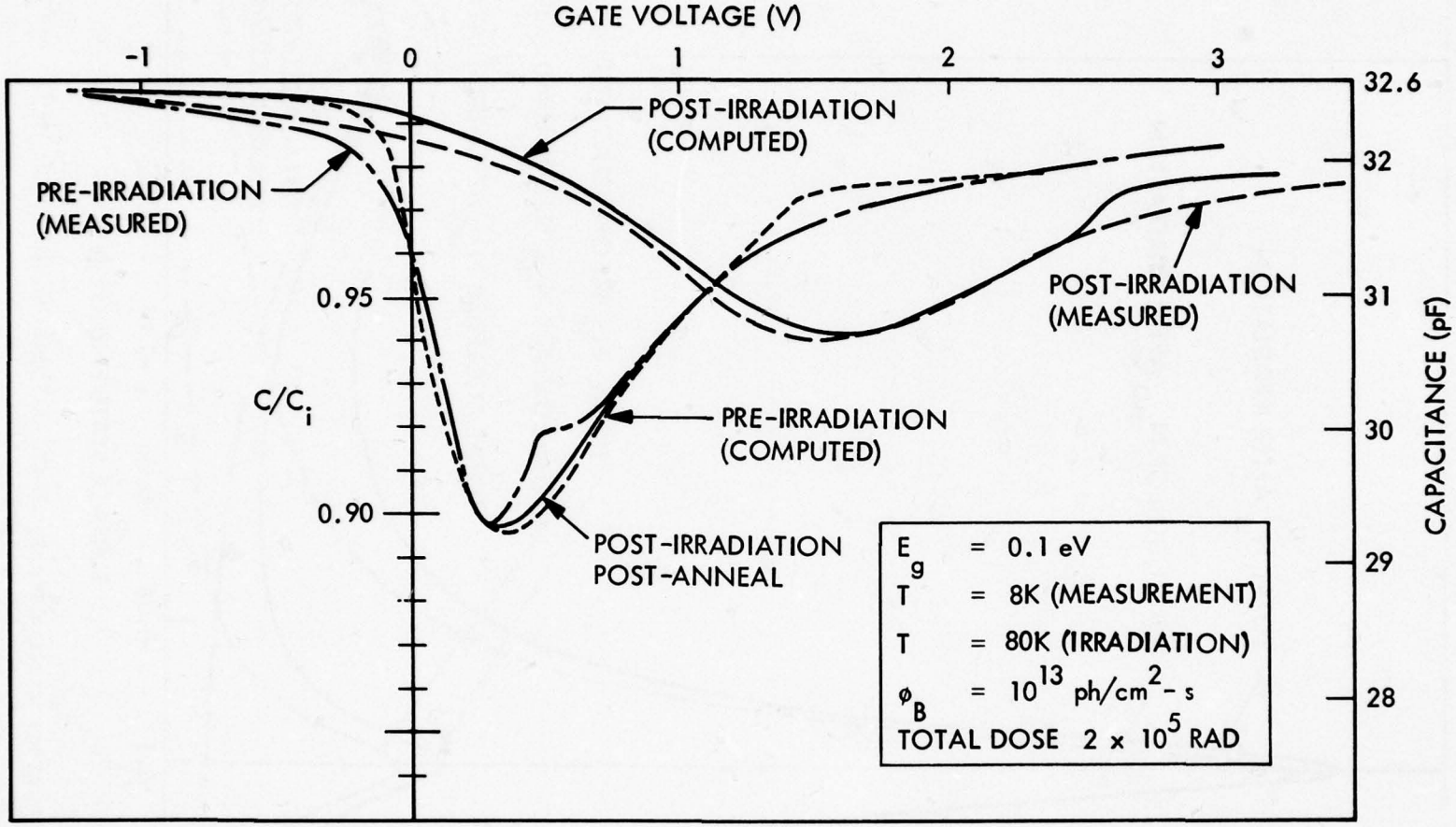

Figure 19. Low frequency capacitance-voltage characteristic of LWIR MIS device before and after 200 kR γ-irradiation

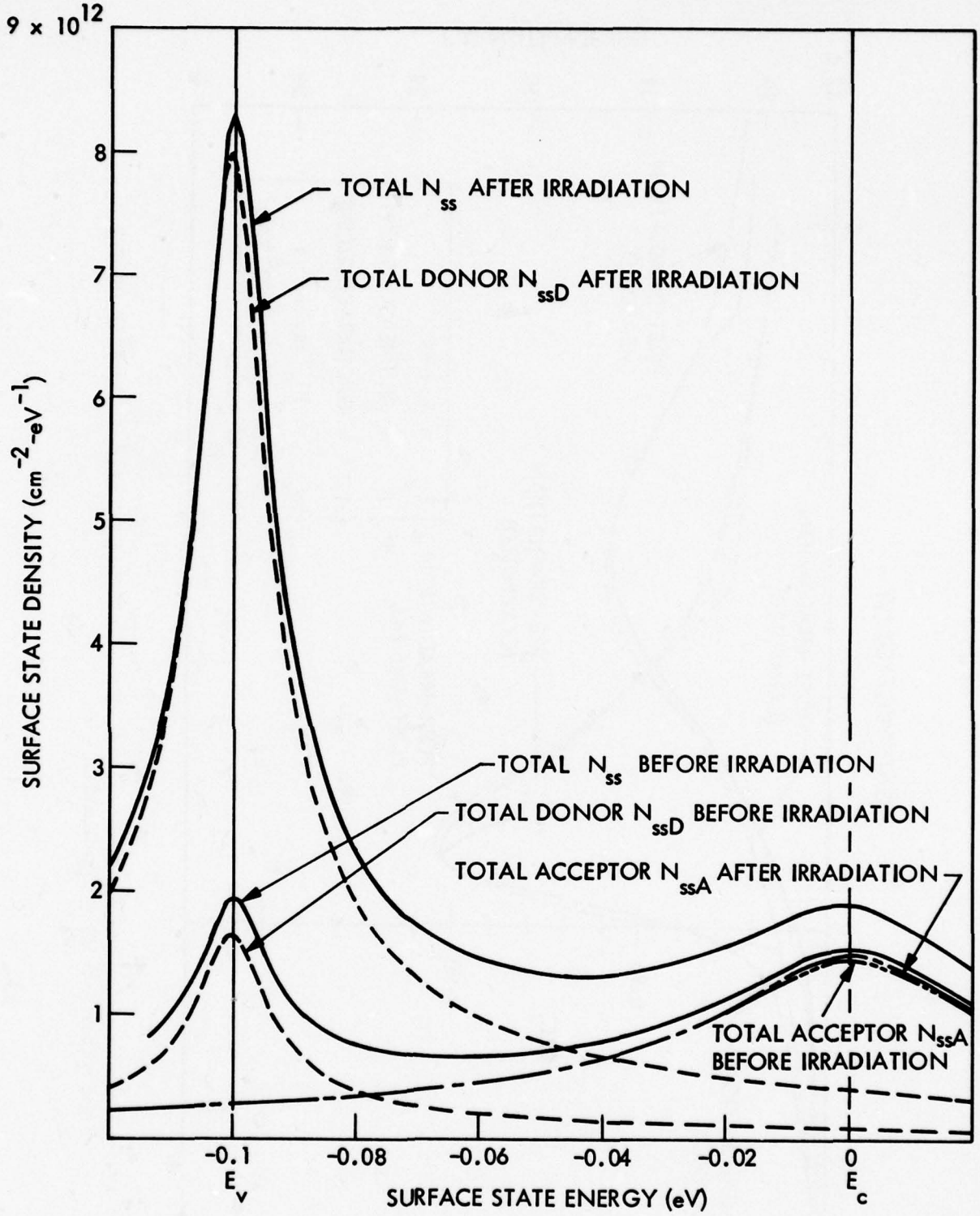

Figure 20. Surface state density distributions of LWIR MIS device before and after 200 kR γ-irradiation

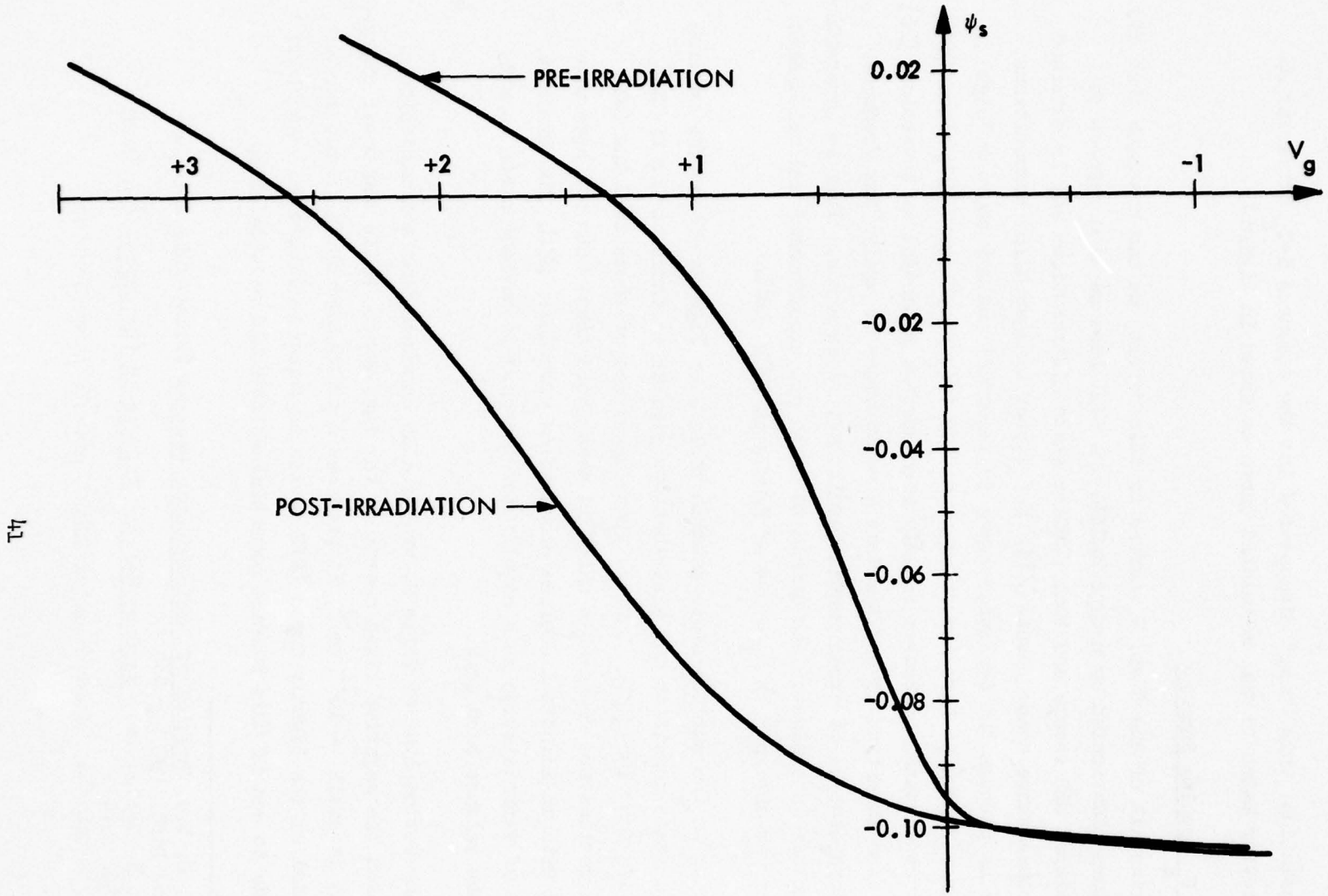

Figure 21. Surface potential as a function of gate voltage of LWIR MIS device before and after 200 kR γ-irradiation

γ-irradiation, this "bump" disappeared and the measured C-V_g curve was an even better match to the calculated curve as shown in Figure 19.

C vs. V_g Results Summary

Reviewing all of the C vs. V_g curves in this report, we can conclude that MIS structures fabricated on n-type HgCdTe are well behaved with respect to established MIS theory and that surface state distributions may be obtained from capacitance measurements [27]. For narrow bandgap alloy compositions, tunneling through the depletion layer is important and may cause a "high frequency" curve to have the shape of a "low frequency" curve [25] since the tunnel conductance increases rapidly with surface potential in inversion [26]. It is also important to confirm that a measurement is truly "low frequency" or interpretation of experimental results may be in error. This is apparently why another investigator was unable to match his experimental and calculated C-V_g curves obtained on E_g = 0.4 eV HgCdTe at 77°K [28].

Returning to the surface state data in Table 2 or Figures 12 and 20, we find surface state densities and distributions similar to those at the Si-SiO_2 interface circa 1967 [27]. Surface state densities of these SWIR and LWIR HgCdTe devices are comparable which is reasonable since both had been processed with an identical surface preparation procedure [29]. The dominant effect of γ-irradiation is a significant increase of surface state density near the valence band edge.

From the bottom line of Table 2, we may also conclude that γ-irradiation increases the negative fixed charge in the insulator. While the total charge density is small, $\sim 10^{11}$ cm^{-2}, it produces a pronounced shift in the surface potential of the lightly doped LWIR device as shown in Figure 19. An attempt was made to see if this surface potential shift could be altered by

---

[27] S. M. Sze, Physics of Semiconductor Devices (Wiley-Interscience, New York, 1969) p 444

[28] A. A. Pellegrino, Surface Related Effects in (Hg,Cd)Te, (MS Thesis, MIT, 1974)

[29] R. Rotolante, Carson-Alexiou Corp., private communication

electrically stressing the insulator during γ-irradiation. Accordingly, irradiations were carried out with the gate electrode connected as indicated in Table 3. In every case, the post irradiation C vs. V_g curves were unaffected by the gate electrode connection or potential during irradiation.

TABLE 3.

GATE ELECTRODE CONNECTIONS DURING γ-IRRADIATIONS

DETECTOR	DOSE	V_g
SWIR	2×10^5 R	Open
SWIR	2×10^5 R	Shorted
LWIR	2×10^5 R	Open
LWIR	2.4×10^5 R	-1 Volt
LWIR	1×10^5 R	+2 Volt
LWIR	1×10^5 R	Open
LWIR	1×10^5 R	Shorted

DETECTOR PROPERTIES

Introduction

In this subsection we present data on responsivity, noise spectral density and photoconductive lifetime obtained on 0.3 eV and 0.1 eV energy gap trapping mode HgCdTe detectors. Before presenting these data we briefly review a few basic relations pertinent to photoconductive detectors. The voltage responsivity R_V is

$$R_V = \eta \frac{\mu_n \mathscr{E} R_D}{\ell(h\nu/e)} \frac{\tau}{\left(1 + \omega^2\tau^2\right)^{\frac{1}{2}}} \quad \text{V/W} \qquad (8)$$

where

η is the quantum efficiency

μ_n is the mobility of the majority carriers (electrons in this case)

$\mathscr{E}$ is the electric field across the detector

τ is the majority carrier lifetime

ℓ is the interelectrode spacing

$h\nu/e$ is the energy of the (monochromatic) signal radiation

ω is the angular frequency of the signal radiation

At very low frequencies R_V is proportional to τ and independent of frequency while at high frequencies R_V is proportional to ω^{-1}. It should be pointed out, however, that the frequency dependence of trapping mode detectors cannot in general be described in terms of a single time constant. The observed frequency dependence of responsivity does not follow ω^{-1} at high frequencies. Instead the high frequency response more closely resembles an $\omega^{-\frac{1}{2}}$ relation. This behavior is due to the presence of, not one, but a spectrum of time constants. Thus, it is not possible to simply extract "the time constant" from the 3db point of the responsivity vs. frequency curve. A graphical technique to extract the dominant time constant will be described later.

The principal detector noise sources are generation-recombination noise, $V_{g\text{-}r}$ (either thermally or optically induced), excess noise, V_{ex} and

Johnson-Nyquist noise V_J.

The generation-recombination noise is given by

$$V_{g-r} = 2e\,\mu_n R_D \left(\frac{w}{\ell}\right)^{\frac{1}{2}} \mathcal{E}(\eta\phi_B + g_{th}d)^{\frac{1}{2}} \frac{\tau}{\left(1+\omega^2\tau^2\right)^{\frac{1}{2}}} \quad V/\sqrt{Hz} \qquad (9)$$

where

w	is width of the detector
ϕ_B	is the optical background flux density
g_{th}	is the thermal generation rate of carriers
d	is the device thickness

The other symbols have the meaning previously defined. At the temperatures used in these experiments ($\leq 80°K$) we do not expect to see the thermal generation term. We can then write the optical portion of V_{g-r} in the more useful form

$$V_{g-r} = 2\,h\nu\,A_D^{\frac{1}{2}} \left(\frac{\phi_B}{\eta}\right)^{\frac{1}{2}} R_V \quad V/\sqrt{Hz} \qquad (10)$$

where A_D is the detector area and the other symbols were defined earlier. Since both R_V and V_{g-r} have the same frequency dependence we can use Eq. (10) in conjunction with the measured values of R_V to estimate V_{g-r}, and its frequency dependence.

The excess noise spectral density follows the semi-empirical relation

$$V_{ex} = \frac{K\mathcal{E}}{f^{\frac{1}{2}}} \quad V/\sqrt{Hz}$$

where K is a constant. This noise source is generally believed to be the result of fluctuations in charge carrier density caused by recombination states located at the detector surface or at the contacts. Previous experiments suggest that in trapping HgCdTe detectors the surface dominates. This noise source is independent of background flux density.

The Johnson-Nyquist noise is independent of frequency and optical background (as long as the background does not change the carrier density significantly) and is given by

$$V_J = (4k\, T_D\, R_D)^{\frac{1}{2}} \qquad V/\sqrt{Hz}$$

where k is Boltzmann's constant and T_D is the detector temperature. This noise source is negligible in these detectors.

Preamplifier noise in these experiments was about 10^{-9} $V/\sqrt{Hz}$ at high frequencies and did not impact our results.

In Table 4 we list some important detector parameters.

TABLE 4

	Detector (both compositions)		
	AB	de or ef	
Interelectrode Spacing	8.1×10^{-2}	2.5×10^{-2}	cm
Width	2.65×10^{-2}	2.65×10^{-2}	cm
Area	2×10^{-3}	6.7×10^{-4}	cm^2
Thickness	$\sim 2 \times 10^{-3}$	$\sim 2 \times 10^{-3}$	cm
	0.1 eV gap	0.3 eV gap	
Operating Temperature	8°K	80°K	
Bias Field	1.2	4.8	v/cm
Majority Carrier Density	1.7×10^{14}	2×10^{16}	cm^{-3}
Wavelength of Radiation	3.5	3.5	μm

Results on 0.3 eV Engergy Gap Detectors

The frequency dependence of responsivity of detectors AB, de and ef are shown in Figures 22 and 23. The data was obtained at a background of about 10^{13} ph-cm^{-2} s^{-1} at 80°K. All three detectors behave qualitatively

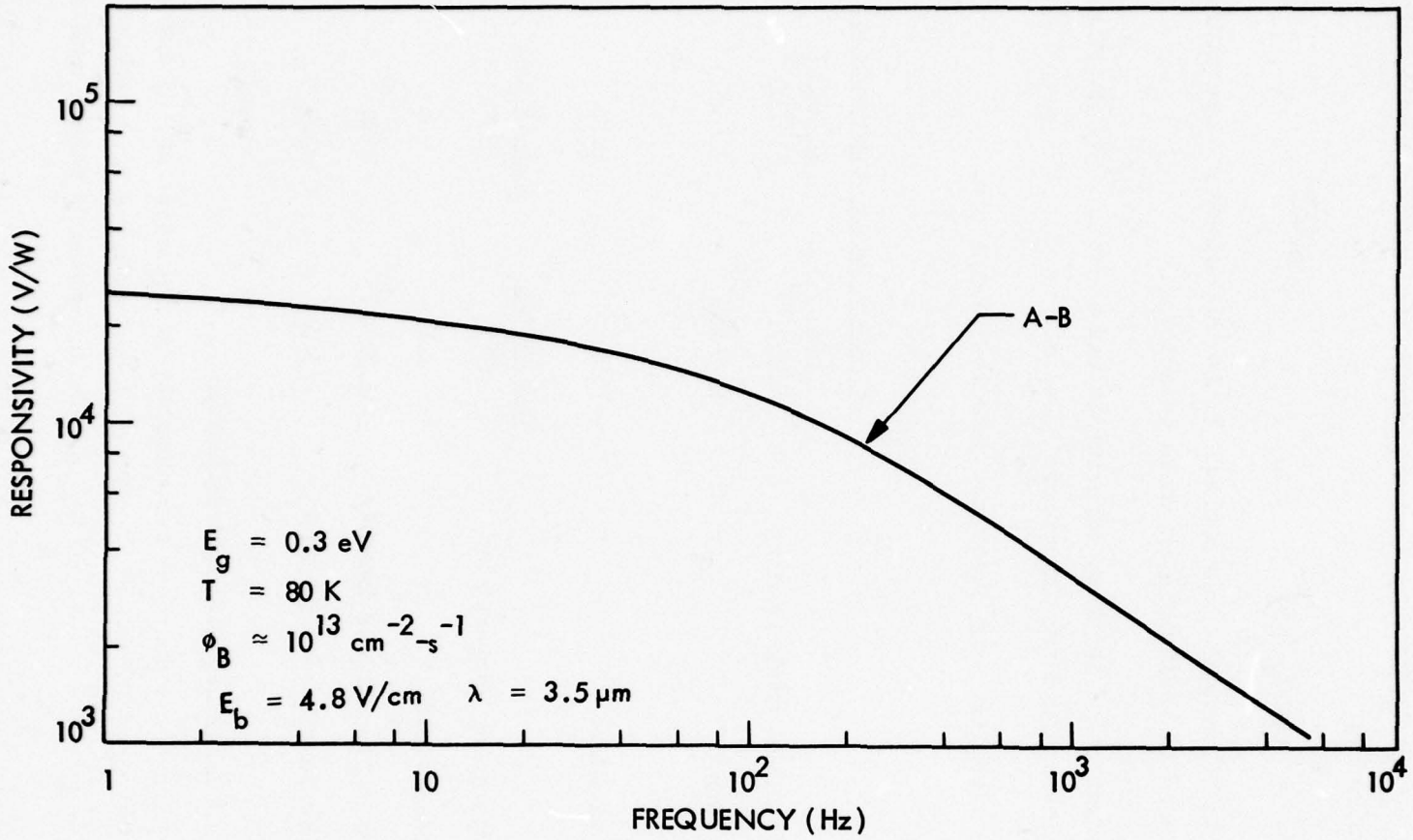

Figure 22. Frequency dependence of responsivity of 0.3 eV MIS detector

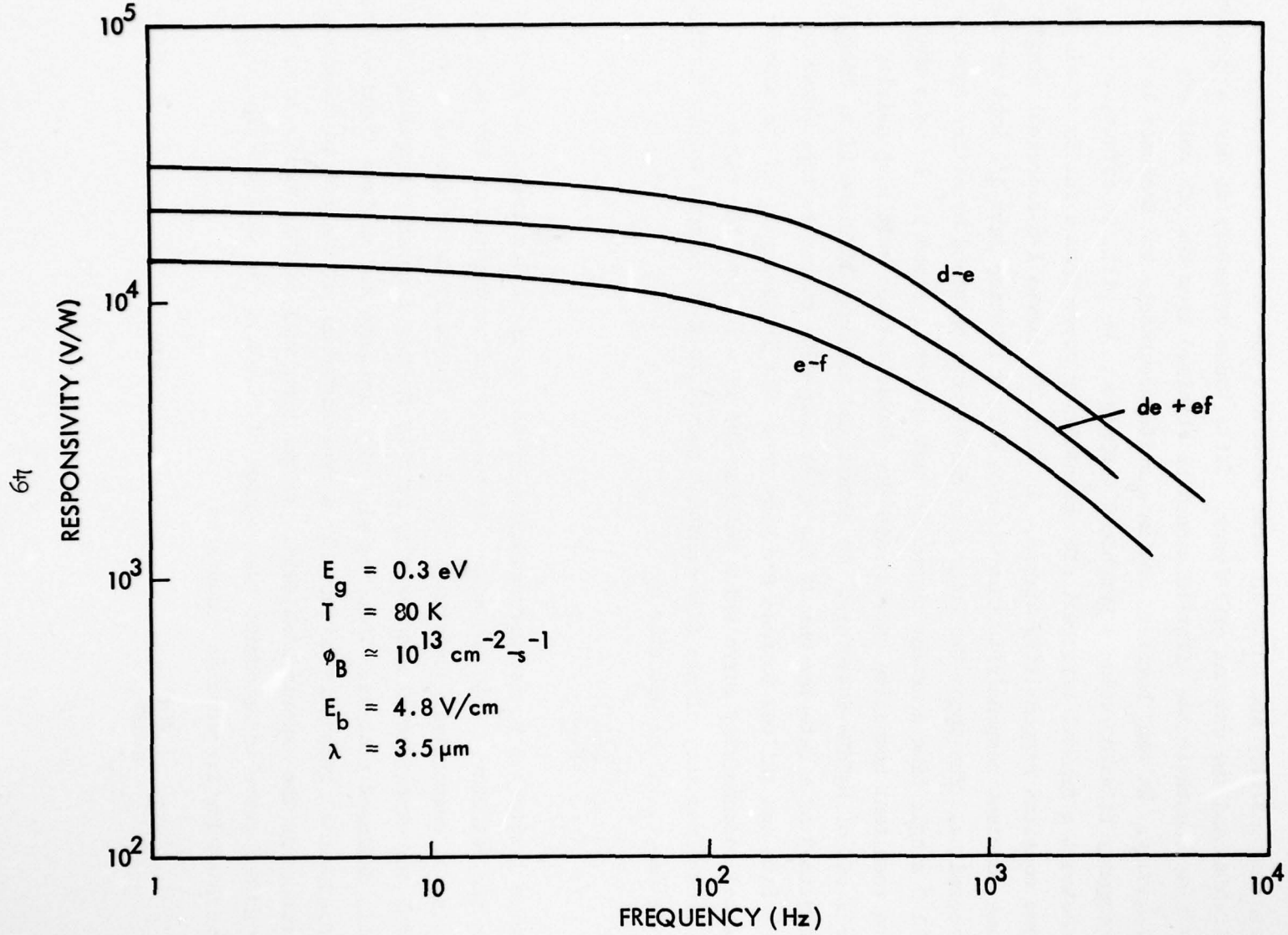

Figure 23. Frequency dependence of responsivity for bare (ef) and Zns coated (de) detectors

alike and have soft roll offs. In order to obtain a consistent picture of both responsivity and noise in these detectors one must determine their lifetime and the quantum efficiency. Since these detectors do have a spectrum of time constants the lifetime cannot be obtained from the 3db roll off frequency. We can, however, estimate quite accurately the dominant low frequency lifetime using a graphical technique. We will, in effect, reconstruct a typical soft roll off responsivity curve from a family of single time constant responsivity curves. In Fig. 24 curves 1-6 represent single time constant responsivity curves, each with a lifetime just 1/2 that of the preceeding. The upper two composite curves were obtained by either summing all 6 single time constant curves or just curves 1, 3, and 5. We note that the resultant composite curves have the characteristic soft responsivity roll off of HgCdTe detectors. To obtain the dominant lifetime (i.e. longest lifetime) of a detector one of the upper composite curves is superposed on the data and shifted to make the best fit. The frequency f_D on the experimental responsivity curve which matches the $\omega\tau = 1$ point for curve 1 (lowest frequency single time-constant curve) is then related to the dominant lifetime τ_D in the detector by

$$\tau_D = \frac{1}{2\pi f_D}$$

Curve 1 with $\tau = \tau_D$ is representative of the dominant low frequency process in the detector. With the composite curve still superposed on the data the value of responsivity determined by the low frequency intercept of curve 1 with the experimental responsivity axis is the low frequency responsivity of this dominant process. Thus, curve 1 with ordinate and abcissa fixed by the experimental responsivity curve is a representation of the lowest frequency process in the experimental data. We can then analyze this single time constant curve to determine the quantum efficiency. We will use Eq. (8), which at low frequencies reduces to

$$R_V = \frac{\eta \mathcal{E} \tau}{h\nu n w t} \qquad V/W \qquad (11)$$

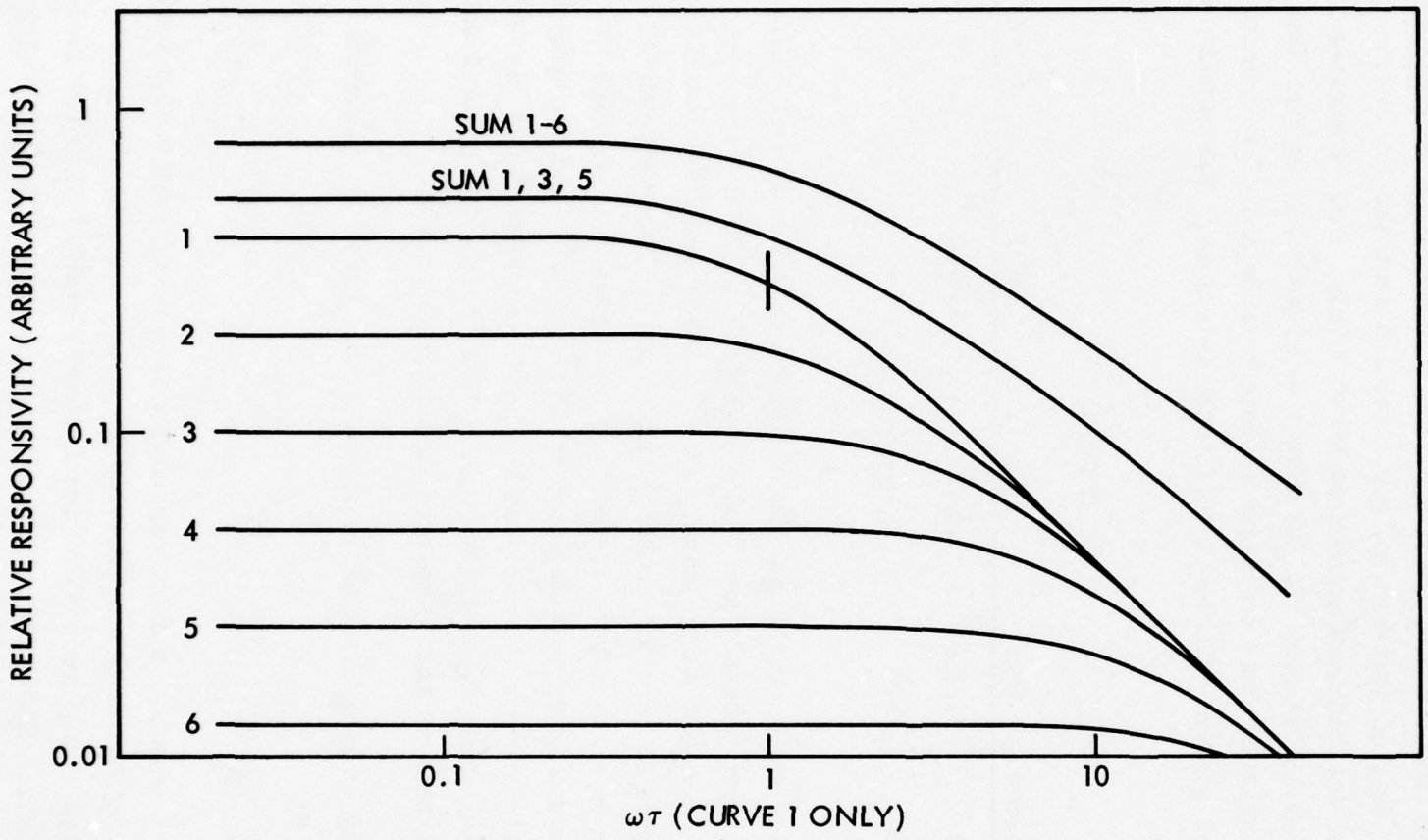

Figure 24. Composition of soft roll-off responsivity curves

and the data from Table 4. Then applying this technique to Detector AB, Figure 22, we find that $\tau_D = 3.5 \times 10^{-3}$ sec and that the low frequency responsivity of the dominant process is about 1.7×10^4 V/W. Comparing this to the value calculated from Eq. (11) with $\tau = 3.5 \times 10^{-3}$ sec we find that $\eta \simeq 0.06$. Applying this technique to detectors de and ef we determine the lifetime and quantum efficiencies of these detectors. The results are given in Table 5.

TABLE 5

Detector	AB	de	ef	de + ef
τ	3.5×10^{-3}	1.6×10^{-3}	1.6×10^{-3}	1.6×10^{-3}
η	.06	.17	.07	.12

The noise for detectors AB and the series combination de + ef (i.e. the noise measured between points d and f of Figure 2) is given in Figure 25. The noise voltage varies approximately as $f^{-\frac{1}{2}}$, and appears to be excess noise. Also on Figure 25 are the computed values of V_{g-r} for detector AB and the combination de + ef. These curves were calculated from Eq.(10) using measured values of R_V, a background of 10^{13} cm^{-2} s^{-1}, and the computed quantum efficiencies. We see that for both detectors AB and de + ef, the expected generation recombination noise falls below the measured noise. We conclude that in both detectors this is excess noise.

The majority carrier lifetime in trapping mode HgCdTe is background dependent and varies as

$$\tau = K\phi_B^{-\alpha}$$

where K is a constant and the exponent α is generally between 0.5 and 0.8. Since the low frequency responsivity is proportional to the lifetime, we can obtain α from a log-log plot of low frequency responsivity (or signal level) vs. background. This plot can then be normalized to the low background time

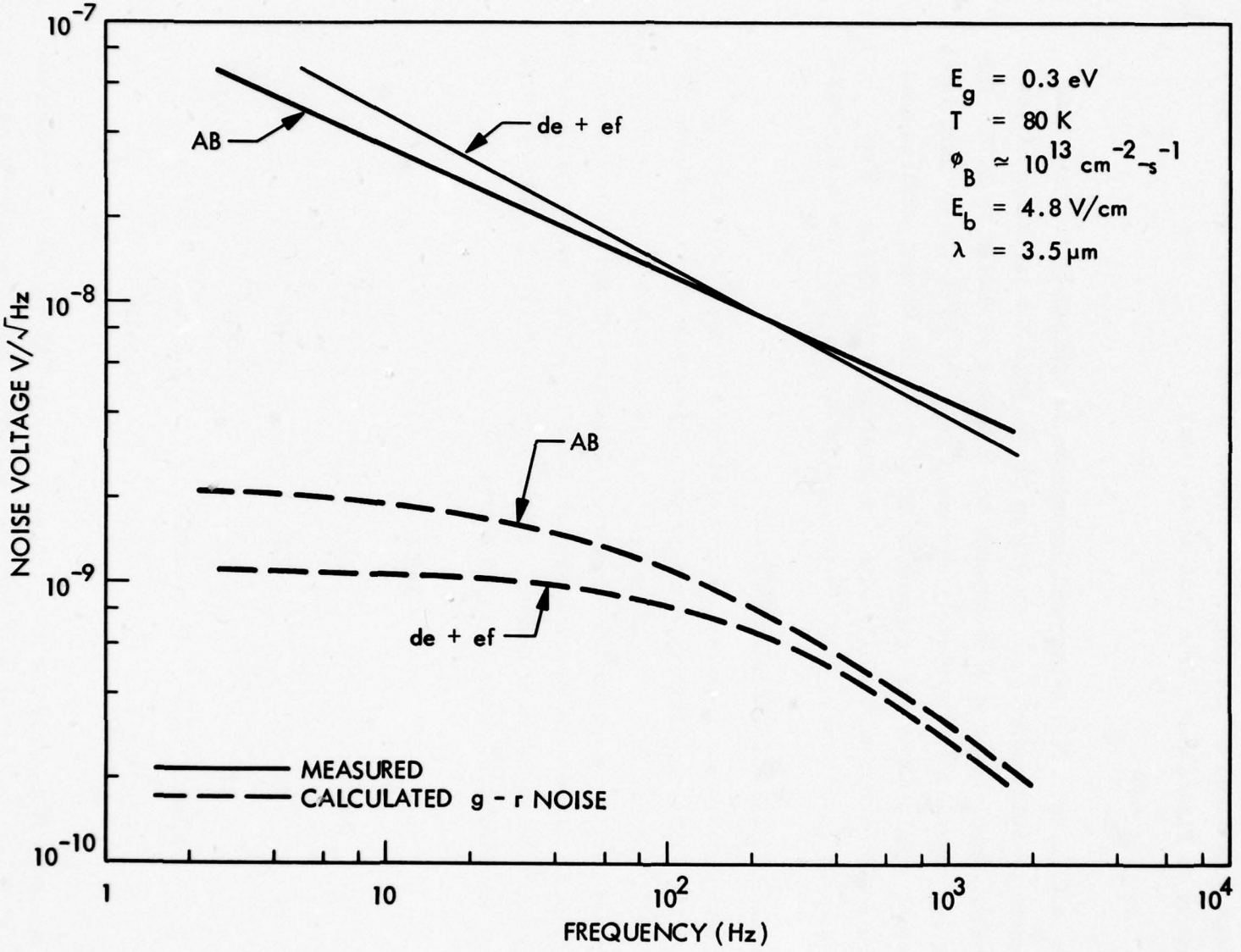

Figure 25. Measured and computed noise on 0.3 eV detectors

constant determined by the graphical method. These data for detector AB are shown in Figure 26. From this we see that

$$\tau \sim \phi_B^{-.72}$$

For V_g = 0 volts. This background dependence is typical of trapping mode detectors of this energy gap. In Figure 27 we show the variation of low frequency signal level with background for detector AB cooled to 10°K. The power law dependence is virtually unchanged from its 80°K value. This is an important result since the trapping model of Beck and Broudy predicts that α should increase monatonically with a decrease in temperature. Thus, these data are not reconcilable with the predictions of the Beck and Broudy model.

Results on 0.1 eV Engergy Gap Detectors

The responsivity vs. frequency for detectors AB, de and ef are shown in Figure 28. The responsivity for detector AB is shown at two backgrounds $\phi_B \simeq 2 \times 10^{12}$ and $\phi_B \simeq 10^{13}$ ph cm^{-2} s^{-1}. From this data using the procedure discussed earlier we extracted the dominant lifetime and detector quantum efficiency. These results are listed in Table 6. The longer time constant of detector AB is probably a result of the lower effective background on AB due to the presence of the Au field plate.

TABLE 6.

Detector	η	τ (s)
de	0.2	1.2×10^{-3}
ef	0.06	1.2×10^{-3}
AB(2×10^{12} ϕ_B)	0.02	3.2×10^{-3}
AB(10^{13} ϕ_B)	0.02	1.5×10^{-3}

The noise vs. frequency for AB is shown in Figures 29 and 30 for backgrounds of 2×10^{12} and 1.3×10^{13} ph cm^{-2} s^{-1} respectively. The noise depends on

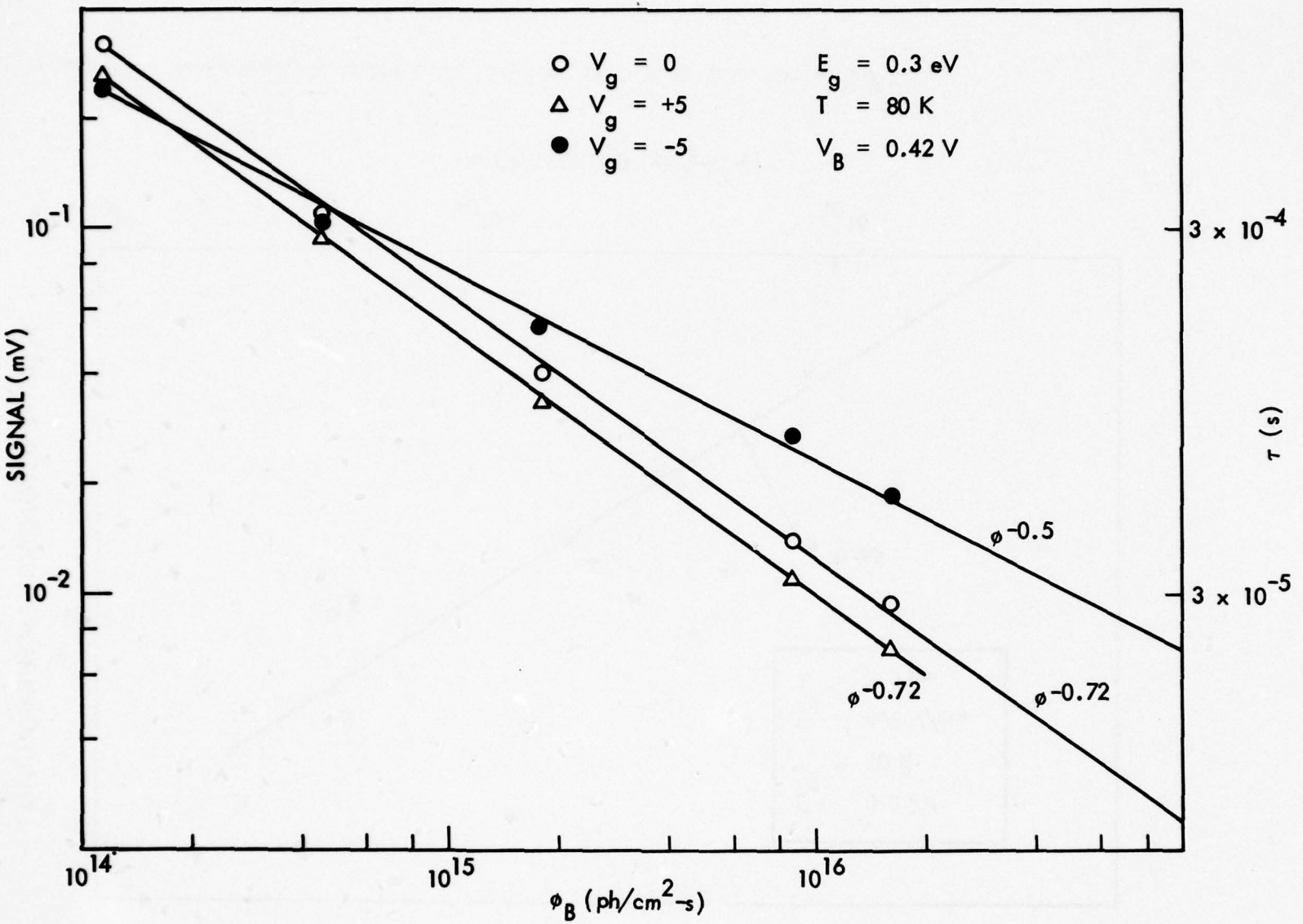

Figure 26. Background dependence of lifetime in 0.3 eV detector at 80° K.

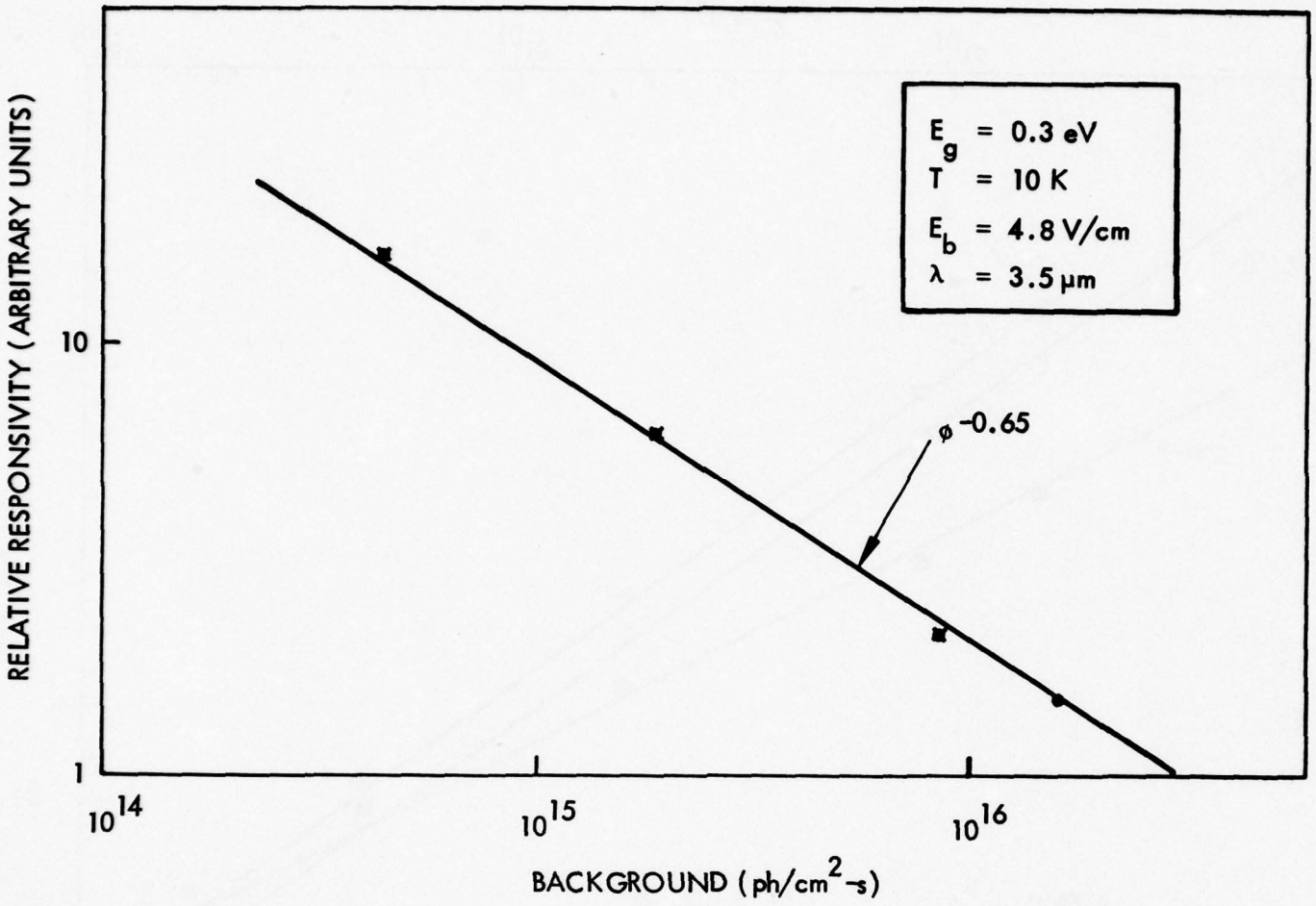

Figure 27. Background dependence of lifetime in 0.3 eV detector at 10° K

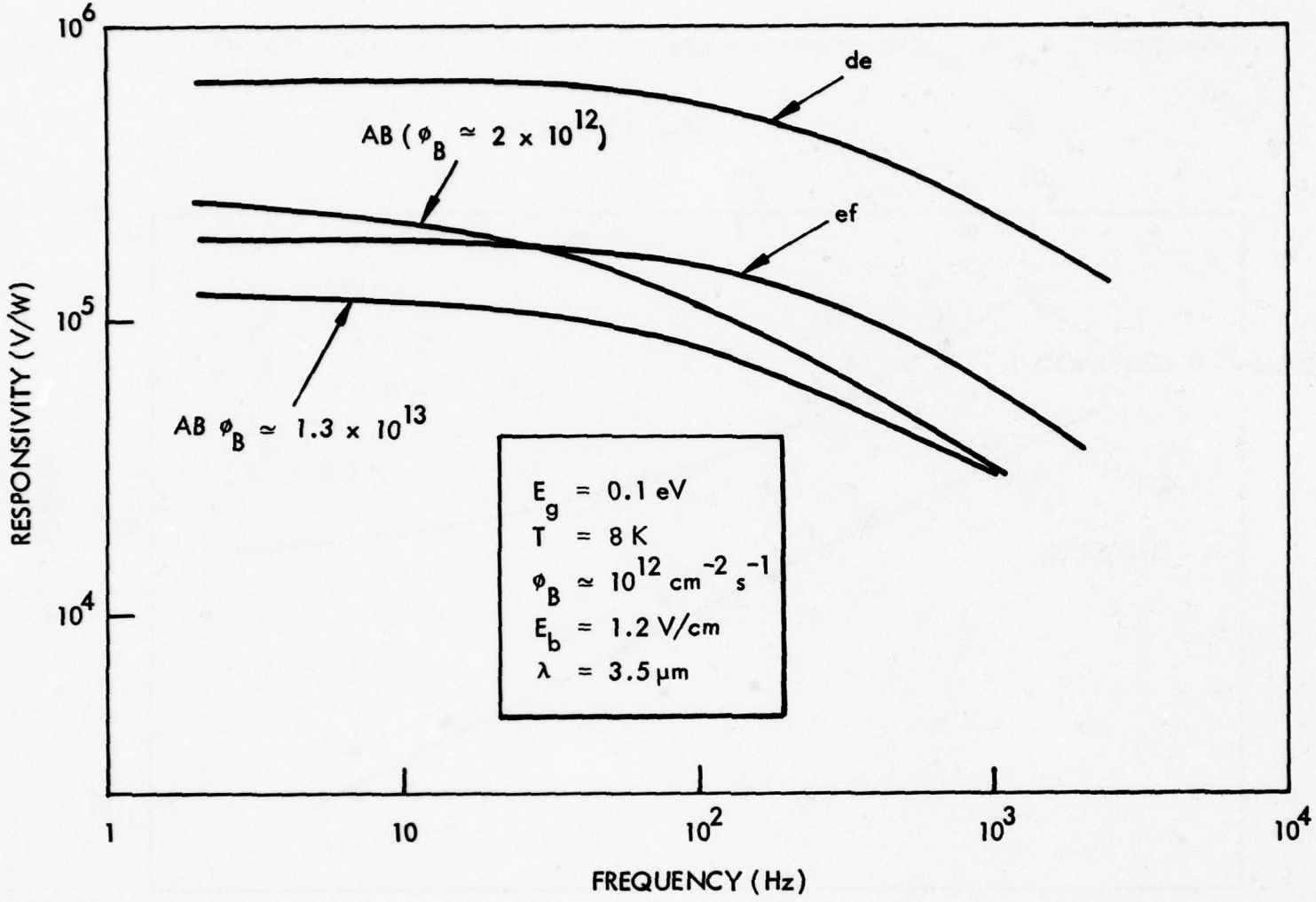

Figure 28. Frequency dependence of responsivity of 0.1 eV detectors

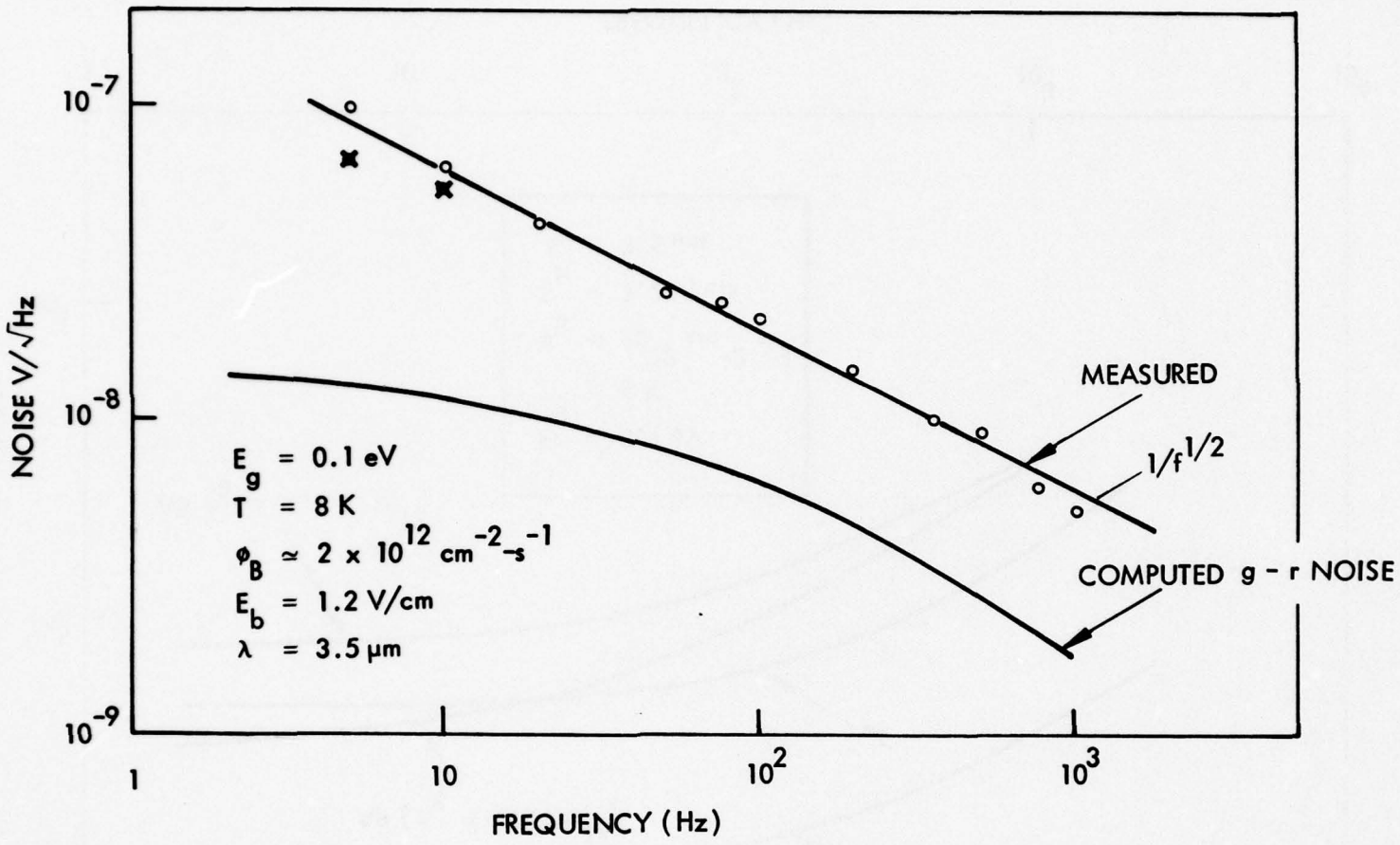

Figure 29. Measured and calculated noise on 0.1 eV MIS detector at 2×10^{12} cm^{-2} s^{-1} background

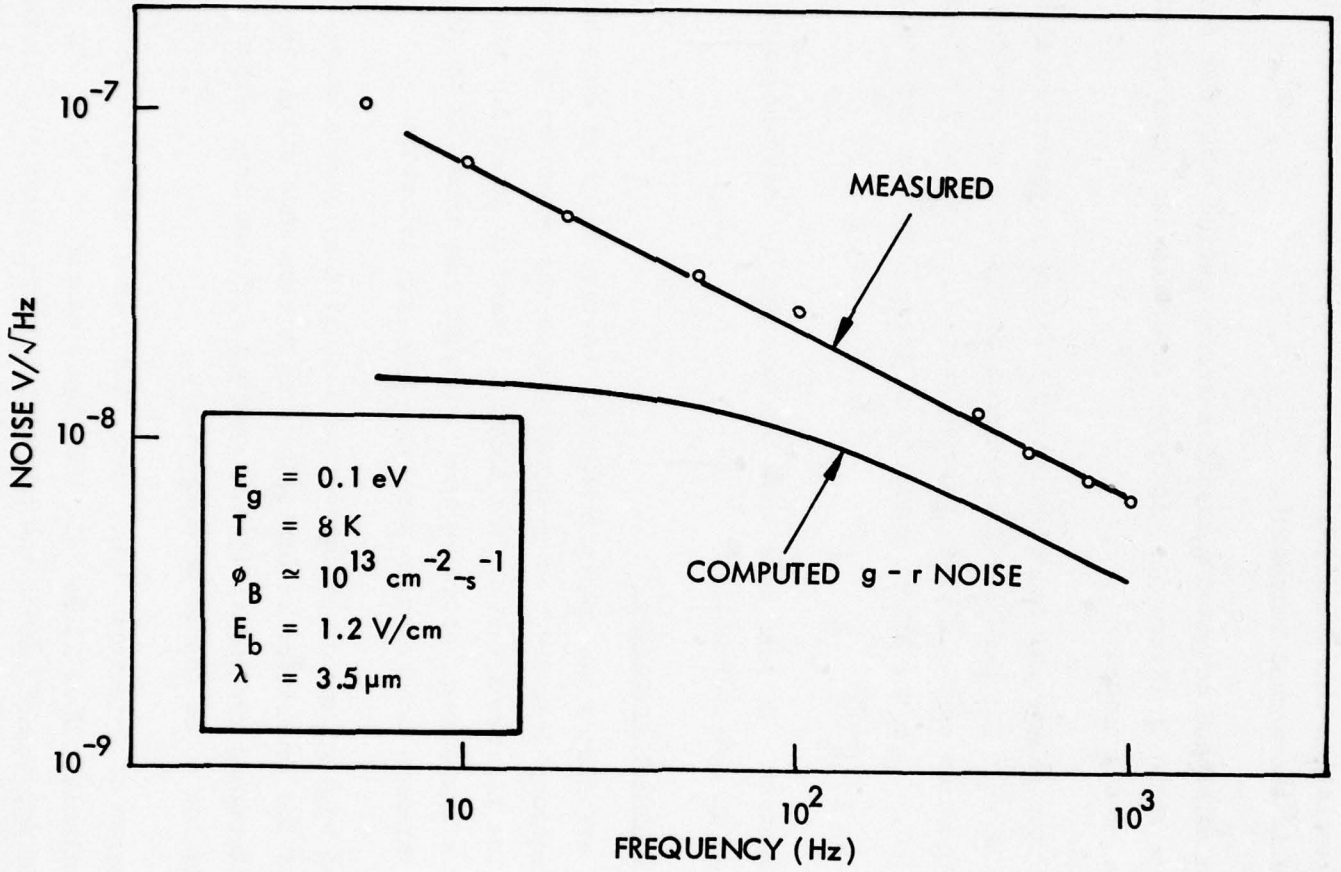

Figure 30. Measured and calculated noise on 0.1 eV MIS detector at 10^{13} cm^{-2} s^{-1} background

frequency as $f^{-\frac{1}{2}}$ and is independent of background, as one would expect for excess noise. The generation recombination noise was computed, as described earlier, and also shown on Figure 29. It is well below the measured noise value. Comparing the measured noise to the computed V_{g-r} at $\phi_B \simeq 10^{13} cm^2\ s^{-1}$ we conclude that the measured noise may at high frequencies be a combination of excess and generation-recombination noise. However, the major contribution to the noise is the excess component.

The measured noise and computed generation-recombination noise for detectors de and ef are shown in Figure 31. Again we note that the measured noise is primarily an excess noise.

In Figure 32 the background dependencies of lifetime in detectors AB and de + ef are shown. The background dependence of lifetime in detector AB is shown as a function of field plate voltage from -0.5 V to +3.0 V (reading from top to bottom). From the linear portions of these curves we determine that

$$\tau = K' \phi_B^{-0.55}$$

for both detectors. We also note that the exponent is independent of field plate voltage in detector AB.

Summary of Detector Properties

The quantum efficiency and dominant majority carrier lifetime were determined from the frequency dependence of responsivity on the detectors of each composition. The lifetimes varied from about 1.5 msec to about 3.5 msec, while the quantum efficiencies varied an order of magnitude from .02 to .2 with the widest variance occurring in the lower band gap detectors.

The noise of both groups of detectors was dominated by excess noise. Estimates of the generation recombination noise were made using the experimentally determined responsivities and quantum efficiencies. This noise was sufficiently low so as not to be observable.

The three types of detectors, i.e., bare, ZnS coated, and MIS devices, all behaved similarly. Thus it is felt that the presence of ZnS or ZnS and field plate do not appreciably alter the properties of the detector. Therefore the information obtained on the MIS device should be applicable on HgCdTe detectors in general.

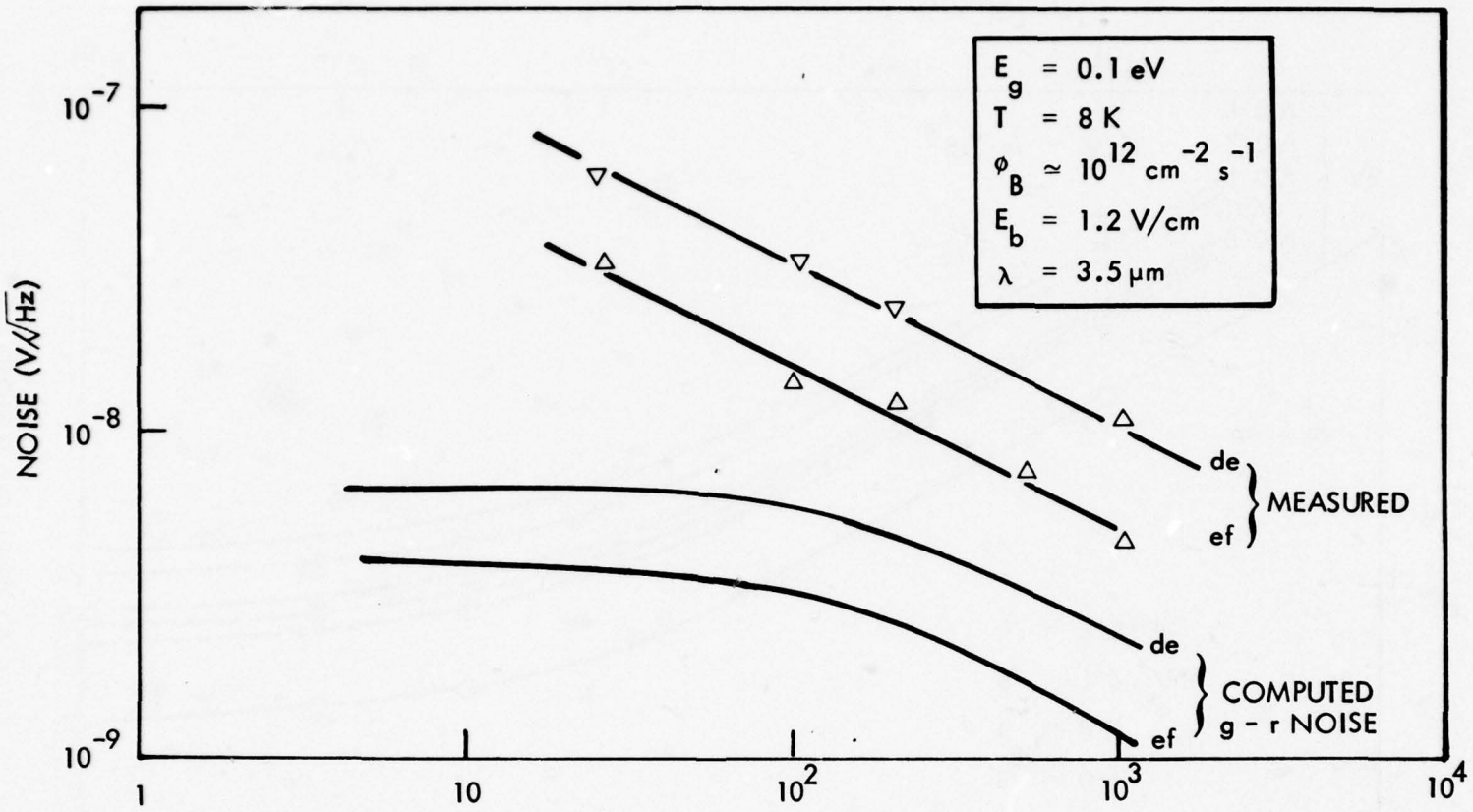

Figure 31. Measured and calculated noise on 0.1 eV bare (ef) and ZnS coated (de) detectors

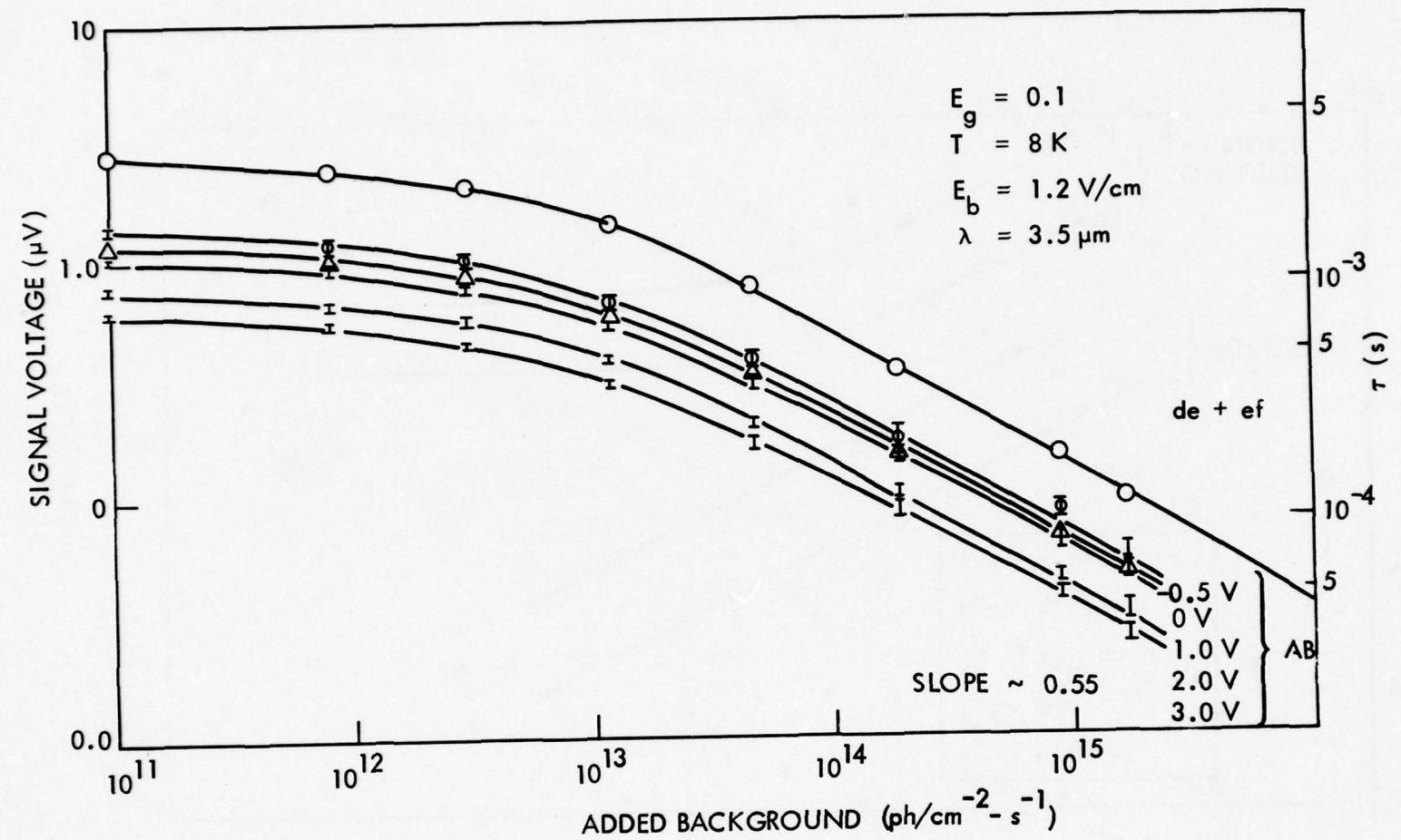

Figure 32. Background dependence of lifetime in 0.1 eV detectors

SURFACE POTENTIAL EFFECTS

The effects of surface potential (i.e. band bending at the surface) were explored using the MIS structure, detector AB. The surface potential was controlled by the applied gate voltage. Computation of the relation between gate voltage and surface potential was discussed in the Surface Potential Variation subsection. The effects of surface potential variation on low frequency responsivity, noise, and the background dependence of lifetime will be presented first for the 0.3 eV gap device and then for the 0.1 eV gap device.

Results on 0.3 eV Energy Gap Devices

The effect of surface potential on low frequency responsivity of the 0.3 eV gap detector is shown in Figure 33. The responsivity, hence lifetime, shows a broad peak approximately at mid gap. A zero or positive surface potential corresponds to a downward bending of the bands at the surface resulting in increased electron density there, while a large negative surface potential corresponds to an upward bending of the bands leading to a depleted or inverted surface layer. At zero gate voltage the surface potential is -0.125 eV. The sharp decline in responsivity (hence lifetime) begins when the surface potential reaches about 0.1 eV above the top of the valence band. The resistance of this device did not change by more than 1 part in 10^3 for the entire range of surface potentials. As the background intensity increased the peak in responsivity shifted towards the valence band and narrowed (Figure 34). At high frequencies the responsivity is independent of surface potential. Since the responsivity at high frequencies depends only on quantum efficiency and is independent of lifetime, we conclude that the quantum efficiency is independent of surface potential. Thus, the low frequency behavior must have been due to a change in lifetime.

The low frequency noise also shows a weak dependence on surface as is shown in Figure 35. The noise (at 10 Hz) is low for values of surface potential away from the band edges but peaks near each band edge.

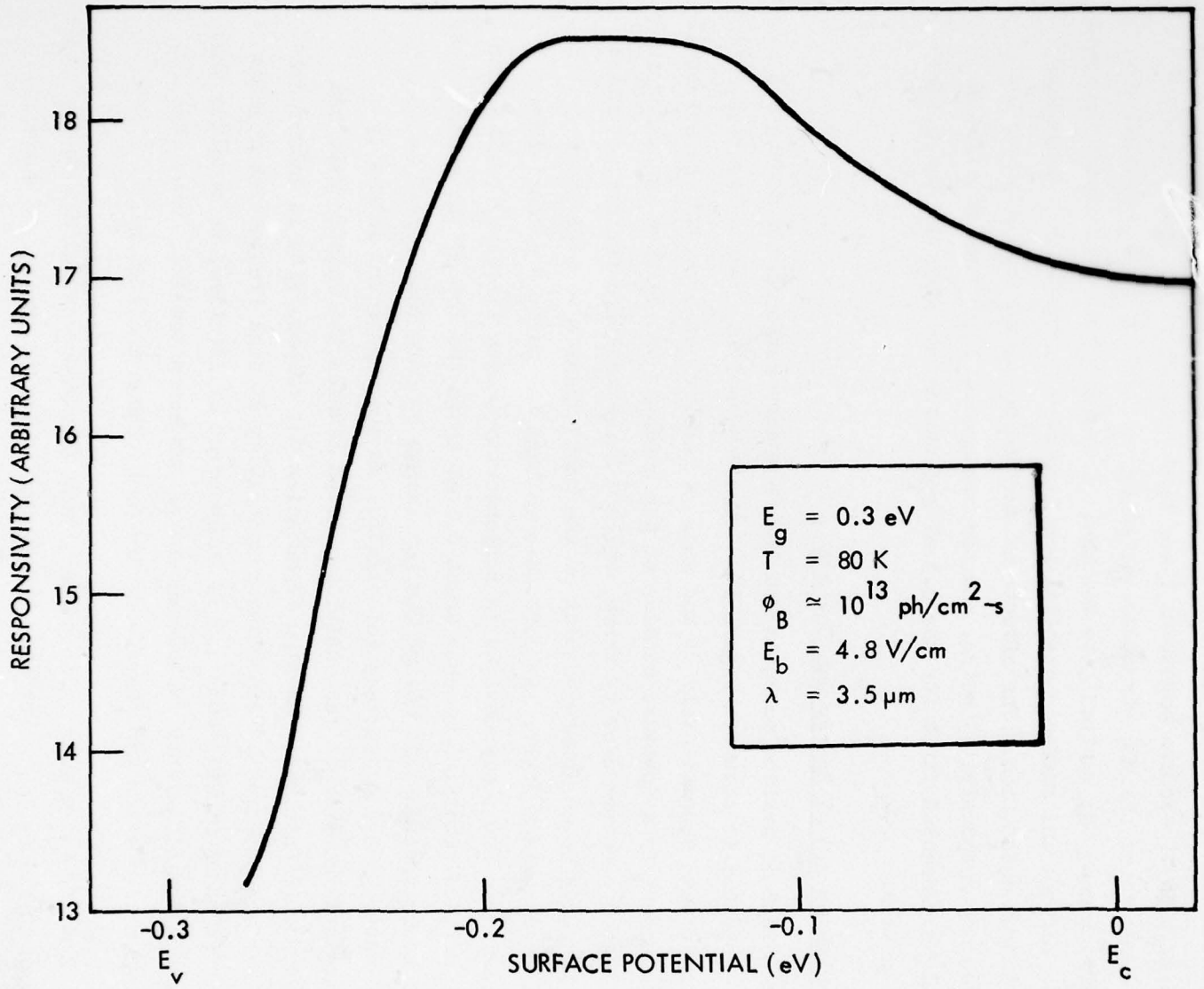

Figure 33. Variation of responsivity with surface potential in 0.3 eV MIS detector (low background)

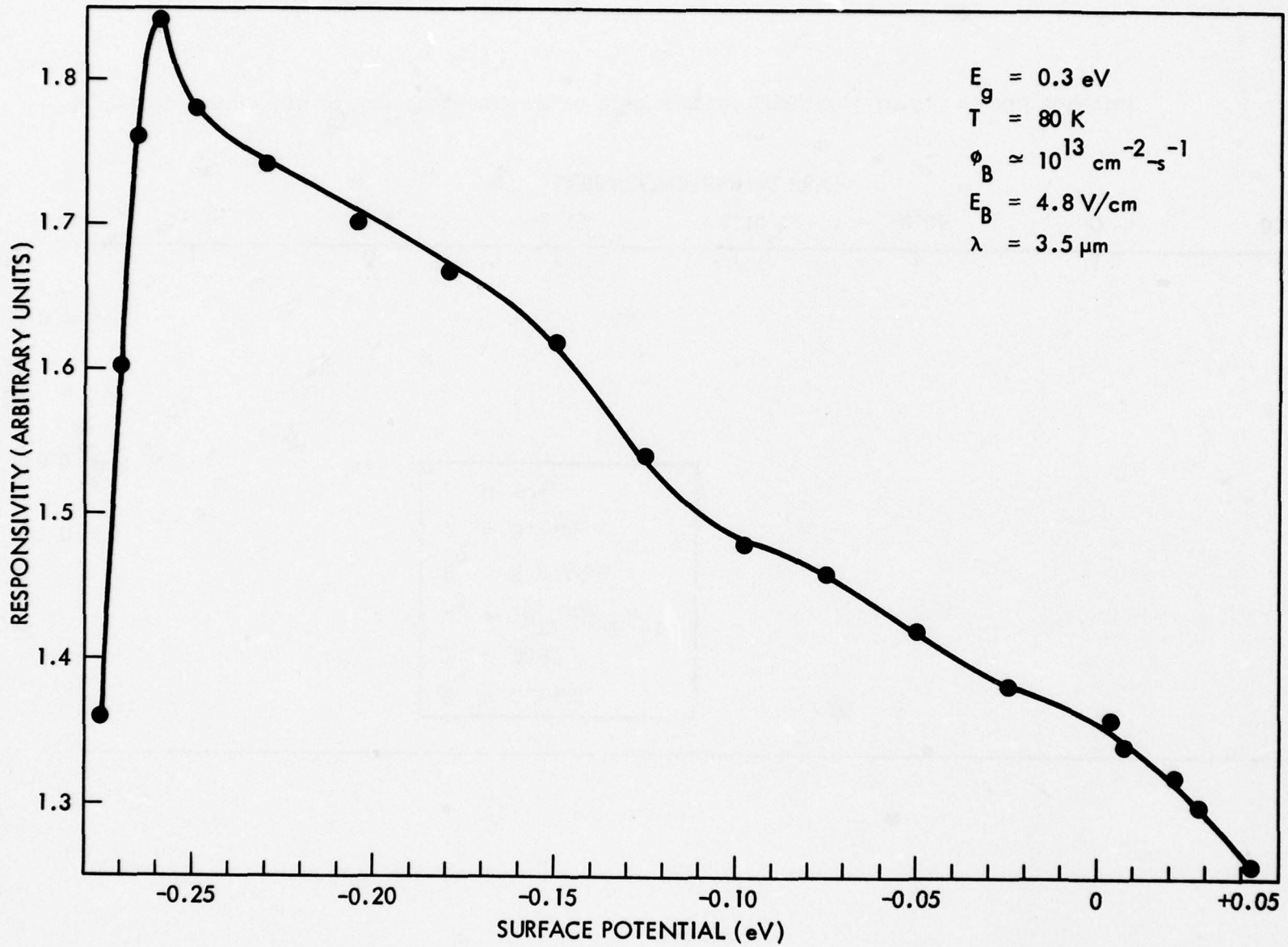

Figure 34. Variation of responsivity with surface potential in 0.3 eV MIS detector (high background)

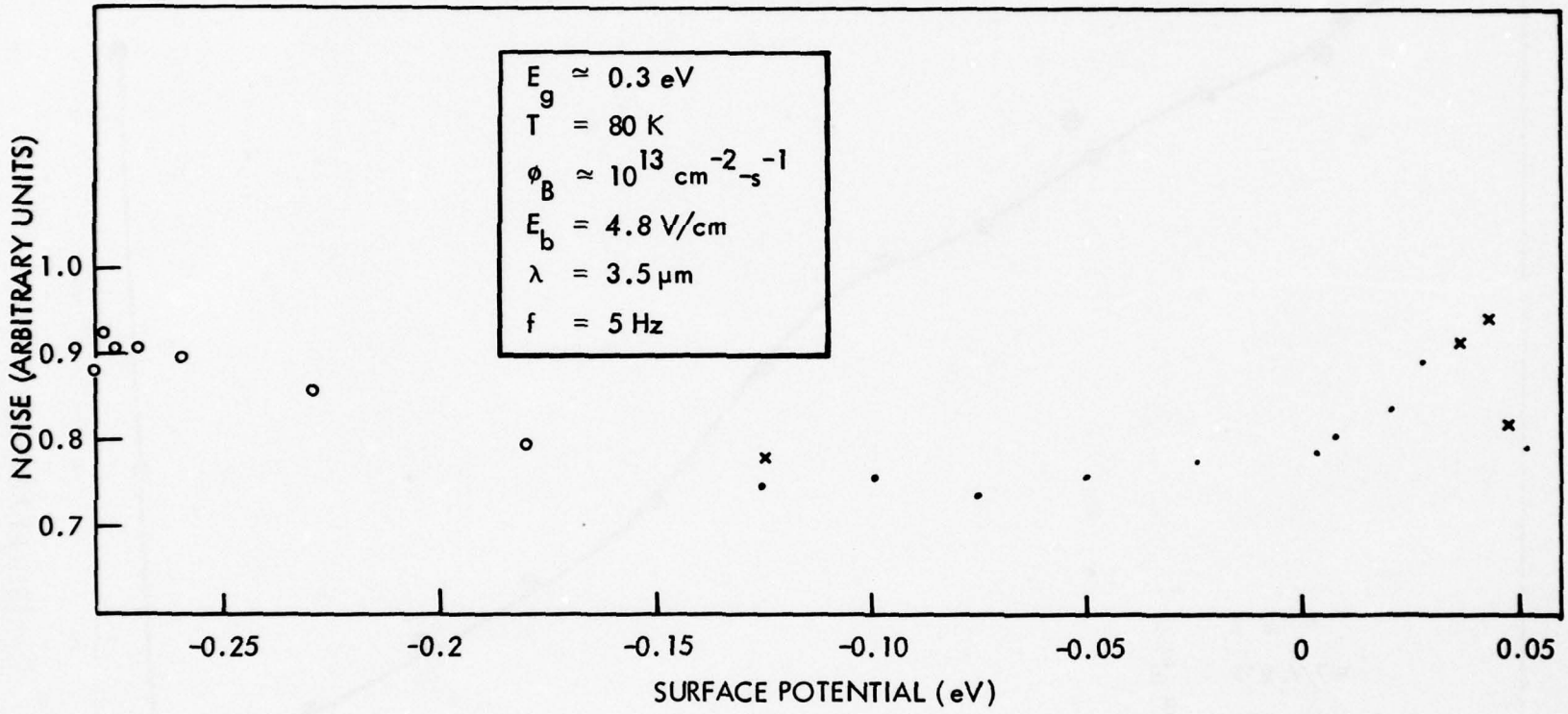

Figure 35. Variation of low frequency noise with surface potential in 0.3 eV MIS detector

In Figure 26 we showed the dependence of lifetime on background, and noted that

$$\tau \sim \frac{K}{\phi_B^{.72}}$$

for zero gate voltage (surface potential of -0.125 eV). Also shown in Figure 26 is the background dependence for gate potentials of ±5 volts.

The slopes of the 0 and +5 volt curves are the same but the lifetime is lower at +5 volts (see Figure 26). The slope of the curve for -5 volts applied gate voltage is however lower. Figure 36 shows the variation in α where

$$\tau \sim \phi_B^{-\alpha}$$

as a function of the surface potential. The exponent is independent of surface potential until the surface potential comes to within about 0.1 eV of the valence band edge. Then it drops precipitously to a constant value of 0.5 for strong inversion.

Results on 0.1 eV Energy Gap Detectors

Surface potential effects in the 0.1 eV gap detector were not as pronounced as in the wider gap device. Unlike the wider gap device, the resistance of this device was dependent on surface potential (Figure 37). This is not surprising since the carrier density in this device is two orders of magnitude lower than the carrier density in the wider gap device. At zero gate voltage the surface potential is -0.095 eV and the surface is already inverted. Applying positive gate voltages brings the surface out of inversion then out of depletion and finally into accumulation. While in inversion the surface layer conductivity is dominated by the low mobility holes. Thus, the detector has a smaller effective thickness and hence higher resistance. With the collapse of the depletion layer and the accumulation of electrons at the surface for larger positive gate voltages the detector resistance drops. In Figure 38 we compare the computed resistance vs. surface

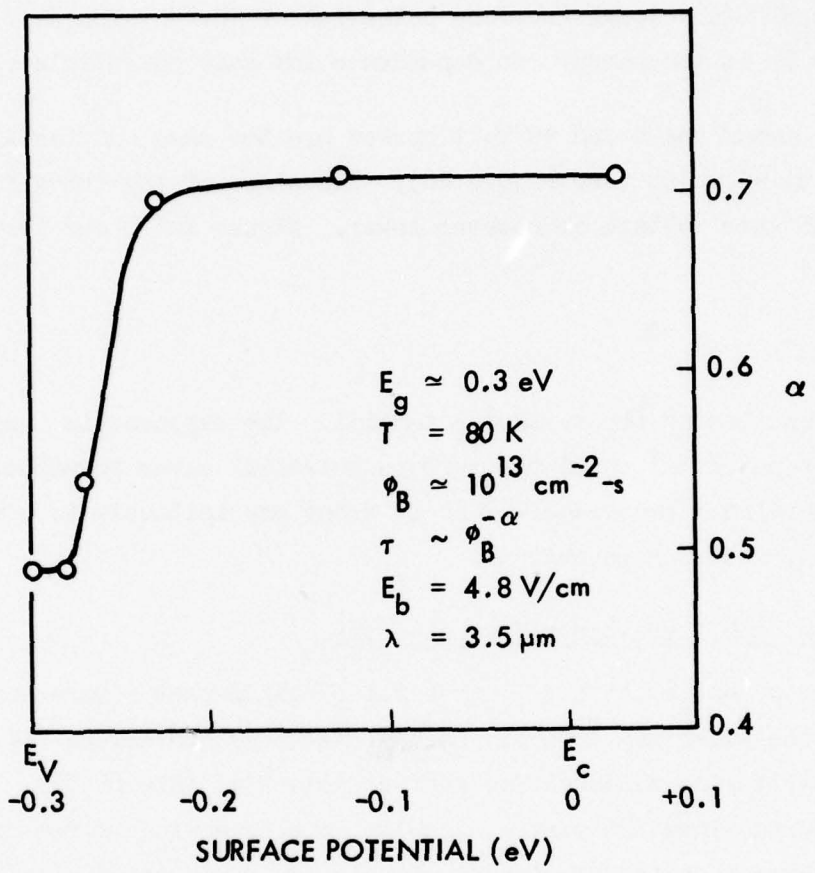

Figure 36. Variation of background exponent α with surface potential in 0.3 eV MIS detector ($\tau \sim \phi_B^{-\alpha}$)

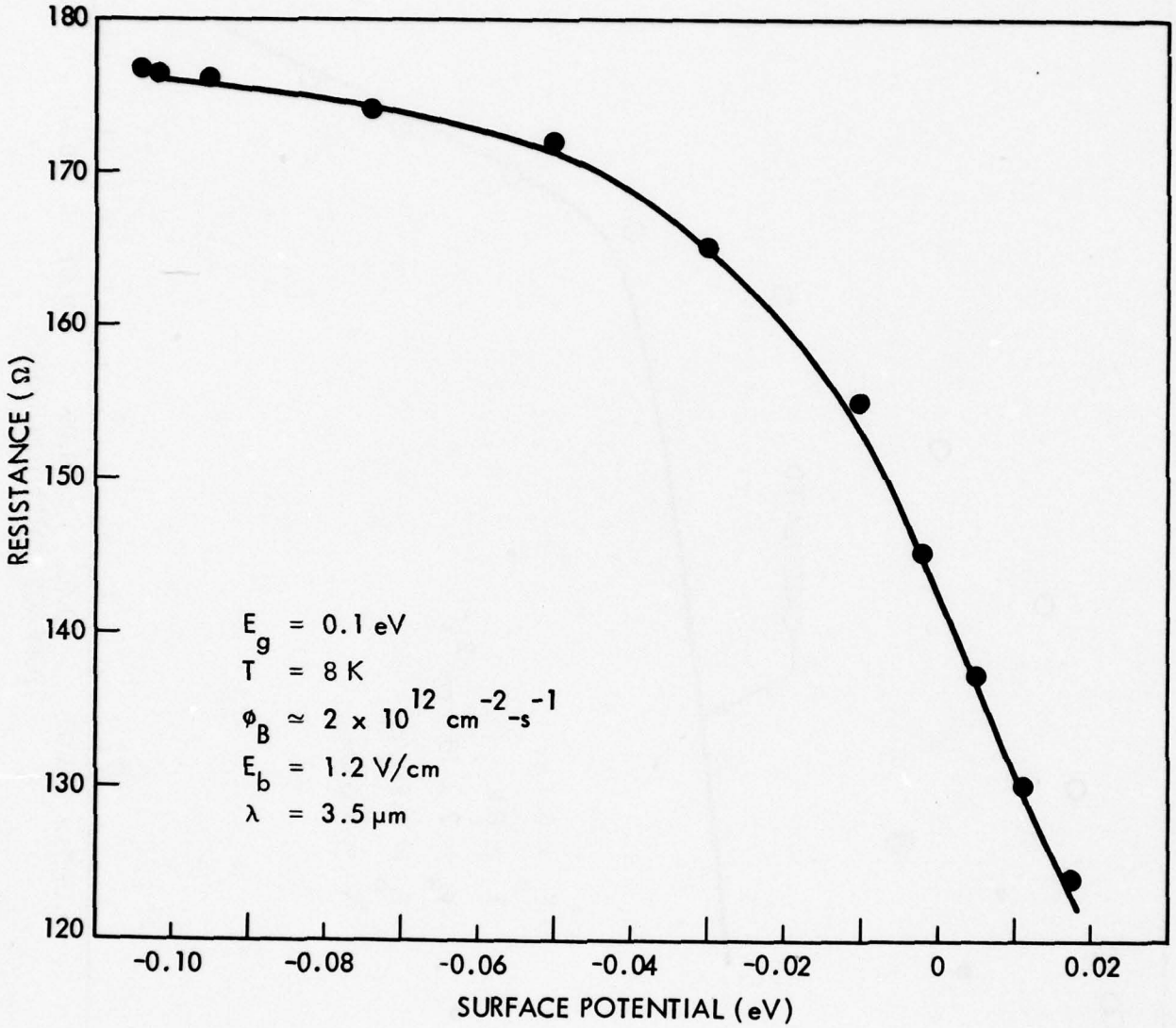

Figure 37. Effect of surface potential on resistance of 0.1 eV MIS device

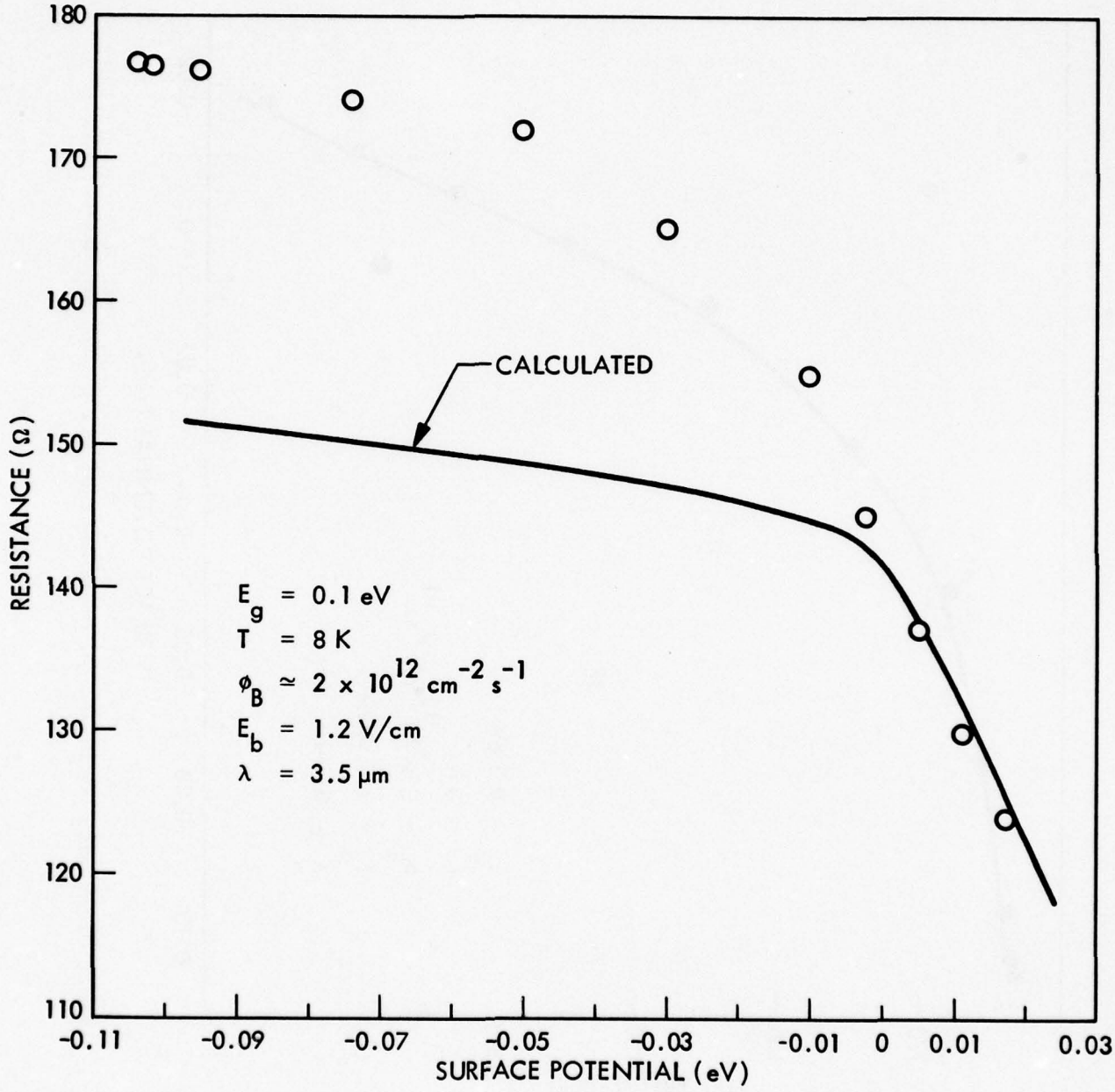

Figure 38. Effect of surface potential on resistance; calculated and measured

potential curve with the measured curve, based on this model. In this computation the computed resistance was normalized to the measured resistance at one point. The agreement in accumulation is quite good but the computed value is low in depletion. However, we feel that the computation essentially verifies the model.

In order to determine whether the lifetime is dependent on surface potential we must examine the behavior of low frequency responsivity/resistance ratio vs. surface potential rather than just responsivity vs. surface potential. This is dictated by the fact that the resistance is surface potential dependent. Figure 39 presents these data. The overall change in the ordinate is not as large as the changes seen in the wider gap sample, but the general behavior is qualitatively the same. The lifetime peaks just below midgap and declines on either side of midgap. At high frequencies the responsivity/resistance ratio is independent of surface potential. Thus the surface potential effects observed in the low frequency measurements can be attributed to a surface potential dependent lifetime.

The low frequency noise vs. surface potential measured with a constant electric field across the detector is shown in Figure 40. Since the noise appears to be excess noise it is field rather than current dependent and therefore must be measured at constant field. It appears from Figure 40 that the noise is insensitive to surface potential. All the data lie within about $\pm\sqrt{2}$ standard deviations from the mean.

In Figure 32 we showed the dependence of low frequency responsivity on background, for zero gate voltage. Also shown is responsivity vs. background for positive gate voltages. The curves for negative gate voltages fall nearly on top of the zero gate voltage curve. All the high background segments of these curves predict the same background dependence of lifetime viz

$$\tau \sim \phi_B^{-.55}$$

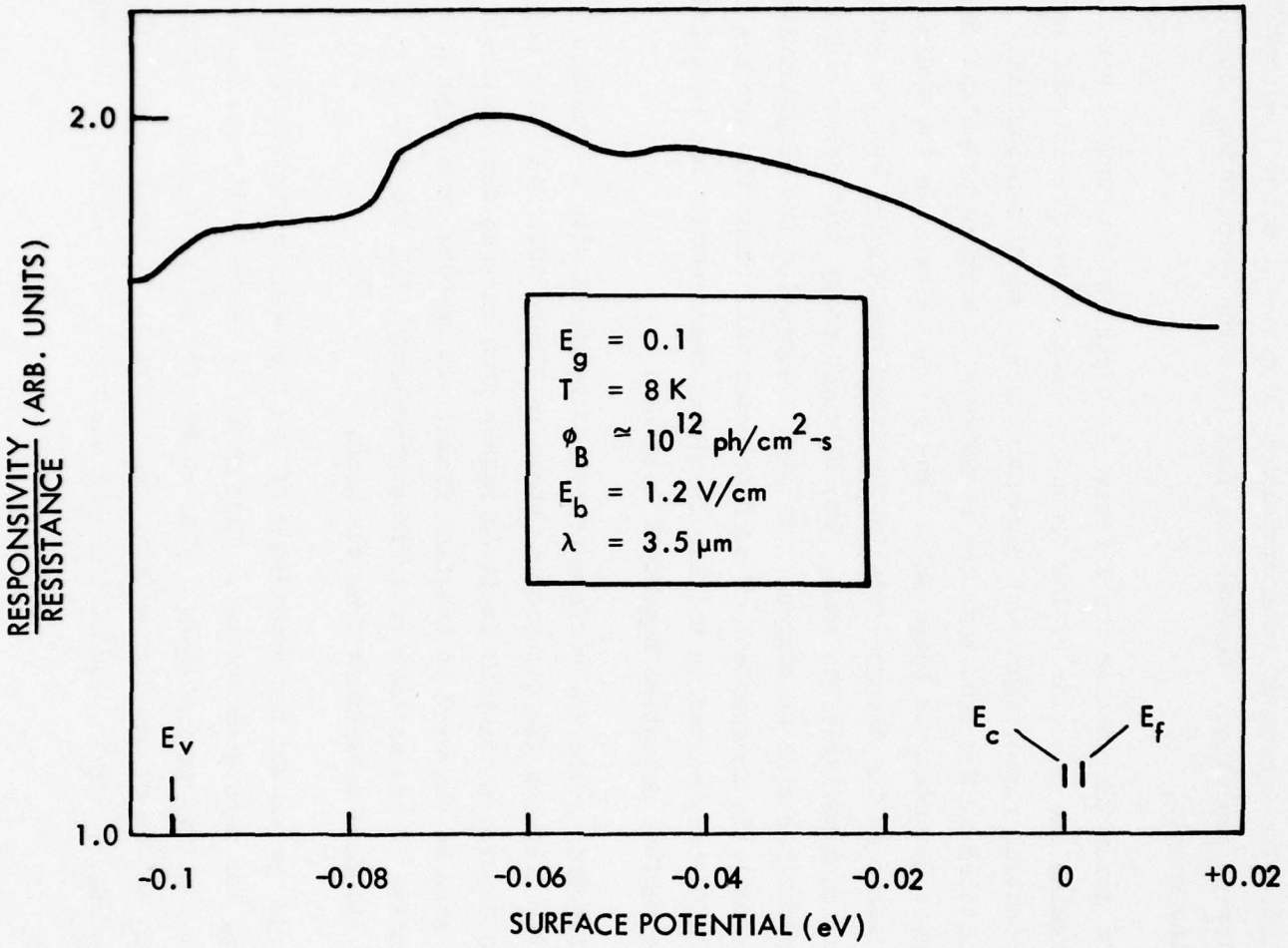

Figure 39. Effect of surface potential on responsivity/resistance in 0.1 eV MIS device

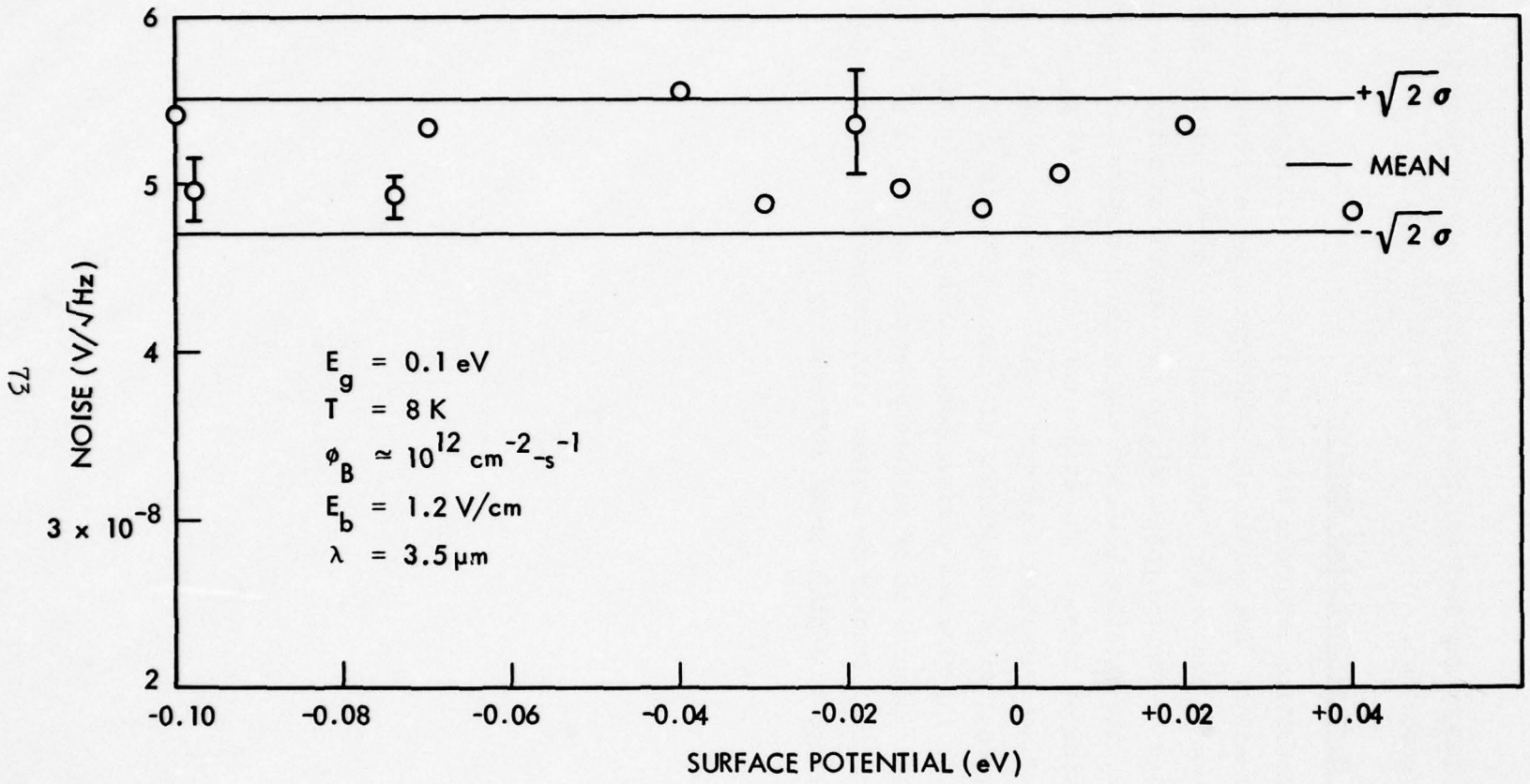

Figure 40. Effect of surface potential on noise in 0.1 eV MIS detector

unlike the larger gap devices, the exponent in this equation is independent of surface potential.

Summary of Surface Potential Effects

In both composition detectors the majority carrier lifetime is dependent on surface potential. The relatively weak dependence of lifetime on surface potential may be due to the fact that the back surface of the detector, which is unaffected by surface potential, always remains an active trapping site. In addition, the lifetime peaks at midgap and decreases for surface potentials on either side of midgap. The excess noise in the 0.3 eV gap detectors was slightly surface potential dependent, while the noise in the 0.1 eV gap detector appears to be independent of surface potential. The background dependence of lifetime was surface potential dependent in the 0.3 eV gap detector, but independent of surface potential in the 0.1 eV gap detector. Surface potential studies on devices with intermediate energy gaps are probably needed to explain these differences.

RADIATION EFFECTS ON DETECTOR PROPERTIES

0.3 eV Energy Gap Devices Co^{60}

Irradiation of these devices was performed with the devices cooled to 80° K. Dose rates were in the range of 300 to 1000 rads/sec. Immediately after irradiation the responsivity and noise were measured. Finally the capacitance vs. voltage measurement was performed. Only after those measurements were completed were the devices allowed to warm above 80° K.

The first irradiation was made to a total dose of 7×10^4 rads. The responsivity and noise, pre and post irradiation of detector AB, are shown in Figure 41. There was a small change in low frequency responsivity and some increase in noise. The increase in noise is too small to be experimentally significant. The responsivity increase is significant and is due to a lengthening of the primary photoconductive lifetime. Detectors de (ZnS coated) and ef also showed an increase in responsivity due to lengthening of the time constant. The responsivity after a room temperature anneal is not quite as high as its pre-irradiation value; however, the shape of the post anneal responsivity curve is identical to the pre-irradiation curve. Thus, the lifetime has returned to its pre-irradiation value, but the detector quantum efficiency has degraded.

The capacitance vs. voltage characteristic was unchanged after irradiation. This implies that neither the surface state density nor the surface potential were affected by irradiation.

According to the trapping model discussed in an earlier section the majority carrier lifetime is monotonically related to the density of trapping centers. In addition the overall quantum efficiency was found to be the product of the usual collection quantum efficiency and an efficiency which measures the relative probability of trapping over recombination. This relative

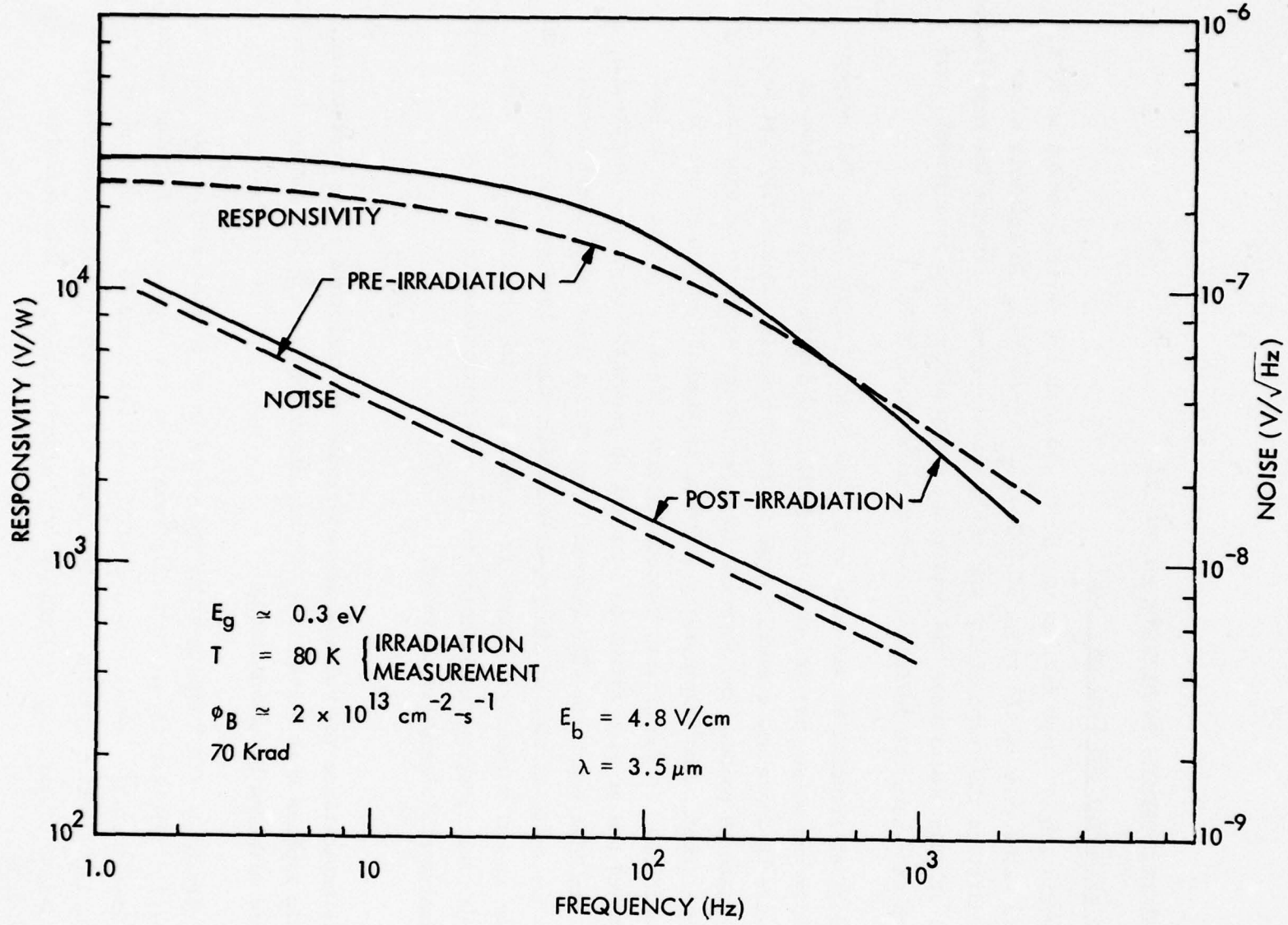

Figure 41. Responsivity and noise in 0.3 eV detector after 70 Krad gamma irradiation

probability η is

$$\eta = \frac{NA}{NA + r_b}$$

where N is the density of trapping sites, A is the capture cross section of the trap multiplied by the hole thermal velocity, and r_b is the rate at which holes recombine via a band to band or flaw assisted process. The product NA is the rate holes are trapped. Thus, η is just the probability that a hole will be trapped. It, too, obviously is dependent on the trap density. Thus, introduction of new trapping sites by irradiation could increase both quantum efficiency and lifetime.

The noise and responsivity of detector AB, following a 2.2×10^5 rad irradiation are shown in Figure 42. The post-irradiation responsivity at low frequencies is about an order of magnitude higher than the pre-irradiation value*. In the roll off region, the differences in responsivity are due primarily to quantum efficiency differences, and it appears from these data that the quantum efficiency has increased about a factor of 2 to 3. From the change in roll off we conclude that the lifetime also has increased by about three. Thus, the change in low frequency responsivity qualitatively tracks with an increase in both lifetime and quantum efficiency.

The capacitance vs. voltage characteristic was changed by irradiation (see "Surface Potential Variation" section). Irradiation increased the density of donor like states at the valence band edge by about a factor of four. The surface potential increases slightly from -0.125 eV to -0.130 eV (Figure 13) below the conduction band. As seen in Figure 33 a change in surface potential in this direction does produce a change in responsivity. However, this change is too small to account for the observed changes. The quantum efficiency and lifetime increases appear to be due to an increase in the density of trapping sites.

---

* When compared to the responsivity after 70 Krad and anneal.

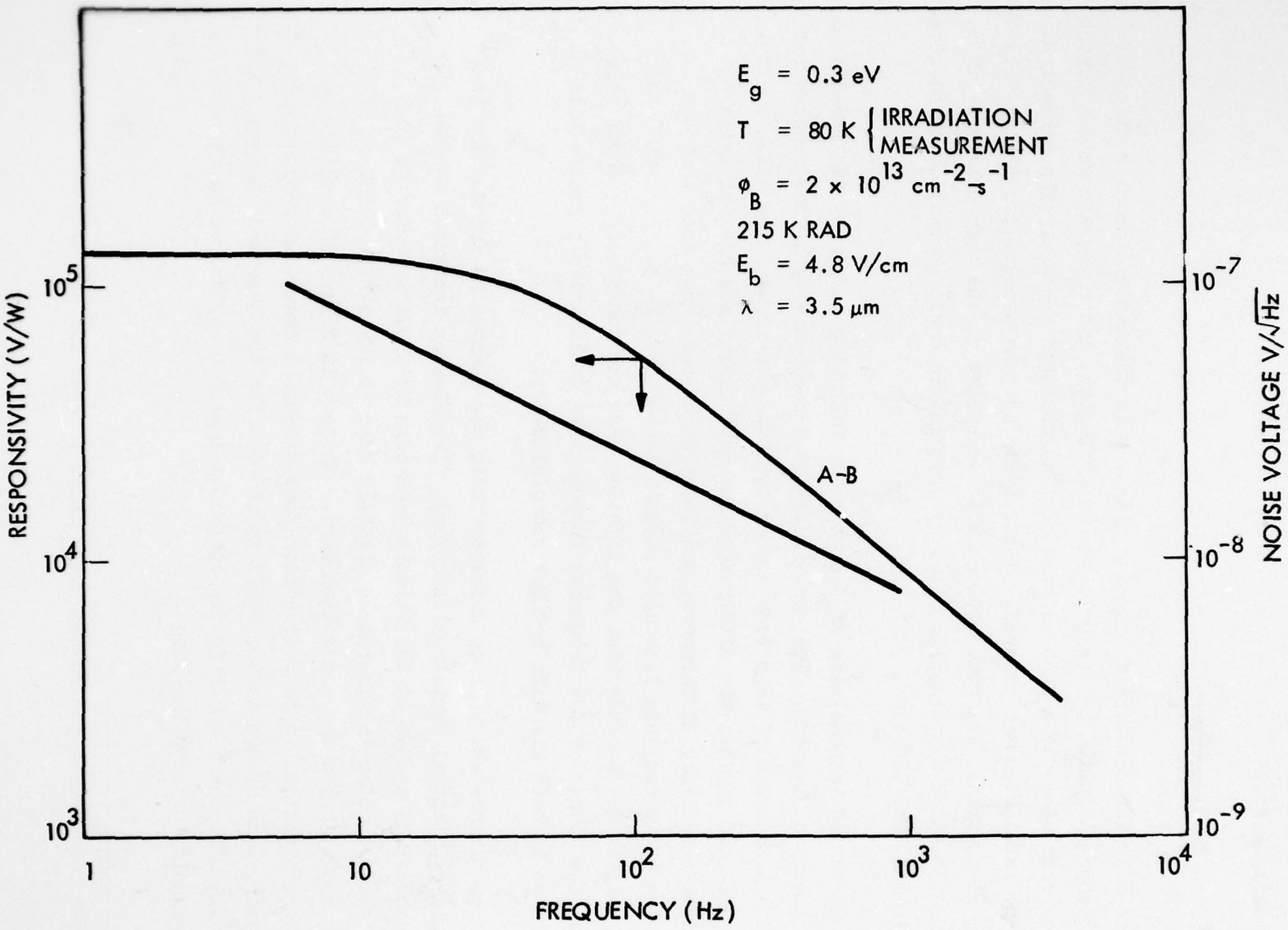

Figure 42. Responsivity and noise in 0.3 eV detector after 2.2×10^5 rad gamma irradiation

Irradiation also increased the excess noise level. This is probably associated with the increase in surface state density.

After a room temperature anneal both responsivity and noise returned to their pre-irradiation value. The new trapping sites are thus not stable at room temperature. (Figure 43.)

0.1 eV Energy Gap Devices

These devices were irradiated at 80° K and then cooled to about 8° K for measurement. Measurements were made in the same sequence as was used for the wide gap devices.

The frequency response of responsivity and noise were measured on these devices after a $1x10^5$ rad and $2.2x10^5$ rad irradiation. The results were identical. Only the results of the $2x10^5$ rad irradiation are shown. The responsivity of detector AB did not change with irradiation. However the adjacent detectors de and ef (Figure 44) experienced a decrease in responsivity in the range of 10-20%. The noise after irradiation of all three detectors AB, de, and ef are within about 25% of their pre-irradiation values. This change is within the limits of experimental error and is probably not significant.

The capacitance vs. voltage characteristic is changed by irradiation (Figure 21). The effect of radiation is to increase the density of donor like surface states and slightly lower the surface potential (from -0.095 eV to -0.104 eV) at zero gate bias. This change in surface potential, according to Figure 39, would only decrease the responsivity by one part in twenty and cannot account for the observed changes. A slight decrease in quantum efficiency would account for the observed changes. This is quite consistent with the data since the pre- and post-irradiation data are nearly parallel, indicating a change in quantum efficiency and not in lifetime. This decrease in quantum efficiency could be due to a radiation induced increase in the density of recombination sites. The fact that de and ef behave slightly

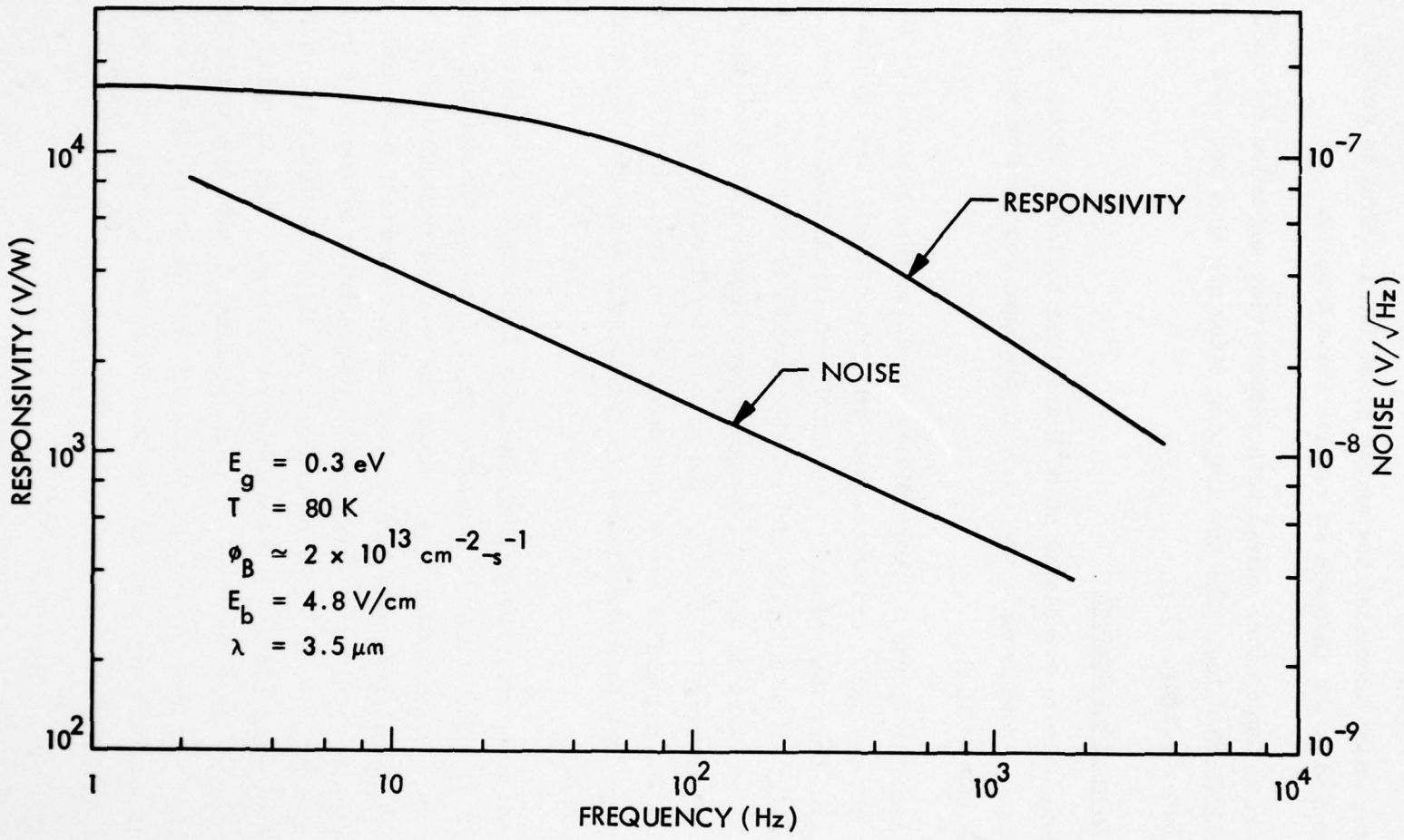

Figure 43. Responsivity and noise in 0.3 eV detector after 2.2×10^5 rad gamma irradiation and room temperature anneal

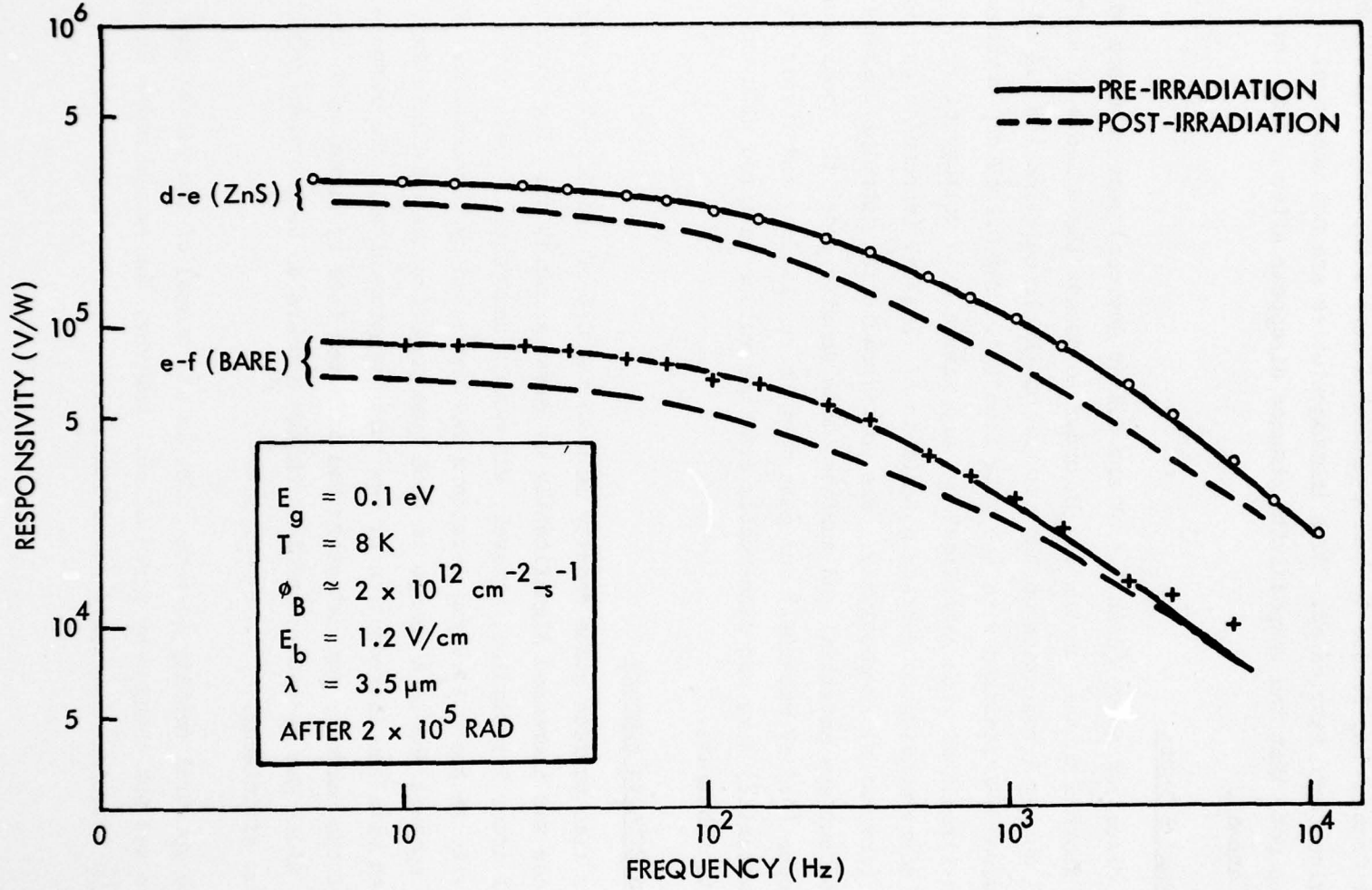

Figure 44. Responsivity and noise in 0.1 eV detectors after 2x10^5 rad gamma irradiation

different from AB may be due to inhomogenieties across the chip from which these devices were fabricated. Such inhomogenieties are not uncommon. Finally we note that the responsivity changes disappear after a room temperature anneal.

Gate Voltage Effects

The data discussed above (both 0.3 eV and 0.1 eV devices) were obtained with the gate shorted to the substrate. In order to assess the effects of surface potential during irradiation on the outcome of the irradiation the 0.3 eV devices were re-irradiated with the gate floating. The 0.1 eV gap devices were also irradiated with gate floating, and with a gate voltage of +2 V and -1 V corresponding to surface potentials of +.017 eV (accumulation) and -0.104 eV (inversion) respectively. The post-irradiation detector characteristics, surface potential and surface state density under the conditions of gate open (0.3 eV material) and gate open, accumulation, and inversion (0.1 eV material) were not discernable from the values measured with the gate shorted to substrate.

Radiation Effects Summary

The donor like surface state density on both the 0.3 eV and 0.1 eV energy gap devices was increased significantly by gamma irradiation. The surface potential after irradiation, however, was nearly unaffected. Detector responsivity in the 0.3 eV gap detectors was increased by irradiation. The increase appears due to a change in both quantum efficiency and lifetime, associated with the introduction of new bulk trapping sites. The responsivity of the narrower gap detectors was affected less by irradiation than were the wider gap detectors and this change appears to be a slight reduction in quantum efficiency.

The noise spectral density (excess noise in all cases) of the 0.1 eV gap detectors was not changed by irradiation. However, the excess noise in the 0.3 eV gap detectors increased significantly.

Finally, we observe that the detector surface potential during irradiation does not affect the outcome of the irradiation.

DISCUSSION

Trapping mode HgCdTe photoconductive detectors with energy gaps of 0.3 eV and 0.1 eV were studied in this program. Three detector configurations of each composition were used: (1) an uncoated detector representing an unperturbed "normal" detector, (2) a ZnS coated detector, and (3) a MIS device consisting of detector ZnS, and a semitransparent Au electrode. These studies showed that all detectors had qualitatively the same general characteristics, with no systematic variations due to surface configuration. The photoconductive lifetimes were in the range of 1-3.5 msec and the quantum efficiencies were in the range of 0.02 to 0.2. The frequency dependence of responsivity in all detectors showed the usual, slower than 1/f roll off. All detectors were excess noise limited at the backgrounds used. The photoconductive lifetimes were background dependent and varied as $\tau \sim \phi^{-\alpha}$ with $\alpha = 0.55$ in the 0.1 eV material and $\alpha \simeq 0.7$ (at $V_g = 0$) in the 0.3 eV material. The exponent α was found to be <u>independent</u> of temperature (Figures 26 and 27) but not independent of surface potential in the wider gap material (Figure 36).

The surface state density per unit energy interval was similar in the MIS devices of both composition and peaked at the band edges (Figures 12 and 20).

The photoconductive lifetimes in both compositions are dependent on surface potential and have broad peaks near midgap. The departures from this maximum value, however are not large (Figures 33 and 39). The exponent in the power low dependence of lifetime on background is surface potential dependent in the 0.3 eV gap detectors. The exponent remains constant at 0.7 until the surface is biased into inversion, at which point α rapidly drops to ~ 0.5. The 0.1 eV gap device did not show this effect.

Gamma irradiation of detectors of both compositions resulted in an increase in the density of donor like surface states at the valence band edge. The responsivity and noise of the wider gap detectors increased significantly

upon irradiation while the responsivity of the narrow gap devices decreased only slightly and the noise was unchanged. The surface potential after irradiation was unchanged in both composition detectors. These results, or at least the effect of irradiation on responsivity, are important since they argue against a surface state dominated trapping mechanism. We note that in the wider gap detector the pre and post irradiation surface potential resided at about -0.125 eV below the conduction band, that is in the region where irradiation had no dramatic effect on surface state density. However, the responsivity increased significantly after irradiation. Likewise, the surface potential in the narrower gap device was unchanged after irradiation and remained at the valence band edge. The surface state density at the valence band edge increased significantly. Now, however, we see almost no change in responsivity. Thus, on the one hand we have a large change in responsivity after irradiation in the detector in which the fermi energy resides in a region of unperturbed surface state density while in the detector in which the fermi energy resides near a maximum in the surface state density, which is increased further by irradiation, the responsivity is unchanged by irradiation. These two results strongly suggest that surface states do not play a part in the minority carrier trapping process.

All data on trapping mode HgCdTe indicate that the presence of some kind of sensitizing center is required to provide minority carrier trapping. In addition, the soft roll off of responsivity with frequency and the dependence of lifetime on background suggest that the trapping process cannot be described in terms of a single time constant trapping process. For a single time constant process the responsivity falls off as 1/f at high frequencies and $\tau \sim \phi_B^{-1}$. This behavior is not observed in HgCdTe. Thus, the trapping process must also allow for a spectrum of time constants and a background dependence of lifetime of the form $\tau \sim \phi_B^{-\alpha}$ where α is less than 1 but greater than 0.5. Three models have been proposed to account for the trapping process: (1) the trapping process is governed by a distribution of surface states, (2) trapping is due to an exponential distribution of bulk states across the energy gap, and (3) trapping is due to a monoenergetic bulk trapping state whose properties are controlled by band bending at the

surface. The required distribution of time constants and proper background dependence of lifetime can be obtained in principal from these models.

The radiation effects results discussed earlier are not compatible with a surface state controlled trapping model. In addition, we recall that the responsivity peaks when the surface is in depletion, when there are essentially no majority carriers at the surface. Since the surface states can only communicate with the bulk via majority carriers, surface states are effectively decoupled from the bulk when the surface is in depletion or inversion [30]. This result cannot be reconciled with the fact that the lifetime is maximum when the surface is depleted. Thus, the surface state approach to trapping does not appear to be consistent with observation.

Model (2) due to Beck and Broudy [31] while it satisfactorily provides a mechanism for a spectrum of time constants and the correct value of α also predicts that α will be temperature dependent and will increase with decreasing temperature. In the "Detector Properties" section we reported that the exponent remained constant or decreased slightly when the detector was cooled from 80°K to 10°K (Figures 26 and 27). This result cannot be reconciled with this model and suggests that trapping is not due to a distribution of bulk trapping states.

The final model which we discuss employs a single bulk state, in particular a doubly ionized acceptor, in conjunction with a depleted surface to account for the characteristics of trapping detectors. The results of this program are suggestive that this model has merit. In particular, we cite the data on the effect of surface potential on responsivity. The lifetime peaks in depletion and decreases for inversion and accumulation as is expected from the model. The fact that there is not a more dramatic change in lifetime is probably due to the fact that only one surface is affected by the field

---

[30] S. R. Hofstein and G. Warfield, Sol. State Elect. 8 321 (1966)
[31] J. Beck and R. Broudy, op. cit.

plate. Due to the long diffusion lengths the back surface of the device, which is prepared in the same manner as the front surface, remains an active trapping region, regardless of the surface potential of the front surface. We highly recommend that further studies on devices which can have both surfaces controlled or on devices which are accumulated on both surfaces be performed to test the validity of this model.

We also should point out that this model predicts that the exponent α is independent of temperature, as is observed.

Finally, the radiation effects data are not inconsistent with this model. Bulk damage due to gamma irradiation results in isolated defects which usually have only a few energy levels associated with them. Previous radiation studies on HgCdTe [32] showed that gamma irradiation, at low temperatures, introduces electrically active damage sites at the rate of 10^{8} cm^{-3} rad^{-1}. Thus, after $2x10^{5}$ rads we expect about $2x10^{13}$ cm^{-3} damage sites. This is comparable to the number of native trapping sites (10^{13} cm^{-3}) as deduced from other studies [14]. Therefore, the number of radiation induced trapping sites is of the right order of magnitude to affect both lifetime and quantum efficiency assuming the site has the correct capture cross-section and energy level. While Mallon et al. detected only donor levels, the presence of a comparable number of acceptors would not have been observed because of the high (10^{17} $cm^{-2}s^{-1}$) optical background in these experiments.

In summary, we have characterized the surface properties of HgCdTe detectors, and studied radiation effects in these devices. The observed radiation effects depend on energy gap but not on surface potential. In addition these studies suggest that trapping behavior is not due to either surface states, or a distribution of bulk states. The data is consistent with a trapping model based on the presence of a depleted surface and a single monoenergetic bulk trapping site.

---

[32] C. E. Mallon et al. IEEE Trans. Nucl. Sci. Vol NS-22, 2283 (1975)
[14] Detector Test Program, op. cit.

APPENDIX A

I. CALCULATION OF BULK CONTRIBUTION TO $Q_{\square}(V_s)$ and $dQ_{\square}/dV_s$.

This development follows the analysis of Michael and Leonard for a semiconductor having a nonparabolic conduction band and a parabolic valence band [A1]. The nonparabolic conduction band is described by Kane's $\vec{k}\cdot\vec{p}$ approximation with a minimum at Γ in the Brillouin zone [A2]. The parabolic approximation to the valence band is valid since the heavy hole band dominates the valence band density of states function in narrow band gap II-VI compound semiconductors.

The sense in which potentials, energies and charges are to be referenced is indicated schematically in Figure A.

The analytical problem is to solve Poisson's equation in the semiconductor:

$$\frac{d^2V}{dx^2} = -\frac{q}{\epsilon_s}(p - p_B - n + n_B) \qquad \text{(A1)}$$

where

$$p_B = N_v \frac{2}{\sqrt{\pi}} \int_o^\infty \frac{\epsilon^{\frac{1}{2}}}{1 + e^{\epsilon+\varphi+t}}\, d\epsilon$$

is the bulk thermal equilibrium hole concentration,

$$n_B = N_c \frac{2}{\sqrt{\pi}} \int_o^\infty \frac{\epsilon^{\frac{1}{2}}(1 + \frac{\epsilon}{\varphi})^{\frac{1}{2}}\,(1 + \frac{2\epsilon}{\varphi})}{1 + e^{\epsilon-t}}\, d\epsilon$$

is the bulk thermal equilibrium electron concentration,

$$p(x) = p(V(x)) = N_v \frac{2}{\sqrt{\pi}} \int_o^\infty \frac{\epsilon^{\frac{1}{2}}}{1 + e^{\epsilon+\varphi+t+v(x)}}\, d\epsilon$$

A1. Michael and Leonard, Solid-State Electronics 17, 71 (1974)
A2. W. W. Anderson, Infrared Phys. 17, 147 (1977)

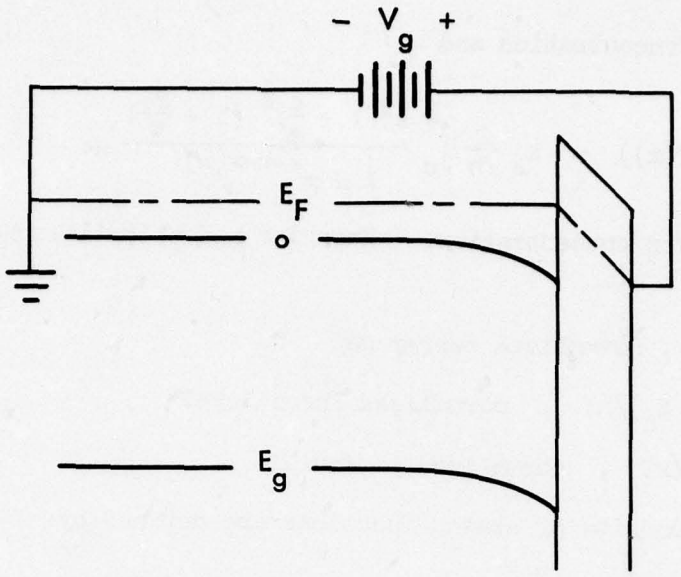

a. Energy level diagram of n-type MIS structure

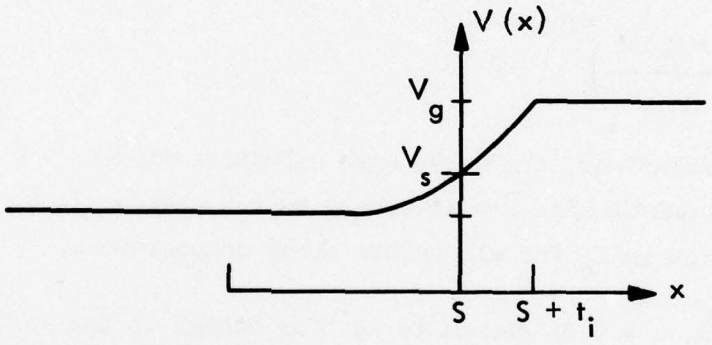

b. Potential variation through MIS structure. Note that $V_g = V_s + Q_\square t_i/\epsilon_i$

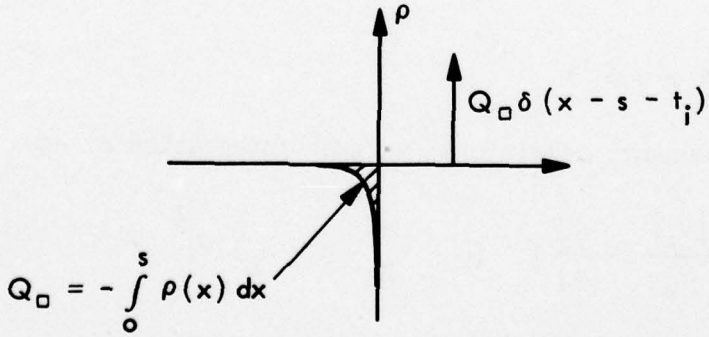

c. Charge distribution through MIS structure

Figure A. Sign convention for potentials, energies, and charges in analysis of semiconductor surface potential

is the local hole concentration and

$$n(x) = n(V(x)) = N_c \frac{2}{\sqrt{\pi}} \int_o^\infty \frac{\epsilon^{\frac{1}{2}}(1 + \frac{\epsilon}{\varphi})^{\frac{1}{2}} (1 + \frac{2\epsilon}{\varphi})}{1 + e^{\epsilon - t - v(x)}} d\epsilon$$

is the local electron concentration. Energies and potentials have been normalized as:

$\varphi \equiv E_g/kT$, normalized energy gap

$t \equiv (E_F - E_c)/kT$, normalized Fermi level

$v \equiv qV(x)/kT$, normalized potential

and the effective density of states functions are defined by:

$$N_v \equiv 2\left(\frac{2\pi\, m_h^*\, kT}{h^2}\right)^{3/2}$$

$$N_c \equiv 2\left(\frac{3\, E_g\, kT}{8\pi\, P^2}\right)^{3/2} .$$

In subsequent calculations, the heavy hole effective mass is taken to be $m_h^* = .55\ m_o$ in N_v and the Kane $\vec{k}\cdot\vec{p}$ interband matrix element is $P = 8.4 \times 10^{-8}$ eV·cm in N_c for all HgCdTe alloy compositions.

In Figure A, x = 0 is chosen to be "far enough to the left" so that

$$V(x = 0) = 0$$

and

$$\frac{dV}{dx} = 0 \quad \text{at } x = 0 .$$

Subject to these boundary conditions, a first integration of eqn. (A1) gives

$$\left.\frac{dV}{dx}\right|_{x=s} = \frac{|V_s|}{V_s}\left[-\frac{2q}{\epsilon_s}\int_o^{V_s}(p - p_B - n + n_B)dV\right]^{\frac{1}{2}} . \qquad (A2)$$

However, from Gauss' law,

$$\left.\frac{dV}{dx}\right|_{x=s} = \frac{Q_{\square}(\text{bulk})}{\epsilon_s}$$

so that:

$$Q_{\square}(\text{bulk}) = \frac{|V_s|}{V_s}\sqrt{2q\,\epsilon_s}\left[-\int_o^{V_s}(p - p_B - n + n_B)\,dV\right]^{\frac{1}{2}} \tag{A3}$$

and:

$$\frac{d\,Q_{\square}(\text{bulk})}{d\,V_s} = \frac{q\,\epsilon_s}{Q_{\square}(\text{bulk})}\left(-p(V_s) + p_B + n(V_s) - n_B\right) . \tag{A4}$$

Eqns. (A3) and (A4) may be written as:

$$Q_{\square}(\text{bulk}) = \frac{|v_s|}{v_s}\frac{2}{\pi^{1/4}}\sqrt{\epsilon_s\,kT\,N_v}\left[\frac{2}{3}(I_4 - I_2) + v_s I_1 - v_s\frac{N_c}{N_v}I_3 - \frac{N_c}{N_v}I_5\right]^{\frac{1}{2}} \tag{A5}$$

and:

$$\frac{dQ_{\square}(\text{bulk})}{d\,V_s} = \frac{q\,\epsilon_s}{Q_{\square}(\text{bulk})}\left[-I_6 + I_1 + \frac{N_c}{N_v}(I_7 - I_3)\right] \tag{A6}$$

so that the computational problem is reduced to evaluation of the seven integrals:

$$I_1 = \int_o^{\infty}\frac{\epsilon^{\frac{1}{2}}\,d\epsilon}{1 + e^{\epsilon+\varphi+t}}$$

$$I_2 = \int_o^{\infty}\frac{\epsilon^{3/2}\,d\epsilon}{1 + e^{\epsilon+\varphi+t}}$$

$$I_3 = \int_o^{\infty}\frac{\epsilon^{\frac{1}{2}}\left(1 + \frac{\epsilon}{\varphi}\right)^{\frac{1}{2}}\left(1 + \frac{2\epsilon}{\varphi}\right)}{1 + e^{\epsilon-t}}\,d\epsilon$$

AD-A058 698 LOCKHEED MISSILES AND SPACE CO INC PALO ALTO CALIF PA--ETC F/G 6/18
RADIATION EFFECTS OF IR DETECTORS.(U)
MAR 78 F A JUNGA, W W ANDERSON, R B EMMONS F19628-75-C-0127

UNCLASSIFIED LMSC/D566051 RADC-TR-78-66 NL

2 OF 2
AD
A058 698

END
DATE
FILMED
11-78
DDC

$$I_4 = \int_0^\infty \frac{\varepsilon^{3/2}\, d\varepsilon}{1 + e^{\varepsilon+\varphi+t+v_s}}$$

$$I_5 = \int_0^\infty \varepsilon^{\frac{1}{2}}\left(1 + \frac{\varepsilon}{\varphi}\right)^{\frac{1}{2}} \left(1 + \frac{2\varepsilon}{\varphi}\right) \ln\left(\frac{e^{t} + e^{\varepsilon}}{e^{v_s+t} + e^{\varepsilon}}\right) d\varepsilon$$

$$I_6 = \int_0^\infty \frac{\varepsilon^{\frac{1}{2}}\, d\varepsilon}{1 + e^{\varepsilon+\varphi+t+v_s}}$$

$$I_7 = \int_0^\infty \frac{\varepsilon^{\frac{1}{2}}\left(1 + \frac{\varepsilon}{\varphi}\right)^{\frac{1}{2}} \left(1 + \frac{2\varepsilon}{\varphi}\right)}{1 + e^{\varepsilon-t-v_s}} d\varepsilon \quad .$$

Integrals I_1 and I_2 are always negligible in the extrinsic n-type materials of interest in this work. Integral I_3 is determined by the defect doping density

$$I_3 = \frac{\sqrt{\pi}}{2} \frac{n_B}{N_c}$$

and is used to determine the Fermi level, t, when the bulk majority carrier density is known. Since I_3 can not be solved explicitly for t, a set of curves of n/N_c vs t with φ as a parameter was calculated as shown in Figure B. When the majority carrier density, n_B, and energy gap, E_g, are known, t is readily obtained from Figure B for use in evaluating I_4 through I_7.

Evaluation of integrals I_4 through I_7 is further simplified by the following approximations:

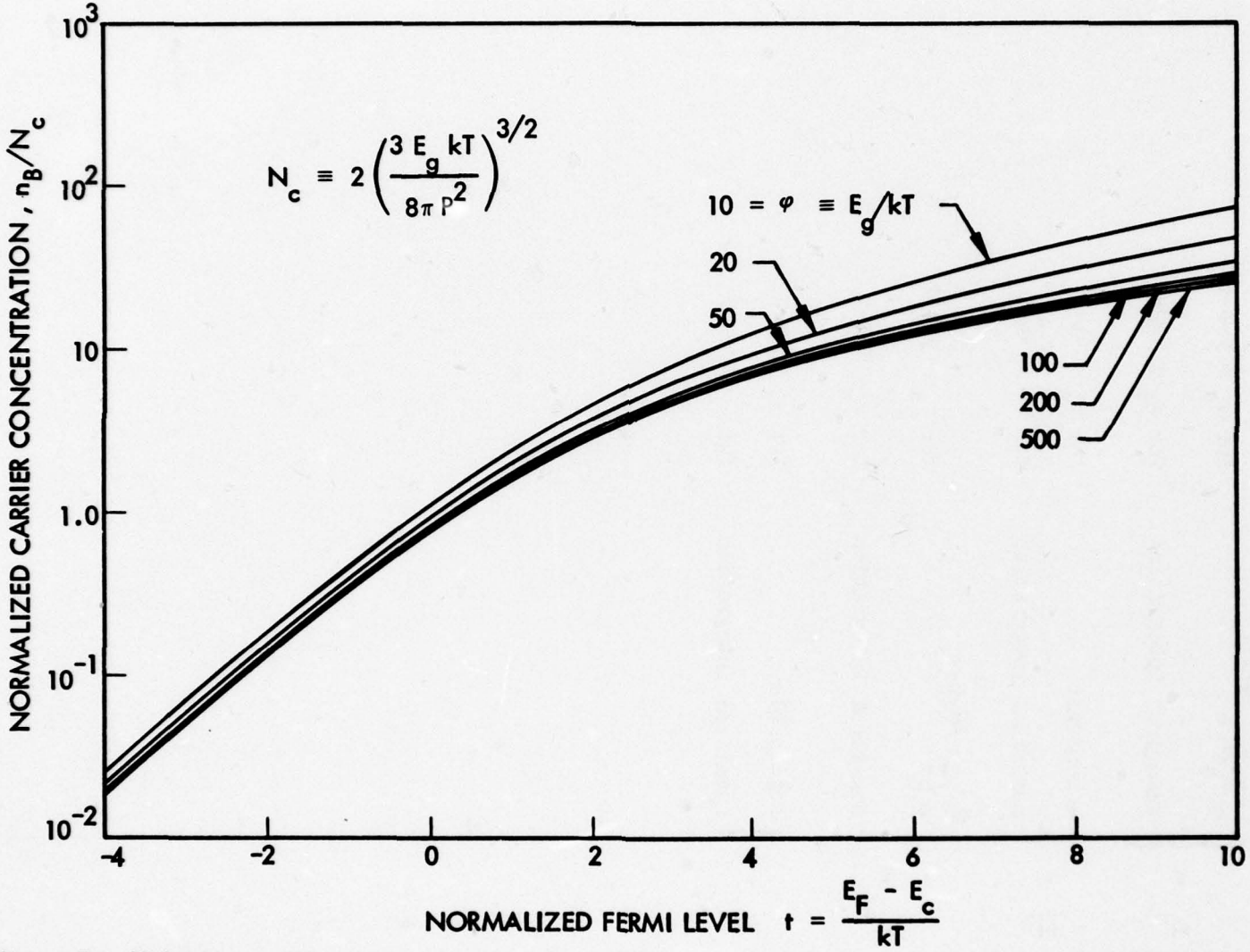

Figure B. Majority carrier concentration in HgCdTe as a function of fermi level with energy gap as a parameter. These curves are used to determine t when given n_B/N_c and φ

$$I_4 = \begin{cases} \approx \frac{3\sqrt{\pi}}{4} e^{-\varphi-t-v_s} & \text{for } v_s > 5-\varphi-t \\ \text{numerical integration} & \text{for } v_s < 5-\varphi-t \end{cases}$$

$$I_5 = \begin{cases} \approx \text{constant} & \text{for } v_s < -t-5 \\ \text{numerical integration} & \text{for } v_s > -t-5 \end{cases}$$

$$I_6 = \begin{cases} \approx \frac{\sqrt{\pi}}{2} e^{-\varphi-t-v_s} & \text{for } v_s > 5-\varphi-t \\ \text{numerical integration} & \text{for } v_s < 5-\varphi-t \end{cases}$$

$$I_7 = \begin{cases} \text{negligible} & \text{for } v_s < -t-5 \\ \text{numerical integration} & \text{for } v_s > -t-5 \end{cases}$$

II. CALCULATION OF SURFACE STATE CONTRIBUTION TO $Q_{\square}(V_s)$ AND $dQ_{\square}/dV_s$.

The relation of surface state energy and occupancy to semiconductor bulk energy levels is indicated in Figure C. Two types of surface states are indicated, acceptor and donor. An acceptor type surface state is characterized by the two charge states, negative or neutral while a donor type surface state is characterized by the two charge states, positive or neutral. It is assumed that donor type state distributions peak near the valence band edge while acceptor type state distributions peak near the conduction band edge. At low temperatures, all donor states above the surface Fermi level are positively charged and all acceptor states below the surface Fermi level are negatively charged.

If the total surface state distribution is given by:

$$N_{ss}(E_s) = N_{ssD}(E_s) + N_{ssA}(E_s) \tag{A7}$$

where $N_{ssD}(E_s)$ is the donor distribution and $N_{ssA}(E_s)$ is the acceptor distribution then

$$Q_{\square} = q\,kT\left[\int_{-\infty}^{\infty} \frac{N_{ssA}(\epsilon + v_s)}{1 + e^{\epsilon - t}}\,d\epsilon - \int_{-\infty}^{\infty} \frac{N_{ssD}(\epsilon + v_s)}{1 + e^{t - \epsilon}}\,d\epsilon\right] . \tag{A8}$$

The normalized surface state energy has been referred to the bulk energy reference level by:

$$E_s = E + V_s = kT(\epsilon + v_s) .$$

Note also the sign reversal in Eqn. (A8) due to choice of $Q_{\square}$ as positive charge on the gate electrode in Figure A.

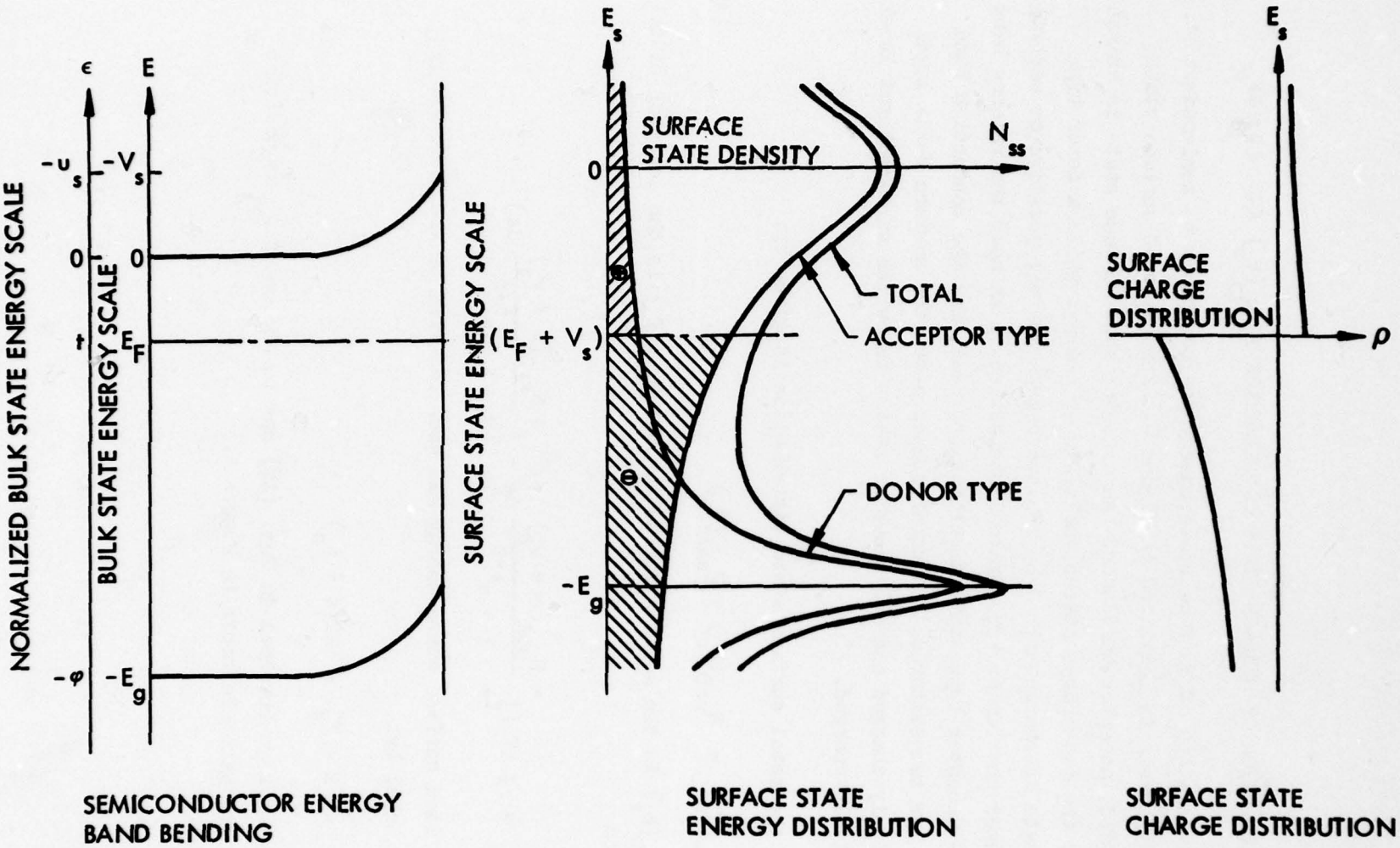

Figure C. Surface state energy distribution and charge state relation to bulk semiconductor energy levels

When the surface state density variation is negligible over an energy interval $\Delta E \approx kT$ or $\Delta\epsilon \approx 1$, a considerable simplification of Eqn. (A8) is possible by using the completely degenerate approximation:

$$Q_{\square} = q\,kT\,[\int_{-\infty}^{t} N_{ssA}(\epsilon + v_s)\,d\epsilon - \int_{t}^{\infty} N_{ssD}(\epsilon + v_s)\,d\epsilon] \qquad (A9)$$

which also allows a simple expression for surface state contribution to capacity:

$$\frac{dQ_{\square}}{dV_s} = q\,[N_{ssA}(E_F + V_s) + N_{ssD}(E_F + V_s)] \quad . \qquad (A10)$$

Equations (A9) and (A10) were used for surface state analysis programs rather than carry out the numerical integration required in Eqn. (A8).

In the course of this work, a number of trial analytic functions were investigated to describe the experimental surface state density distribution. These included discrete states or a δ-function distribution:

$$N_{ssA} = N_{sA}\,\delta(E_s - E_A)$$

$$N_{ssD} = N_{sD}\,\delta(E_s - E_D) \quad ,$$

a uniform distribution:

$$N_{ssA} = \begin{cases} S_A & \text{for } 0 \geq E_s \geq -E_g \\ 0 & \text{otherwise} \end{cases}$$

$$N_{ssD} = \begin{cases} S_D & \text{for } 0 \geq E_s \geq -E_g \\ 0 & \text{otherwise} \end{cases}$$

a distribution linearly varying from a band edge:

$$N_{ssA} = \begin{cases} S_A(1 + \dfrac{E_s}{E_A}) & \text{for } 0 \geq E_s \geq -E_A \\ 0 & \text{otherwise} \end{cases} \quad ,$$

$$N_{ssD} = \begin{cases} S_D\left(1 - \dfrac{E_s + E_g}{E_D}\right) & \text{for } -E_D \geq E_s \geq -E_g \\ 0 & \text{otherwise,} \end{cases}$$

A Gaussian distribution:

$$N_{ssA} = S_A \exp -\left(\frac{E_s - E_A}{\Delta_A}\right)^2$$

$$N_{ssD} = S_D \exp -\left(\frac{E_s - E_D}{\Delta_D}\right)^2$$

A Lorentzian distribution:

$$N_{ssA} = \frac{S_A}{\left(\dfrac{E_s - E_A}{\Delta_A}\right)^2 + 1}$$

$$N_{ssD} = \frac{S_D}{\left(\dfrac{E_s - E_D}{\Delta_D}\right)^2 + 1}$$

and a root Lorentzian distribution:

$$N_{ssA} = \frac{S_A}{\sqrt{\left(\dfrac{E_S - E_A}{\Delta_A}\right)^2 + 1}}$$

$$N_{ssD} = \frac{S_D}{\sqrt{\left(\dfrac{E_S - E_D}{\Delta_D}\right)^2 + 1}}$$

The root Lorentzian distribution gave a best fit to all of our experimental data and the linearly varying distribution was second best. The Gaussian,

Lorentzian, and δ function distributions were consistently too sharply peaked while the uniform distribution was consistently too broad. Note that for each surface state type, the root Lorentzian distribution has three adjustable parameters: peak surface state density, energy position of the peak and width of the distribution. Adjustment of the resultant six parameters results in an excellent fit of deduced surface state distributions to experimental data via the C-V characteristic.

III. CALCULATION PROCEDURE

All calculations were performed on an HP 9810A calculator with an HP 9862 plotter accessory. Time consuming numerical integrations were minimized by utilizing the approximations to integrals I_4 through I_7 as the surface potential was stepped through the depletion regime. The main program flow chart is shown in Figure D.

Coordinate entries required were V_{max} and V_{min} for the gate voltage and $(C/C_o)_{max} = 1$ and $(C/C_o)_{min}$ which were chosen as appropriate to each device modeled. The semiconductor bulk and device parameter entries required were:

- E_g - energy gap in eV at device operating temperature.
- T - device operating temperature in $^\circ K$.
- n_B - majority (electron) carrier concentration in cm^{-3}.
- ϵ_s - static dielectric constant of HgCdTe (assumed to be 18 in the alloy compositions studied here).
- ϵ_i - static dielectric constant of insulator (ZnS).
- t_i - thickness of insulator in cm.
- m_h^* - heavy hole effective mass ($m_h^* \approx .55$).
- P - interband matrix element. $P = 8.4 \times 10^{-8}$ eV·cm across the HgCdTe alloy system.

Since the ZnS film dielectric constant is not well established, is known to be temperature dependent, and the ZnS film thickness was not accurately known, device capacity was measured in strong inversion and then a consistent set of values for ϵ_i and t_i were chosen.

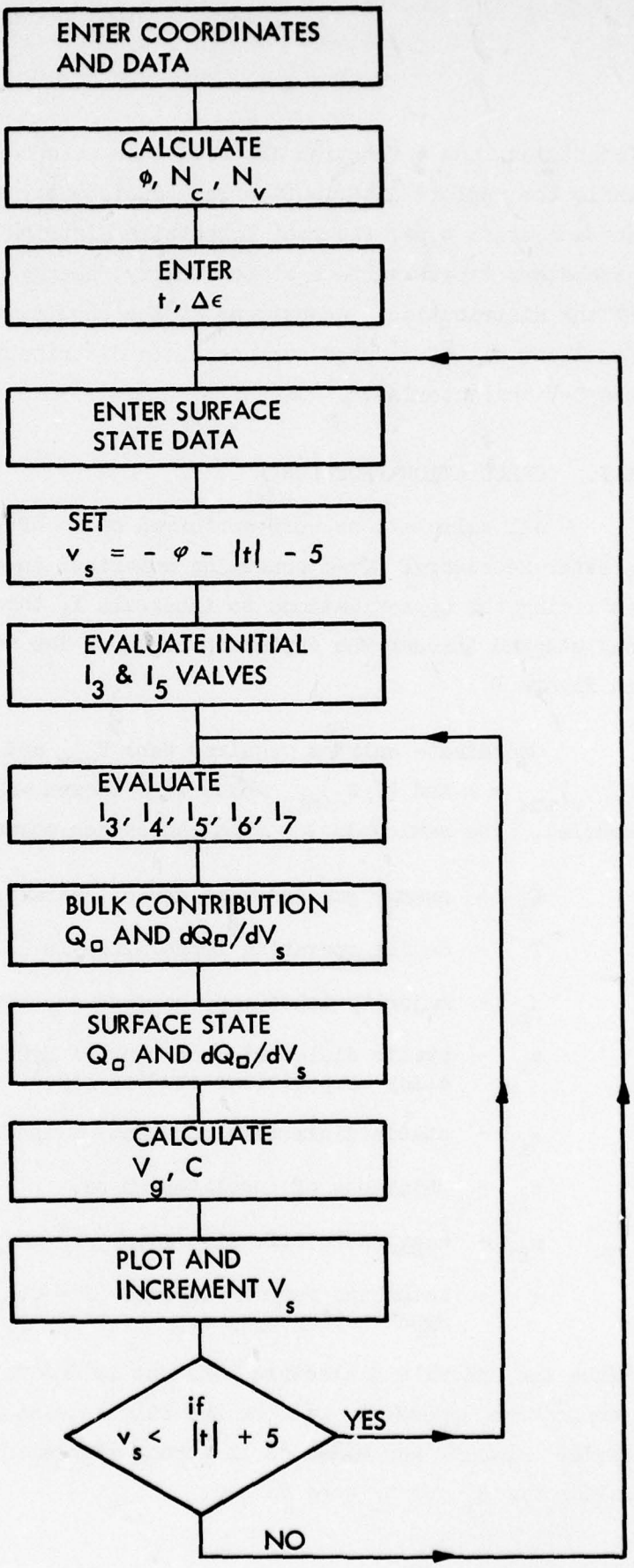

Fig. D. Flow chart for program to calculate C vs. V with prescribed surface state distribution

After the above data was entered in the program, $\varphi = E_g/kT$, $N_c(E_g,P,T)$ and $N_v(m_h^*,T)$ were calculated and the quantities φ and n_B/N_c displayed. From Figure B, the appropriate value of $t = (E_F-E_c)/kT$ was determined and entered in the calculation, along with $\Delta\epsilon$. The latter entry determined the step size used in the numerical evaluation of integrals I_3 through I_7.

Next, the surface state data was entered. The set of data to be entered depended on the analytic approximation assumed for the surface state distribution. However, in every case the experimental measurement gave significant guidance to the initial parameter choice since the surface state contribution dominated the device capacitance as the surface potential varied through the depletion regime. In particular the minimum capacity was determined by the minimum surface state density and the width (in gate voltage) of the C-V curve was determined by the total number of surface states between conduction and valence band edges.

Since both V_g and C can be calculated from the surface potential (see Eqns. (1) and (2)), the calculation strategy was to start with a value of v_s in strong inversion (initial $v_s = -\varphi - |t| - 5$ from Figure D) and increment v_s until strong accumulation was reached ($v_s = |t| + 5$). By starting in strong inversion, fixed values of I_3, I_5 and I_7 could be used until v_s increased to near accumulation. The subroutine for appropriate evaluation or approximation of the I's is shown in Figure E. When numerical integration was required, a simple Simpson's rule procedure was used. It was found, by considerable program testing, that a step size of $\Delta\epsilon = 0.1$ or .05 gave satisfactory accuracy. Since all integrands approach zero exponentially for large values of ϵ (including I_5), proper termination of the Simpson's rule summation was ignored. Satisfactory upper limits for the various numerical integrations were:

$$\infty \approx \epsilon_{U.L.} = 10 + |t| \qquad \text{for } I_3 \text{ and } I_5 \ (v_s < -t - 5)$$

$$\infty \approx \epsilon_{U.L.} = 10 + t + v_s \qquad \text{for } I_5 \text{ and } I_7 \ (v_s > -t - 5)$$

$$\infty \approx \epsilon_{U.L.} = 10 - t - \varphi - v_s \qquad \text{for } I_4 \text{ and } I_6 \ (v_s < -\varphi - t + 5)$$

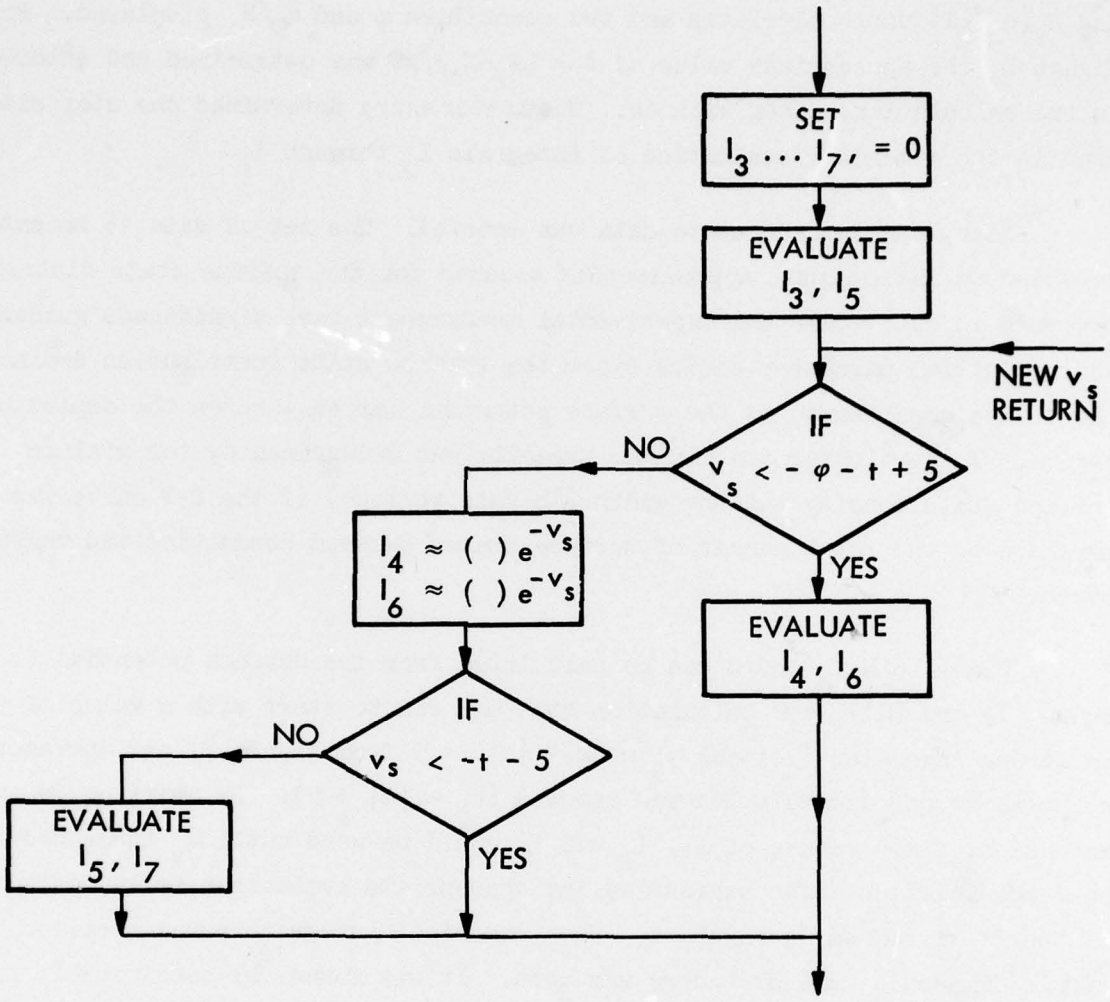

Figure E. Subroutine for evaluation or approximation of integrals

After calculating the bulk contribution to $Q_{\square}$ and $dQ_{\square}/dV_s$, the corresponding surface state contributions were calculated from Eqns (A9) and (A10). For all analytic approximations used for $N_{ssA}(E_s)$ and $N_{ssD}(E_s)$, analytic evaluation of the integrals in Eqn. (A9) was possible. (In the root Lorentzian case, integration was terminated at the band edges rather than $\pm\infty$ to avoid a logarithmic divergence.)

After a few trial and error calculations, a surface state distribution can usually be found which gives a reasonable approximation to an experimental C-V curve. This, in turn, gives a good approximation to the surface potential as a function of gate voltage through Eqn. (1) since $Q_{\square}(V_s)$ is a relatively insensitive function of V_s:

$$Q_{\square}(\text{surface}) \propto \int N_{ss}(\epsilon + v_s)\, d\epsilon$$

from Eqn. (A8). From C vs V_s, an accurate calculation of $N_{ss}(V_s)$ is possible by subtracting the bulk contribution from $dQ_{\square}/dV_s$:

$$qN_{ss}(E_F + V_s) = \frac{C(V_s)}{1 - \dfrac{C(V_s)}{C_o}} - \frac{dQ_{\square}(\text{bulk})}{dV_s} \quad . \tag{A11}$$

The empirical $N_{ss}(E_s)$ obtained from Eqn. (A11) may then be used for a refined calculation of V_s vs. V_g and the entire process repeated until satisfactory convergence of calculated vs. experimental C-V curves is obtained.

DISTRIBUTION LIST

DEPARTMENT OF DEFENSE

Defense Communication Engineer Center
1860 Wiehle Ave
Reston, VA 22090
Attn: Code R320 C W Bergman
Attn: Code R410 J W McClean

Director
Defense Communications Agency
Washington, DC 20305
Attn: Code 540.5
Attn: Code 930 M I Burgett Jr

Defense Documentation Center
Cameron Station
Alexandria, VA 22314
Attn: TC

Director
Defense Intelligence Agency
Washington, DC 20301
Attn: DS-4A2

Director
Defense Nuclear Agency
Washington, DC 20305
Attn: TITL Tech Library
Attn: DDST
Attn: RAEV
Attn: STVL

Dir of Defense Rsch & Engineering
Department of Defense
Washington, DC 20301
Attn: S&SS (OS)

Commander
Field Command
Defense Nuclear Agency
Kirtland AFB, NM 87115
Attn: FCPR

Director
Interservice Nuclear Weapons School
Kirtland AFB, NM 87115
Attn: Document Control

Director
Joint Strat Tgt Planning Staff JCS
Offutt AFB Omaha, NB 68113
Attn: JLTW-2

Chief
Livermore Division Fld Command DNA
Lawrence Livermore Laboratory
P.O. Box 808
Livermore, CA 94550
Attn: FCPRL

Director
National Security Agency
Ft. George G. Meade, MD 20755
Attn: O O Van Gunten R-425
Attn: TDL

DEPARTMENT OF ARMY

Project Manager
Army Tactical Data Systems
US Army Electronics Command
Fort Monmouth, NJ 07703
Attn: DRCPN-TDS-SD
Attn: DWAINE B Huewe

Commander
BMD System Command
P.O. Box 1500
Huntsville, AL 35807
Attn: BDMSC-TEN

Commander
Frankford Arsenal
Bridge and Tacony Sts
Philadelphia, PA 19137
Attn: SARFA FCD

Commander
Harry Diamond Laboratories
2800 Powder Mill Road
Adelphi, MD 20783
Attn: DRXDO-EM
Attn: DRXDO-NP
Attn: DRXDO-TI/Tech Library
Attn: DRXDO-RB
Attn: DRXDO-RCC
Attn: DRXDO-RC
Attn: J Halpin
Attn: J McGarrity

Commanding Officer
Night Vision Laboratory
US Army Electronics Command
Fort Belvoir, VA 22060
Attn: Capt, Allan S Parker

Commander
Picatinny Arsenal
Dover, NJ 07801
Attn: SMUPA-FR-S-P
Attn: SARPA-FR-E
Attn: SMUPA-ND-W
Attn: SMUPA-ND-D-B
Attn: SARPA-ND-C-E
Attn: SARPA-ND-N
Attn: SMUPA-ND-N-E

Commander
Redstone Scientific Information Center
US Army Missile Command
Redstone Arsenal, AL 35809
Attn: Chief, Documents

Secretary of the Army
Washington, DC 20310
Attn: ODUSA or D Willard

Director
Trasana
White Sands Missile Range NM 88002
Attn: ATAA-EAC

Director
US Army Ballistic Research Labs
Aberdeen Proving Ground, MD 21005
Attn: DRXBR-X
Attn: DRXBR-VL
Attn: DRXBR-AM
Attn: DRXRD-BVL

Chief
US Army Communications Systems Agency
Fort Monmouth, NJ 07703
Attn: SCCM-AD-SV/Library

Commander
US Army Electronics Command
Fort Monmouth, NJ 07703
Attn: DRSEL-TL-IR
Attn: DRSEL-CE
Attn: DRSEL-CT-HDK
Attn: DRSEL-GG-TD
Attn: DRSEL-TL-MD
Attn: DRSEL-TL-ND
Attn: DRSEL-PL-ENV

Commandant
US Army Engineer School
Ft Belvoir VA 22060
Attn: ATSE-CTD-CS

Commander-in-Chief
US Army Europe & Seventh Army
APO New York 09403
(Heidelberg)
Attn: ODCSE-E AEAGE-PI

Commandant
US Army Field Artillery School
Fort Sill, OK 73503
Attn: ATSFA-CTD-ME

Commander
US Army Material Dev & Readiness CMD
5001 Esenhower Ave
Alexandria, VA 22333
Attn: DRCDE-D

Commander, US Army Missile Command
Redstone Arsenal, AL 35809
Attn: DRSI-RGP
Attn: DRCPM-PE-EA
Attn: DRSMI-RGD
Attn: DRSMI-RGP
Attn: DRSMI-RRR

Chief
US Army Nuc & Chemical Surety GP
Bldg 2073, North Area
Ft Belvoir, VA 22060
Attn: MOSG-ND

Commander
US Army Nuclear Agency
7500 Backlick Road
Building 2073
Springfield, VA 22150
Attn: ATCN-W

Commander
US Army Tank Automotive Command
Warren, MI 48090
Attn: DRCPM-GCM-SW

Commander
White Sands Missile Range
White Sands Missile Range NM 88002
Attn: STEWS-TE-NT

DEPARTMENT OF NAVY

Chief of Naval Research
Navy Department
Arlington, VA 22217
Attn: Code 427

Commander Officer
Naval Avionics Facility
21st & Arlington Ave
Indianapolis, IN 46218
Attn: Branch 942

Commander
Naval Electronic Systems Command Hqs
Washington, DC 20360
Attn: Code 504511
Attn: Code 50451
Attn: PME 117-21
Attn: Code 5032
Attn: Flex 05323

Commanding Officer
Naval Intelligence Support Ctr
4301 Suitland Road, Bldg. 5
Washington, DC 20390
Attn: NISC-45

Director
Naval Research Laboratory
Washington, DC 20375
Attn: Code 4004
Attn: Code 6631
Attn: Code 5210
Attn: Code 5216
Attn: Code 6460
Attn: Code 601
Attn: Code 7701
Attn: Code 2627

Commander
Naval Sea Systems Command
Navy Department
Washington, DC 20362
Attn: SEA-9931

Officer-in-Charge
Naval Surface Weapons Center
White Oak, Silver Spring, MD 20910
Attn: Code WA52
Attn: Code WA501/Navy Nuc Prgms Off
Attn: Code WA50

Commander
Naval Weapons Center
China Lake, CA 9355
Attn: Code 533 Tech Library

Commanding Officer
Naval Weapons Evaluation Facility
Kirtland AFB Albuquerque, NM 87117
Attn: Code ATG/Mr Stanley

Commanding Officer
Naval Weapons Support Center
Crane, IN 47522
Attn: Code 7024/J Ramsey
Attn: Code 70242/J A Munarin

Commanding Officer
Nuclear Weapons TNG Center Pacific
Naval Air Station, North Island
San Diego, CA 92135
Attn: Code 50

Director
Strategic Systems Project Office
Navy Department
Washington, DC 20376
Attn: SP 2701
Attn: NSP-2342
Attn: NSP-27331

DEPARTMENT OF THE AIR FORCE

RADC/Deputy for Electronic Technology
Hanscom AFB, MA 01731
Attn: ET/Stop 30/E Cormier
Attn: ES/Stop 30/F Shepherd
Attn: ES/Stop 30/E A Burke

AF Institute of Technology, AU
Wright-Patterson AFB, OH 45433
Attn: ENP/C J Bridgman

AF Materials Laboratory, AFSC
Wright-Patterson AFB, OH 45433
Attn: LTE

AF Weapons Laboratory, AFSC
Kirtland AFB, NM 87117
Attn: DES
Attn: ELA
Attn: ELP TREE SECTION
Attn: NT/Carl E Baum
Attn: ELS
Attn: NTS

AFTAC
Patrick AFB FL 32925
Attn: TFS/Maj M F Schneider

AF Avionics Laboratory, AFSC
Wright-Patterson AFB, OH 45433
Attn: DHE/H J Hennecke
Attn: DHM/C Friend
Attn: DH/Ltc McKenzie
Attn: AAT/M Friar

Commander
ASD
Wright-Patterson AFB, OH 45433
Attn: ASD/ENESS/P T Marth
Attn: ASD-YH-EX/Ltc R Leverette
Attn: ENACC/R L Fish

Hq ESD
Hanscom AFB, MA 01731
Attn: YSEV

Hq ESD
Hanscom AFB, MA 01731
Attn: YWET

Commander
Foreign Technology Division, AFSC
Wright-Patterson AFB, OH 45433
Attn: FTDP

Commander
Rome Air Development Center, AFSC
Griffiss AFB, NY 13440
Attn: RBRP
Attn: RBRAC

Commander
RADC/Deputy for Electronic Technology
Hanscom AFB, MA 01731
Attn: ES/A Kahan
Attn: ES/B Buchanan
Attn: ES/R Dolan

SAMSO/YE
Post Office Box 92960
Worldway Postal Center
Los Angeles, CA 90009
Attn: YEE

SAMSO/IN
Post Office Box 92960
Worldway Postal Center
Los Angeles, CA 90009
Attn: IND/I J Judy

SAMSO/MN
Norton AFB, CA 92409
Attn: MNNH

SAMSO/RS
Post Office Box 92960
Worldway Postal Center
Los Angeles, CA 90009
Attn: RSMG
Attn: RSSE

SAMSO/SK
Post Office Box 92960
Worldway Postal Center
Los Angeles, CA 90009
Attn: SKF

SAMSO/SZ
Post Office Box 92960
Worldway Postal Center
Los Angeles, CA 90009
Attn: SZJ

Commander in Chief
Strategic Air Command
Offutt AFB, NB 68113
Attn: XPFS
Attn: NRI-STINFO Library

US ENERGY RSCH & DEV ADMIN

University of California
Lawrence Livermore Laboratory
P. O. Box 808
Livermore, CA 94550
Attn: Hans Kruger L-96
Attn: Frederick R Kovar L-31
Attn: Donald J Meeker L-545
Attn: Tech Info Dept L-3
Attn: F K Miller L-156
Attn: William J Hogan L-531
Attn: Ronald L Ott L-531
Attn: Joseph E Keller Jr L-125
Attn: Lawrence Cleland L-156

Los Alamos Scientific Laboratory
P. O. Box 1663
Los Alamos NM 87545
Attn: Doc Con for B W Noel
Attn: Doc Con for J A Freed

SANDIA Laboratories
P. O. Box 5800
Albuquerque NM 87115
Attn: Doc Con for Org 2110/J A Hood
Attn: Doc Con for 3141 Sandia Rpt Coll
Attn: Doc Con for Org 2140/R Gregory

US Energy Research & Dev Admin
Albuquerque Operations Office
P. O. Box 5400
Albuquerque, NM 87115
Attn: Doc Con for WSSB

OTHER GOVERNMENT

Department of Commerce
National Bureau of Standards
Washington, DC 20234
Attn: Judson C French

DEPARTMENT OF DEFENSE
CONTRACTORS

Aerojet Electro-Systems Co.
Div of Aerojet-General Corp.
P. O. Box 296, 1100 W. Hollyvale Dr
Azusa, CA 91702
Attn: T D Hanscome

Aerospace Corp.
P. O. Box 92957
Los Angeles, CA 90009
Attn: John Ditre
Attn: Irving M Garfunkel
Attn: S P Bower
Attn: Julian Reinheimer
Attn: L W Aukerman
Attn: Library
Attn: William W Willis

Analog Technology Corp.
3410 East Foothill Boulevard
Pasadena, CA 91107
Attn: J J Baum

AVCO Research & Systems Group
201 Lowell St
Wilmington, MA 01887
Attn: Research Lib/A830 Rm 7201

BDM Corp.
7915 Jones Branch Drive
McClean, VA 22101
Attn: T H Neighbors

BDM Corporation
P. O. Box 9274
Albuquerque International
Albuquerque, NM 87119
Attn: D R Alexander

Bendix Corp.
Communication Division
Fast Joppa Road
Baltimore, MD 21204
Attn: Document Control

Bendix Corp.
Research Laboratories Division
Bendix Center
Southfield, MI 48075
Attn: Mgr Prgm Dev/D J Niehaus
Attn: Max Frank

Boeing Company
P. O. Box 3707
Seattle, WA 98124
Attn: H W Wicklein/MS 17-11
Attn: Itsu Amura/2R-00
Attn: Aerospace Library
Attn: R S Caldwell/2R-00
Attn: Carl Rosenberg/2R-00

Booz-Allen and Hamilton, Inc.
106 Apple Street
Tinton Falls, NJ 07724
Attn: Raymond J Chrisner

California Institute of Technology
Jet Propulsion Laboratory
4800 Oak Grove Drive
Pasadena, CA 91103
Attn: J Bryden
Attn: A G Stanley

Charles Stark Draper Laboratory Inc.
555 Technology Square
Cambridge, MA 02139
Attn: Kenneth Fertig
Attn: Paul R Kelly

Cincinnati Electronics Corp.
2630 Glendale - Milford Road
Cincinnati, OH 45241
Attn: Lois Hammond
Attn: C R Stump

Control Data Corporation
P. O. Box O
Minneapolis, MN 55440
Attn: Jack Meehan

Cutler-Hammer, Inc.
AIL Division
Comac Road
Deer Park, NY 11729
Attn: Central Tech Files/A Anthony

Dikewood Industries, Inc.
1009 Bradbury Drive, S. E.
Albuquerque, NM 87106
Attn: L Wayne Davis

E-Systems, Inc.
Greenville Division
P. O. Box 1056
Greenville, TX 75401
Attn: Library 8-50100

Effects Technology, Inc.
5383 Hollister Avenue
Santa Barbara, CA 93111
Attn: Edward J Steele

Exp & Math Physics Consultants
P. O. Box 66331
Los Angeles, CA 90066
Attn: Thomas M Jordan

Fairchild Camera & Instrument Corp.
464 Ellis St
Mountain View, CA 94040
Attn: Sec Dept for 2-233 D K Myers

Fairchild Industries, Inc.
Sherman Fairchild Technology Center
20301 Century Boulevard
Germantown, MD 20767
Attn: Mgr Config Data & Standards

Florida, University of
P. O. Box 284
Gainesville, FL 32601
Attn: Patricia B Rambo
Attn: D P Kennedy

Ford Aerospace & Communications Corp.
3939 Fabian Way
Palo Alto, CA 94303
Attn: Edward R Hahn/MS-X22
Attn: Donald R McMorrow/MS-G30
Attn: Samuel R Crawford/MS-531

Ford Aerospace & Comm Operations
Ford & Jamboree Roads
Newport Beach, CA 92663
Attn: F R Poncelet Jr.
Attn: Ken C Attinger
Attn: Tech Info Section

Franklin Institute, The
20th St and Parkway
Philadelphia, PA 19103
Attn: Ramie H Thompson

Garrett Corporation
P. O. Box 92248, 9851 Sepulveda Blvd
Los Angeles, CA 90009
Attn: Robert E Weir/Dept 93-9

General Dynamics Corp.
Electronics Div Orlando Operations
P. O. Box 2566
Orlando, FL 32802
Attn: D W Coleman

General Electric Company
Space Division
Valley Forge Space Center
Goddard Blvd King of Prussia
P. O. Box 8555
Philadelphia, PA 19101
Attn: Larry I Chasen
Attn: John L Andrews
Attn: Joseph C Peden/VFSC, Rm 4230M

General Electric Company
Re-Entry & Environmental Systems Div
P. O. Box 7722
3198 Chestnut St
Philadelphia, PA 19101
Attn: Robert V Benedict
Attn: John W Palchefsky Jr
Attn: Ray E Anderson

General Electric Company
Ordnance Systems
100 Plastics Ave.
Pittsfield, MA 01201

General Electric Company
Tempo-Center for Advanced Studies
816 State St (P O Drawer QQ)
Santa Barbara, CA 93102
Attn: Royden R Rutherford
Attn: DASIAC
Attn: M Espig
Attn: William McNamera

General Electric Company
Aircraft Engine Business Group
Evendale Plant Int Hwy 75 S
Cincinnati, OH 45215
Attn: John A Ellerhorst E2

General Electric Company
Aerospace Electronics Systems
French Road
Utica, NY 13503
Attn: Charles M Hewison/Drop 624
Attn: W J Patterson/Drop 233

General Electric Company
P. O. Box 5000
Binghamton, NY 13902
Attn: David W Pepin/Drop 160

General Electric Company-Tempo
c/o Defense Nuclear Agency
Washington, DC 20305
Attn: DASIAC
Attn: William Alfonte

General Research Corporation
P. O. Box 3587
Santa Barbara, CA 93105
Attn: Robert D Hill

Georgia Institute of Technology
Georgia Tech Research Institute
Atlanta, GA 30332
Attn: R Curry

Grumman Aerospace Corporation
South Oyster Bay Road
Bethpage, NY 11714
Attn: Jerry Rogers/Dept 533

GTE Sylvania, Inc.
Electronics Systems GRP-Eastern Div
77 A St
Needham, MA 02194
Attn: Charles A Thornhill, Librarian
Attn: James A Waldon
Attn: Leonard L Blaisdell

GTE Sylvania, Inc.
189 B St
Needham Heights, MA 02194
Attn: Paul B Fredrickson
Attn: Herbert A Ullman
Attn: H & V Group
Attn: Charles H Ramsbottom

Gulton Industries, Inc.
Engineered Magnetics Division
13041 Cerise Ave
Hawthorne, CA 90250
Attn: Engnmagnetics Div

Harris Corp.
Harris Semiconductor Division
P. O. Box 883
Melbourne, FL 32901
Attn: Wayne E Abare/MS 16-111
Attn: Carl F Davis/MS 17-220
Attn: T L Clark/MS 4040

Hazeltine Corp.
Pulaski Rd
Greenlawn, NY 11740
Attn: Tech Info Ctr/M Waite

Honeywell Inc.
Avionics Division
2600 Ridgeway Parkway
Minneapolis, MN 55413
Attn: Ronald R Johnson/A1622
Attn: R J Kell/MS S2572

Honeywell Inc.
Avionics Division
13350 US Highway 19 North
St Petersburg, FL 33733
Attn: H H Noble/MS 725-5A
Attn: S H Graaff/MS 725-J

Honeywell Inc.
Radiation Center
2 Forbes Road
Lexington, MA 02173
Attn: Technical Library

Hughes Aircraft Company
Centinela and Teale
Culver City, CA 90230
Attn: Dan Binder/MS 6-D147
Attn: Billy W Campbell/MS 6-E-110
Attn: Kenneth R Walker/MS D157
Attn: John B Singletary/MS 6-D133

Hughes Aircraft Co., El Segundo Site
P. O. Box 92919
Los Angeles, CA 90009
Attn: William W Scott/MS A1080
Attn: Edward C Smith/MS A620

IBM Corporation
Route 17C
Owego, NY 13827
Attn: Frank Frankovsky
Attn: Harry W Mathers/Dept M41

Intl Tel & Telegraph Corp
500 Washington Ave
Nutley, NY 07110
Attn: Alexander T Richardson

Ion Physics Corp.
South Bedford St
Burlington, MA 01803
Attn: Robert D Evans

IRT Corp.
P. O. Box 81087
San Diego, CA 92138
Attn: MDC
Attn: Leo D Cotter
Attn: R L Mertz

JAYCOR
205 S. Whitting St, Suite 500
Alexandria, VA 22304
Attn: Catherine Turesko
Attn: Robert Sullivan

Johns Hopkins University
Applied Physics Laboratory
Johns Hopkins Road
Laurel, MD 20810
Attn: Peter E Partridge

Kaman Sciences Corp.
P. O. Box 7463
Colorado Springs, CO 80933
Attn: Jerry I Lubell
Attn: Walter E Ware
Attn: John R Hoffman
Attn: Donald H Bryce
Attn: Albert P Bridges
Attn: W Foster Rich

Litton Systems, Inc.
Guidance & Control Systems Division
5500 Canoga Ave
Woodland Hills, CA 91364
Attn: John P Retzler
Attn: Val J Ashby/MS 67
Attn: R W Maughmer

Litton Systems, Inc.
Electron Tube Division
1035 Westminster Drive
Williamsport, PA 17701
Attn: Frank J McCarthy

Lockheed Missiles & Space Co. Inc.
P. O. Box 504
Sunnyvale, CA 94088
Attn: B T Kimura/Dept 81-14
Attn: E A Smith/Dept 85-85
Attn: George F Heath/Dept 81-14
Attn: Samuel I Taimuty/Dept 85-85
Attn: L Rossi/Dept 81-64

Lockheed Missiles & Space Co. Inc.
3251 Hanover St
Palo Alto, CA 94304
Attn: Tech Info Ctr D/Coll

M.I.T. Lincoln Laboratory
P. O. Box 73
Lexington, MA 02173
Attn: Leona Loughlin, Librarian A-082

Martin Marietta Aerospace
Orlando Division
P. O. Box 5837
Orlando, FL 32805
Attn: Jack M Ashford/MP-537
Attn: William W Mras/MP-413
Attn: Mona C Griffith/Lib MP-30

Martin Marietta Corp.
Denver Division
P. O. Box 179
Denver, CO 80201
Attn: Paul G Kase/Mail 8203
Attn: Research Lib 6617 J R McKee
Attn: J E Goodwin/Mail 0452
Attn: B T Graham/MS PO-454

McDonnel Douglas Corp.
P. O. Box 516
St Louis, MO 63166
Attn: Tom Ender
Attn: Technical Library

McDonnel Douglas Corp.
5301 Bolsa Ave
Huntington Beach, CA 92647
Attn: Stanley Schneider

McDonnel Douglas Corp.
3855 Lakewood Boulevard
Long Beach, CA 90846
Attn: Technical Library, C1-290/36-84

Mission Research Corp.
735 State St
Santa Barbara, CA 93101
Attn: William C Hart

Mission Research Corp.-San Diego
P. O. Box 1209
La Jolla, CA 92038
Attn: V A J Van Lint
Attn: J P Raymond

The MITRE Corp.
P. O. Box 208
Bedford, MA 01730
Attn: M E Fitzgerald
Attn: Library

National Academy of Sciences
2101 Constitution Ave, NW
Washington, DC 20418
Attn: National Materials Advisory Board
Attn: R S Shane, Nat Materials Advsy

University of New Mexico
Electrical Engineering & Computer
Science Dept
Albuquerque, NM 87131
Attn: Harold Southward

Northrop Corp.
Electronic Division
1 Research Park
Palos Verdes Peninsula, CA 90274
Attn: George H Towner
Attn: Boyce T Ahlport

Northrop Corp.
Northrop Research & Technology Ctr
3401 West Broadway
Hawthorne, CA 90250
Attn: Orlie L Curtis, Jr
Attn: David N Pocock
Attn: J R Srour

Northrop Corp.
Electronic Division
2301 West 120th St
Hawthorne, CA 90250
Attn: Vincent R DeMartino
Attn: Joseph D Russo
Attn: John M Reynolds

Palisades Inst for Rsch Services Inc.
201 Varick St
New York, NY 10014
Attn: Records Supervisor

Physics International Co.
2700 Merced St
San Leandro, CA 94577
Attn: Doc Con for C H Stallings
Attn: Doc Con for J H Huntington

R&D Associates
P. O. Box 9695
Marina Del Rey, CA 90291
Attn: S Clay Rogers

Raytheon Company
Hartwell Road
Bedford, MA 01730
Attn: Gajanan H Joshi, Radar Sys Lab

Raytheon Company
528 Boston Post Road
Sudbury, MA 01776
Attn: Harold L Flescher

RCA Corp.
Government Systems Division
Astro Electronics
P. O. Box 800, Locust Corner
East Windsor Township
Princeton, NJ 08540
Attn: George J Brucker

RCA Corporation
Camden Complex
Front & Cooper Sts
Camden, NJ 08012
Attn: E Van Keuren 13-5-2

Rensselaer Polytechnic Institute
P. O. Box 965
Troy, NY 12181
Attn: Ronald J Gutmann

Research Triangle Institute
P. O. Box 12194
Research Triangle Park, NC 27709
Attn: Eng Div Mayrant Simons Jr

Rockwell International Corp.
P. O. Box 3105
Anaheim, CA 92803
Attn: George C Messenger FB61
Attn: Donald J Stevens FA70
Attn: K F Hull
Attn: N J Rudie FA53
Attn: James E Bell, HA10

Rockwell International Corporation
3701 West Imperial Highway
Los Angeles, CA 90009
Attn: T B Yates

Rockwell International Corporation
Collins Divisions
400 Collins Road NE
Cedar Rapids, IA 52406
Attn: Dennis Sutherland
Attn: Alan A Langenfeld
Attn: Mildred A Blair

Sanders Associates, Inc.
95 Canal St
Nashua, NH 03060
Attn: Moe L Aitel NCA 1 3236

Science Applications, Inc.
P. O. Box 2351
La Jolla, CA 92038
Attn: J Robert Beyster

Science Applications, Inc.
Huntsville Division
2109 W Clinton Ave
Suite 700
Huntsville, AL 35805
Attn: Noel R Byrn

Singer Company (Data Systems)
150 Totowa Road
Wayne, NJ 07470
Attn: Tech Info Center

Sperry Flight Systems Division
Sperry Rand Corp.
P. O. Box 21111
Phoenix, AZ 85036
Attn: D Andrew Schow

Sperry Univac
Univac Park, P. O. Box 3535
St. Paul, MN 55165
Attn: James A Inda/MS 41T25

Stanford Research Institute
333 Ravenswood Ave
Menlo Park, CA 94025
Attn: Philip J Dolan
Attn: Arthur Lee Whitson

Stanford Research Institute
306 Wynn Drive, NW
Huntsville, AL 35805
Attn: MacPherson Morgan

Sundstrand Corp.
4751 Harrison Ave.
Rockford, IL 61101
Attn: Curtis B White

Systron-Donner Corp.
1090 San Miguel Road
Concord, CA 94518
Attn: Gordon B Dean
Attn: Harold D Morris

Texas Instruments, Inc.
P. O. Box 5474
Dallas, TX 75222
Attn: Donald J Manus/MS 72

Texas Tech University
P. O. Box 5404 North College Station
Lubbock, TX 79417
Attn: Travis L Simpson

TRW Defense & Space Sys Group
One Space Park
Redondo Beach, CA 90278
Attn: Robert M Webb R1 2410
Attn: Tech Info Center/S1930
Attn: O E Adams R1-2036
Attn: R K Plebuch R1-2078

TRW Defense & Space Sys Group
San Bernardino Operations
P. O. Box 1310
San Bernardino, CA 92402
Attn: R Kitter

United Technologies Corp.
Hamilton Standard Division
Bradley International Airport
Windsor Locks, CT 06069
Attn: Raymond G Giguere

Vought Corp.
P. O. Box 5907
Dallas, TX 75222
Attn: Technical Data Ctr

ADDITIONAL DISTRIBUTION LIST

Hanscom AFB, MA 01731
Attn: AFGL/SUSRP/Stop 30
Attn: AFGL/CC/Stop 30
Attn: AFGL/SUOL/Stop 20
Attn: ESD/XR/Stop 30
Attn: ESD/XR/Stop 30/D Brick
Attn: DCD/SATIN IV
Attn: MCAE/Lt Col D Sparks
Attn: ES/Stop 30
Attn: EE/Stop 30

Griffiss AFB, NY 13441
Attn: RADC/OC
Attn: RADC/IS
Attn: RADC/DC

Attn: RADC/IR
Attn: RADC/CA
Attn: RADC/TIR
Attn: RADC/DAP
Attn: RADC/TILD

Maxwell AFB, AL 36112
Attn: AUL/LSE-67-342

US Army Missile Command Labs
Redstone Scientific Information Ctr
Redstone Arsenal, AL 35809
Attn: Chief, Documents

SAMSO (YA/AT)
P. O. Box 92960
Worldway Postal Center
Los Angeles, CA 90009
Attn: Mr Hess

Naval Postgraduate School
Superintendent
Monterey, CA 93940
Attn: Library (Code 2124)

US Dept. of Commerce
Boulder Laboratories
Boulder, CO 80302
Attn: Library/NOAA/ERl

USAF Academy
Library
Colorado 80840
Attn: 80840

Eglin AFB, FL 32542
Attn: ADTC/DLOSL

Scott AFB, IL 62225
Attn: AWS/DNTI/Stop 400

NASA Scientific & Technical
Information Facility
P. O. Box 33
College Park, MD 20740

NASA Goddard Space Flight Center
Goddard Space Flight Center
Greenbelt, MD 20771
Attn: Technical Library, Code 252,
Bldg. 21

Naval Surface Weapons Center
White Oak Lab.
Silver Spring, MD 20910
Attn: Library Code 730, RM 1-321

US Naval Missile Center
Point Mugu, CA 93041
Attn: Tech. Library - Code NO322

NASA Johnson Space Center
Attn: JM6, Technical Library
Houston, TX 77058

NASA
Lewis Research Center
21000 Brookpark Road
Cleveland, OH 44135
Attn: Technical Library

Wright-Patterson AFB, OH 45433
Attn: AFAL/CA
Attn: AFIT/LD, Bldg. 640, Area B
Attn: ASD/ASFR
Attn: ASD/FTD/ETID

Defense Communications Engineering
Center
1860 Wiehls Ave
Reston, VA 22090
Attn: Code R103R

Director, Technical Information
DARPA
1400 Wilson Blvd.
Arlington, VA 22209

Department of the Navy
800 North Quincy St
Arlington, VA 22217
Attn: ONRL Documents, Code 102IP

SAMSO
P. O. Box 92960
Worldway Postal Center
Los Angeles, CA 90006
Attn: Lt Col Staubs

US Army Electronics Command
Fort Monmouth, NJ 07703
Attn: AMSEL-GG-TD

Kirtland AFB NM 87117
Attn: AFWL/SUL Technical Library

US Naval Weapons Center
China Lake, CA 93555
Attn: Technical Library

Los Alamos Scientific Lab.
P. O. Box 1663
Los Alamos, NM 87544
Attn: Report Library

Hq DNA
Washington DC 20305
Attn: Technical Library

Secretary of the Air Force
Washington DC 20330
Attn: SAFRD

Scott AFB IL 62225
Attn: ETAC/CB/Stop 825

Andrews AFB
Washington DC 20334
Attn: AFSC/DLC

Army Material Command
Washington, DC 20315
Attn: AMCRD

NASA Langley Research Center
Langley Station
Hampton, VA 23365
Attn: Technical Library/MS 185

NASA
Washington DC 20546
Attn: Library (KSA-10)

Andrews AFB
Washington, DC 20334
Attn: AFSC/DLS

AFOSR, Bldg 410
Bolling AFB, Washington DC 20332
Attn: CC

AFML
Wright Patterson AFB, OH 45433

The Pentagon
Room 3-D-139
Washington, DC 20301
Attn: ODDR&E-OSD (Library)

ONR (Library)
Washington, DC 20360

Defense Intelligence Agency
Washington, DC 20301
Attn: SO-3A

AFAL
Wright-Patterson AFB, OH 45433
Attn: WRA-1/Library
Attn: TSR-5/Technical Library

Advisory Group on Electron Devices
201 Varick St, 9th Floor
New York, NY 10014

White Sands Missile Range, NM 88002
Attn: STEWS-AD-L/Technical Library

University of New Mexico
Dept. of Electrical Engineering

Albuquerque, NM 87106
Attn: D Neaman

RADC/ESE, Stop 30, J. M. Cullen
Hanscom AFB, MA 01731

MISSION
of
Rome Air Development Center

RADC plans and conducts research, exploratory and advanced development programs in command, control, and communications (C^3) activities, and in the C^3 areas of information sciences and intelligence. The principal technical mission areas are communications, electromagnetic guidance and control, surveillance of ground and aerospace objects, intelligence data collection and handling, information system technology, ionospheric propagation, solid state sciences, microwave physics and electronic reliability, maintainability and compatibility.

Printed by
United States Air Force
Hanscom AFB, Mass. 01731